

Physical properties of carbon nanotube/graphene junctions

Zur Erlangung des akademischen Grades eines
DOKTORS DER NATURWISSENSCHAFTEN
durch die Fakultät für Physik
des Karlsruher Instituts für Technologie

genehmigte

DISSERTATION

von

Dipl.-Phys. Pablo T. Robert

aus Paris, Frankreich

Tag der mündlichen Prüfung: 21.12.2012
Referent: Prof. Dr. Hilbert von Löhneysen
Korreferent: Prof. Dr. Wulf Wulfhekel

Contents

1	Basic properties of graphene and carbon nanotubes	5
1.1	Basics properties of carbon nanotubes and graphene	5
1.1.1	Structural properties	5
1.1.2	Band structure	8
1.1.3	Electrical transport properties	11
1.2	Connecting graphene	13
1.2.1	Metal as leads	14
1.2.2	Multi-walled carbon nanotubes as leads	19
2	Structural properties	23
2.1	Introduction	23
2.2	Semi-empirical methods	23
2.2.1	NDDO method	24
2.2.2	PM6-D method	24
2.3	Equilibrium distance	25
2.3.1	Geometry description	25
2.3.2	Binding energy	26
2.3.3	London dispersion forces	27
2.3.4	Curvature effect	29
2.4	Conclusion	32
3	Analytical calculations	33
3.1	Laplace Equation	33
3.2	Conformal mapping technique	34
3.2.1	Conformal transformations	34
3.2.2	Laplace Equation solution	34
3.3	Potential and charge density	36
4	Numerical calculations	39
4.1	Development of the charge-dipole model	39
4.2	Presentation of the charge-dipole model	40
4.3	Code validation	44
4.4	Geometry	46
4.5	Charge profile and scaling of the model	47
4.6	Effects of the potential difference	49

CONTENTS

4.7	Charge distribution in the graphene sheet and in the CNT	49
4.8	Effects of the edges of the graphene flake	55
4.9	Conclusion	57
5	Results for the charge distribution	59
5.1	Scaling of the influence length $l_{5\%max}$ with the radius of the CNT	59
5.2	Effects of the CNT-Graphene distance	61
5.3	Conclusion	62
6	Sample preparation	65
6.1	Introduction	65
6.2	Graphene	66
6.2.1	Substrate preparation	66
6.2.2	Graphene deposition	66
6.2.3	Graphene characterisation	67
6.3	Multi-walled carbon nanotubes	71
6.3.1	Solution of carbon nanotubes	71
6.3.2	Characterisation	71
6.4	Nanomaniplulation of MWCNT	73
6.5	Electron beam lithography	77
6.6	Metal deposition	80
7	Work function measurements	83
7.1	Kelvin Probe Force Microscopy	84
7.2	Ambient air measurements	85
7.3	Conclusion	88
8	Electrical transport experiments	91
8.1	Measurement setup	91
8.2	Sample description	93
8.3	Description of the measurements	94
8.3.1	Connecting graphene with metal	94
8.3.2	Connecting graphene with MWCNTs	97
8.4	MWCNT/graphene junction properties	102
8.4.1	Charge injection localisation	102
8.4.2	Gate dependence of the injection	104
8.5	Conclusion	110
A	Hartree-Fock method	113
A.1	Schrödinger equation	113
A.2	Hartree-Fock method	114
A.3	Implementation of the Hartree-Fock method	116
	References	121

Contents

CONTENTS

Introduction

Although the electronic structure of graphene had been predicted as early as 1947 by P. Wallace, until 2004 graphene remained a mere mental construction. The isolation of the first graphene layer by A. Geim and K. Novoselov unleashed an investigation frenzy around this new amazing material. For the first time, a one-atomic-thick layer of carbon atom could be accessed, manipulated and characterised. The electrical properties of this new wonder material soon proved to be astonishing. The description of the electrical transport due to massless Dirac fermions brings in relativistic theories contrasting with conventional solid state physics approaches. Graphene displays uncommon and rather counterintuitive behaviours and features such as anomalous quantum effects or conduction "without charge carriers". Not only does graphene exhibit astonishing electrical properties that makes it promising for electronic applications but rates among the strongest materials known, raising the interest for potential mechanical use.

In the permanent quest for smaller transistors together with better performances, graphene with its exceptionally high carrier mobility even at room temperature and great down-sizing potential is a promising building-block candidate. Now if graphene has such extraordinary electronic features, why is the "silicon-electronic era" not already over? The exciting prospectives in electronics are damped by technical limitations. The integration of graphene in electronic devices requires to connect it with metal leads. This requirement constitutes one major hindrance, as the intrinsic properties of graphene are strongly affected by the quality of the contact interface. Therefore unravelling and controlling the transport process at the interface is crucial to ensure a sustainable integration of graphene in electronic devices.

Carbon nanotubes are materials closely related to graphene, as they can be viewed as a rolled-up graphene sheet. Their excellent electrical properties in term of carrier mobility or maximal current density combined with good heat conduction properties makes them suitable replacement for metals in the nano-contact engineering field. The idea of using carbon nanotubes as lead to connect graphene is then supported by the amazing properties of both graphitic structures. The use of carbon nanotubes to connect graphene could open the way to "all-carbon" electronics as well as to a sustainable nano-electronics.

Understanding the transport properties at the carbon nanotube/graphene interface is thus crucial to develop good-quality junctions and therefore allow further applications. The investigations related to this topic are at an early stage, no systematic study has been reported up to now. The work presented constitutes a the first step toward a better understanding of these promising nano-junctions.

CONTENTS

In the first part, Sec. 1 the basic properties of graphene and of carbon nanotubes are recalled. An overview of the current stand on metal/graphene interfaces is presented as well as the advances made towards carbon nanotubes/graphene junctions. Sec. 2 gives an insight in the structural properties of carbon nanotube/graphene junctions. Semi-empirical quantum chemistry calculations were performed to determine the equilibrium distance between the two graphitic structures and to determine the strength of the bonding. The results of the structural calculations are used in Sec. 3 and Sec. 4 to compute the charge distribution at the interface. This was done first by using a 2D electrostatic analytic model in Sec. 3 whereas Sec. 4 presents the results obtained for the charge distribution with a 3D numerical model, termed as "charge-dipole" model. The results obtained by the two models are compared and discussed in Sec. 5. The conclusions of the calculations are used later in the discussion of the experimental results.

The experimental part of this work starts by describing in Sec. 6 the carbon nanotube/graphene devices fabrication process. The most delicate part of this process relies on using the nano-manipulation potential of atomic force microscopy to fabricate actually the carbon nanotube/graphene junction. To prove that carbon nanotubes have little effect on the charge distribution in graphene, work function measurements have been performed using Kelvin probe microscopy. These results are presented and discussed in Sec. 7. Finally, the transport measurements are reported and analysed in Sec. 8. The experimental set-up is presented as well as the type of characterisation performed. The statistics obtained probing several carbon nanotube/graphene devices constitutes the core of Sec. 8 along with the discussion that follows.

1

Basic properties of graphene and carbon nanotubes

1.1 Basics properties of carbon nanotubes and graphene

1.1.1 Structural properties

Carbon nanotubes (CNTs) and graphene are graphitic materials that are made of carbon atoms arranged in a hexagonal honeycomb lattice. They are respectively 1D and 2D graphitic materials. The electronic ground state configuration for the carbon element is $1s^2 2s^2 2p^2$. They belongs to the sp^2 -carbon materials together with fullerenes and graphite. This class of material shows hybridisation between the $2s$ and the $p_x p_y$ orbitals, which leads to the following electronic structure: $1s^2 sp^2 sp^2 sp^2 2p_z$. The hybridized sp^2 three orbitals are spanning a single plane. Their electrons form strong covalent bonds (σ bond) and do not participate in the electronic transport. The remaining $2p_z$ orbital is perpendicular to the plane defined by the sp^2 orbitals. Its electron may form delocalised weak π bonds and is responsible for the electronic transport properties. The atomic structure of the graphitic materials follows as a consequence of the orbital orientation.

Graphene

While the band structure of graphene had already been addressed in 1947 by P.R. Wallace (1), the experimental observation had not been reported until 2004 when A. Geim and K. Novoselov deposited few-atom-thick layer of carbon atoms, among them mono layers, onto a SiO_2 substrate (2). In 2005, Zhang *et al.* carried out the first clear characterisation of mono layer graphene by measuring the anomalous quantum Hall effect, one of the footprint of graphene (3).

In graphene, each carbon atom binds to its three closest neighbours by a covalent sp^2 bond. The distance between two neighbouring atoms is $a = 1.42 \text{ \AA}$ and is termed as in-plane distance. The unit cell is made up of two atoms A and B and can be defined with the lattice vectors

$$\mathbf{a}_1 = \frac{a}{2}(3, \sqrt{3}) \quad \text{and} \quad \mathbf{a}_2 = \frac{a}{2}(3, -\sqrt{3}) \quad (1.1)$$

1. BASIC PROPERTIES OF GRAPHENE AND CARBON NANOTUBES

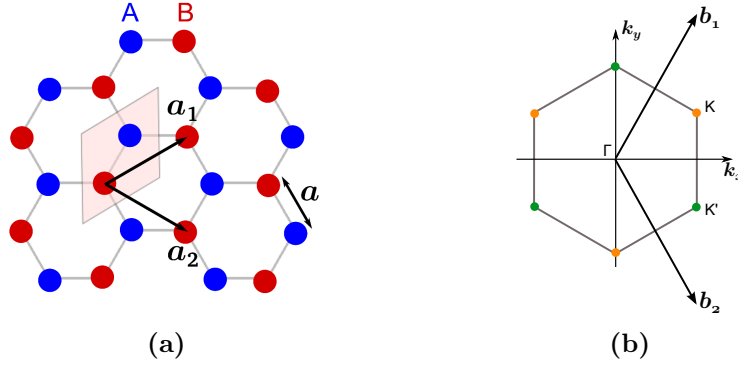


Figure 1.1: Fig. 1.1a: Graphene hexagonal lattice with the two sub-lattices formed by the atoms A and B. The lattice vectors \mathbf{a}_1 and \mathbf{a}_2 have been indicated. Fig. 1.1b: First Brillouin zone of graphene. The high symmetry points Γ , K and K' have been represented as well as the reciprocal lattice vectors \mathbf{b}_1 and \mathbf{b}_2 . Adapted from (4)

to generate the graphene hexagonal lattice (Fig. 1.1a). The distance between two carbon atoms belonging to the same lattice is then $|\mathbf{a}_1| = |\mathbf{a}_2| = 2.46 \text{ \AA}$. In reciprocal space, the lattice vectors are then given by

$$\mathbf{b}_1 = \frac{2\pi}{3a}(1, \sqrt{3}) \quad \text{and} \quad \mathbf{b}_2 = \frac{2\pi}{3a}(1, -\sqrt{3}). \quad (1.2)$$

As in real space, the structure in reciprocal space is a hexagonal honeycomb lattice. Its orientation is rotated by 90° with respect to the structure in the real space (Fig. 1.1b).

The first Brillouin zone has then a hexagonal structure and exhibits a three-fold rotation symmetry. It has two types of corner points: the K and the K' points with the following coordinates in reciprocal space

$$K \left(\frac{2\pi}{3a}, \frac{2\pi}{3\sqrt{3}a} \right) \quad \text{and} \quad K' \left(\frac{2\pi}{3a}, -\frac{2\pi}{3\sqrt{3}a} \right). \quad (1.3)$$

These points are often referred to as "Dirac points". They are important to understand the electronic transport properties. Starting from a K point, no K' point can be reached using the lattice vectors \mathbf{b}_1 and \mathbf{b}_2 , hence the K and K' points are not equivalent.

Carbon nanotubes

Carbon nanotubes were first reported by S. Iijima in 1991 while attempting the synthesis of C_{60} fullerenes (5). Nanotubes can be either single-walled nanotubes (SWCNTs) made of one rolled-up graphene sheet or multi-walled carbon nanotubes (MWCNTs). Multi-walled nanotubes consist of many concentric nested SWCNTs.

The structure of SWCNTs is entirely determined by a pair of two integers (n, m) termed chiral indices. In order to eliminate redundancies in the tube structure, the chiral indexes have to verify the following condition: $n > m$. These two integers define the chiral vector \mathbf{C} in the unrolled graphene lattice. This vector is also referred to as perimetral vector or roll-up vector, since its absolute length gives the circumference of the tube.

$$\mathbf{C} = n \cdot \mathbf{a}_1 + m \cdot \mathbf{a}_2 \quad (1.4)$$

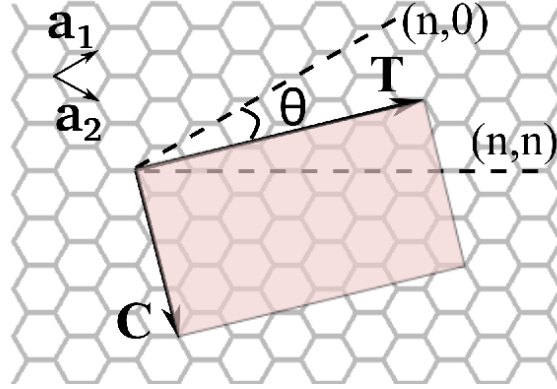


Figure 1.2: The Chiral vector \mathbf{C} and the translational vector \mathbf{T} defining the unit cell have been represented for a CNT (5,2) together with the chiral angle θ . The graphene lattice vectors \mathbf{a}_1 and \mathbf{a}_2 have been also indicated as well as the limit $(n, 0)$ and (n, n) for the chiral angle.

where \mathbf{a}_1 and \mathbf{a}_2 are the graphene lattice vectors. The tube diameter is then obtained by

$$d_{CNT} = \frac{|\mathbf{C}|}{\pi} = \frac{|\mathbf{a}_1|}{\pi} \sqrt{n^2 + nm + m^2} \quad (1.5)$$

The elementary cell is a rectangle defined by the chiral vector \mathbf{C} and the translational vector \mathbf{T} as seen on Fig. 1.2. The translational vector \mathbf{T} gives the length of the unit cell and runs parallel to the rolling axes. It is defined by

$$\mathbf{T} = t_1 \cdot \mathbf{a}_1 + t_2 \cdot \mathbf{a}_2 \quad (1.6)$$

with $t_1 = -(2m + n)/d_R$ and $t_2 = (2n + m)/d_R$ where d_R is the biggest common divisor of $(2n + m)$ and $(2m + n)$.

An additional parameter, the chiral angle θ defined as the angle between the chiral vector \mathbf{C} and the first lattice vector \mathbf{a}_1 , determines the helical chirality (i.e., how much the graphene structure is twisted before being rolled up). Because of the graphene lattice six-fold rotational symmetry, θ ranges from 0° to 30° . The way the graphene sheet is rolled up determines three sorts of tubes as shown in Fig.1.3:

- Zig-zag tubes have a chiral angle $\theta = 0^\circ$. The open ends of the rolled unit cell have a zig-zag configuration. These tubes are characterised by having the second chiral indice equal to zero ($m=0$), thus the chiral indice pairs are given by $(n, 0)$ (Fig. 1.3a).
- Armchair tubes correspond to the extreme case where $\theta = 30^\circ$. The open ends of the rolled unit cell show an "armchair"-like structure. The pairs of same chiral indices (n, n) characterise these tubes (Fig. 1.3b).
- Chiral tubes exhibit chiral angle $0^\circ < \theta < 30^\circ$. The edges of the unit cell do not show any particular arrangement. All indices combinations but the previously mentioned result in a chiral tube (Fig. 1.3c).

The SWCNT reciprocal lattice vectors can be written using the graphene reciprocal lattice vectors \mathbf{b}_1 and \mathbf{b}_2 . The first reciprocal lattice vector \mathbf{K}_1 is associated with the

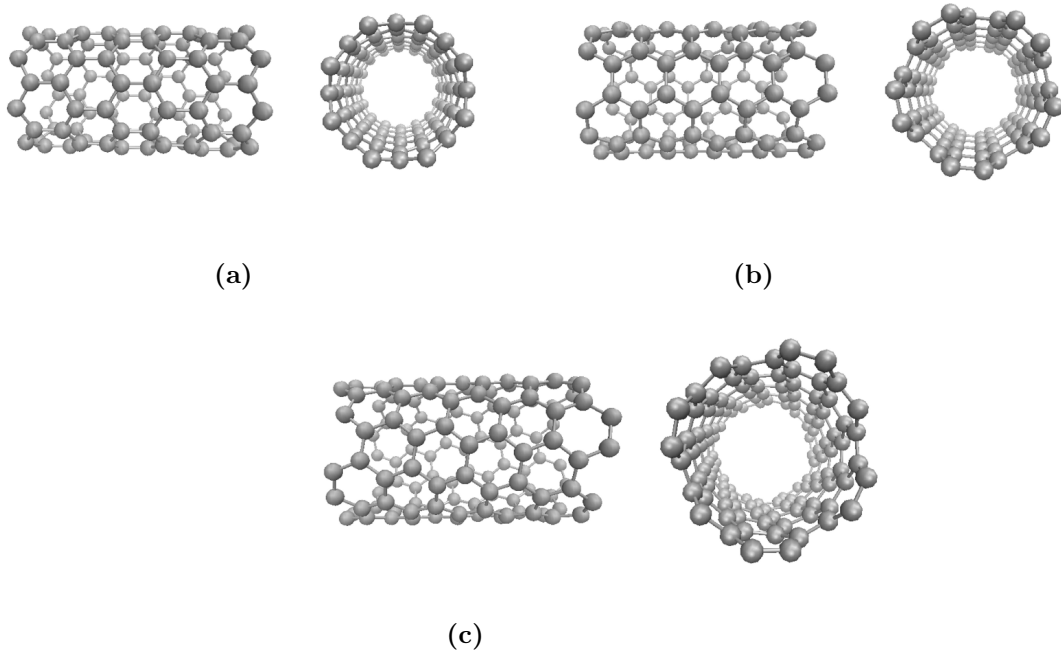


Figure 1.3: Structure of different CNTs depending on the chiral angle. A lateral view perpendicular to the axis and a view parallel to the axis are represented for each nanotubes. Fig.1.3a: Zigzag CNT (8,0). Fig.1.3b: Armchair CNT (5,5). Fig.1.3c: Chiral CNT (7,4).

chiral vector \mathbf{C} .

$$\mathbf{K}_1 = \frac{1}{N}(-t_2\mathbf{b}_1 + t_1\mathbf{b}_2) \quad (1.7)$$

where N is the number of hexagons in the tube unit cell defined by \mathbf{C} and \mathbf{T} . The reciprocal lattice vector \mathbf{K}_2 associated with the translational vector is given by

$$\mathbf{K}_2 = \frac{1}{N}(m\mathbf{b}_1 - n\mathbf{b}_2) \quad (1.8)$$

Because of the quasi-1D structure of the tube, the number of wave vectors allowed along the circumference of the tube is finite $p\mathbf{K}_1$ with p an integer ranging from 0 to $N - 1$. In the axis direction, since the tube is considered to be infinitely long, the value of the wave vectors is continuous. This results in a first Brillouin zone that contains N parallel $|\mathbf{K}_2|$ -long lines distant from each other by $\frac{2\pi}{|\mathbf{C}|}$.

1.1.2 Band structure

Graphene

The electronic band structure of graphene can be obtained in the tight-binding approximation. Two hopping processes are considered for the electrons: hopping to the nearest or to the next-nearest atom. To each hopping process is associated an energy, respectively t and t' determined by ab-initio calculations. Using the notation of (4), the Hamiltonian

reads

$$H = -t \sum_{i,j,\sigma} (a_{\sigma,i}^\dagger b_{\sigma,j} + Hc.) - t' \sum_{i,j,\sigma} (a_{\sigma,i}^\dagger a_{\sigma,j} + b_{\sigma,i}^\dagger b_{\sigma,j} + Hc.) \quad (1.9)$$

where the operators $a_{\sigma,i}^\dagger$ and $a_{\sigma,i}$ stand respectively for the creation and annihilation of an electron with spin σ on a site R_i in the sub-lattice A. The operator $b_{\sigma,i}^\dagger$ and $b_{\sigma,i}$ are defined for the electrons in the sub-lattice B. $Hc.$ stands for the hermitian conjugation of the term in the sum. Solving the Hamiltonian leads to the following energy dispersion relation for a wave vector \mathbf{k} (k_x, k_y) inside the Brillouin zone

$$E(\mathbf{k}) = \pm t \sqrt{3 + f(\mathbf{k})} - t' f(\mathbf{k}) \quad (1.10)$$

with

$$f(\mathbf{k}) = 2 \cos(\sqrt{3}k_y a) + 4 \cos\left(\frac{\sqrt{3}}{2}k_y a\right) \cos\left(\frac{3}{2}k_x a\right)$$

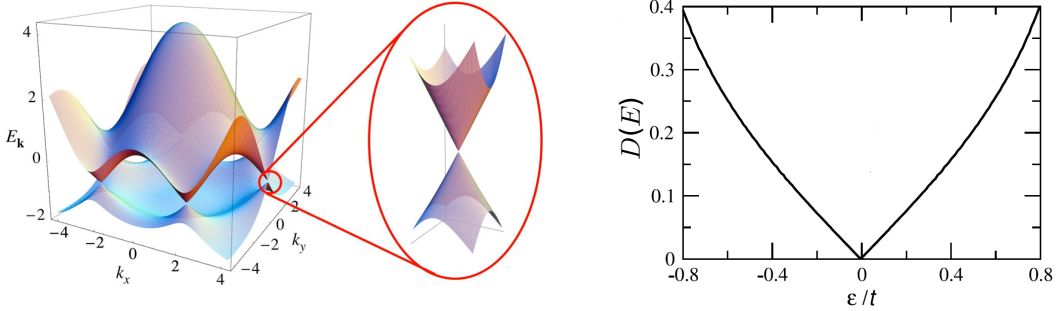


Figure 1.4: Left: Graphene conduction and valence bands with a close up around one of the Dirac points. The conduction and valence band are linear around the Dirac point. Right: Density of state near the Dirac point. Taken from (4)

As seen from the representation of the band structure in the first Brillouin zone (Fig. 1.4), the conduction and the valence bands touch at the corner of the Brillouin zone. These six corner points are the Dirac points (K and K' points). Because of the two inequivalent sub-lattices formed by the atoms A and B, the electrons are characterised by an additional degree of freedom termed valley isospin. For undoped graphene, the Fermi level crosses the Dirac points. Thus graphene is a semi-metal, its valence band is completely filled whereas its conduction band is empty, but it exhibits no band gap. The band structure around the Dirac point determines the electron transport properties.

A closer look at the energy dispersion around the Dirac points discloses a striking feature of graphene: the energy dispersion is linear instead of being quadratic as for usual crystals

$$E(\mathbf{q}) \approx \pm \hbar v_F |q| \quad (1.11)$$

where the reference for the wave vector \mathbf{q} has been taken from the Dirac point K and v_F is the Fermi velocity ($v_F = 3ta/2 \simeq 1 \times 10^6$ m.s⁻¹). Such linear energy dispersion is a feature of relativistic massless particles. The charge carriers in graphene around the Dirac point can hence be considered to behave as massless relativistic particles coined Dirac

1. BASIC PROPERTIES OF GRAPHENE AND CARBON NANOTUBES

fermions that move with the Fermi velocity v_F . The fact that two sub-lattices spawned by the atoms A and B allows the massless Dirac fermion to be described within a relativistic theory framework using the Dirac Hamiltonian

$$H = v_F \hbar \sigma \cdot \mathbf{k} \quad (1.12)$$

where σ is the 2D Pauli matrix and \mathbf{k} the wave vector.

It follows from the linear dispersion that the density of state $D(E)$ around the Dirac point is proportional to the energy

$$D(E) = \frac{2}{\pi} \frac{|E|}{(\hbar v_F)^2} (\simeq 0.09 \text{ eV}^{-2} |E| \text{ for } |E| < 1\text{eV}). \quad (1.13)$$

Graphene has consequently at the Dirac point, also labeled as neutrality point, no charge carrier.

Carbon nanotubes

SWCNT can show either metallic or semi-conductive behavior depending on their band structure. The graphene band structure is the starting point to obtain the SWCNT band structure. The chiral indices determine how the Brillouin zone of the tube cuts the graphene band structure. If the Dirac points are among the allowed states, the tube is metallic, otherwise it is semi-conductive.

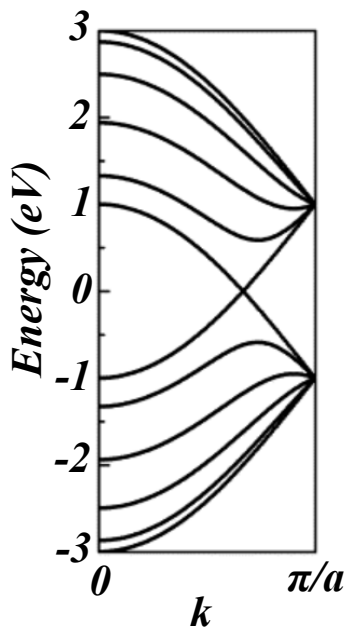


Figure 1.5: Band structure for a CNT (5,5) calculated in the tight binding approximation. Taken and adapted from (6).

The dispersion relation is obtained from that of graphene subject to the quantisation condition along the diameter of the tube

$$\mathbf{k} \cdot \mathbf{C} = 2\pi l \quad (1.16)$$

In this work, the nanotubes will be used as wires to connect graphene, only the metallic tubes are of interest for this task. The review is consequently restrained to metallic carbon nanotubes.

The condition on the chiral indices for the SWCNT to be metallic is

$$\mathbf{K} \cdot \mathbf{C} = 2\pi l \quad (1.14)$$

where \mathbf{K} is the vector in the reciprocal lattice giving the position of the Dirac point \mathbf{K} and l is an integer. This leads to the following condition for the chiral indices

$$n - m \equiv 0 \pmod{3} \quad (1.15)$$

Consequently, all armchair SWCNTs are metallic as well as one third of the zig-zag SWCNTs. The diameter of the tube d_{CNT} is inversely related to the band gap for semi-conductive SWCNTs $E_g \approx \frac{0.8 \text{ eV.nm}}{d_{CNT}}$. This relation implies that the outer-shell of MWCNTs is likely to be metallic already for thin MWCNT. An example of band structure for a metallic SWCNT is presented in Fig.1.7. More generally, the

where \mathbf{k} is the wave vector and l a integer.

1.1.3 Electrical transport properties

Transport in mesoscopic structures

The electrical transport in mesoscopic structures can be described in a semi-classical theory combining the Drude model together with the Boltzmann equation as long as the dimensions are large compared to the Fermi wavelength (7).

In the Drude model, the electrons are viewed as independent particles moving freely in a fixed ion lattice. The electrons interact with lattice defects by elastic scattering processes associated to a mean scattering time τ . If there is no external field \mathbf{E} , the electrons have no mean velocity. When an external field is applied, the electrons start to accelerate between each scattering event. Eventually, the mean velocity of the electrons reaches a saturation value $\langle \mathbf{v} \rangle$ given by $\langle \mathbf{v} \rangle = -e\mathbf{E}\tau/m_e$. The current density is proportional to the mean velocity and to the density of electron n , $\langle \mathbf{j} \rangle = -ne \langle \mathbf{v} \rangle$. Ohm's law is then found by replacing the expression of the mean velocity in the current density formula

$$\langle \mathbf{j} \rangle = \sigma \langle \mathbf{E} \rangle \quad \text{with } \sigma = \frac{ne^2\tau}{m_e} \quad (1.17)$$

where σ is the conductivity.

The Boltzmann equation can be used at this point to render the scattering processes in a more accurate and diverse way (8). The conductivity in this model is given by

$$\sigma = \frac{e^2}{2} \int d\epsilon_k D(\epsilon_k) v^2 \tau(\epsilon_k) \left(-\frac{\partial f}{\partial \epsilon_k}\right) \quad (1.18)$$

where f is the equilibrium Fermi distribution, $D(\epsilon_k)$ the density of states. The scattering time $\tau(\epsilon_k)$ depends now on the charge carrier energy ϵ_k . It is determined by solving the Boltzmann equation. Each scattering source is taken into account independently.

Graphene

Graphene exhibits three striking features: a strong response to perpendicular external electric fields, a transport "without charge carriers" at the maximum of resistivity and a high carrier mobility.

Since graphene is an only one-atom-thick arrangement of atoms, it differs from the 3D metal structures in its response to external electric fields. 3D metal structures usually screen the electric field by means of induced charge. The amount of induced charges is negligible when compared to the free-carrier concentration in the bulk. Because of the different dimensionality, the response of graphene should be much more significant. Indeed, graphene exhibits the ambipolar field effect as shown in Sec. 1.6. For pristine graphene, the Fermi level is at the Dirac point when no external field is applied. A voltage difference is applied between the graphene and a gate, thus modifying the electric external field.

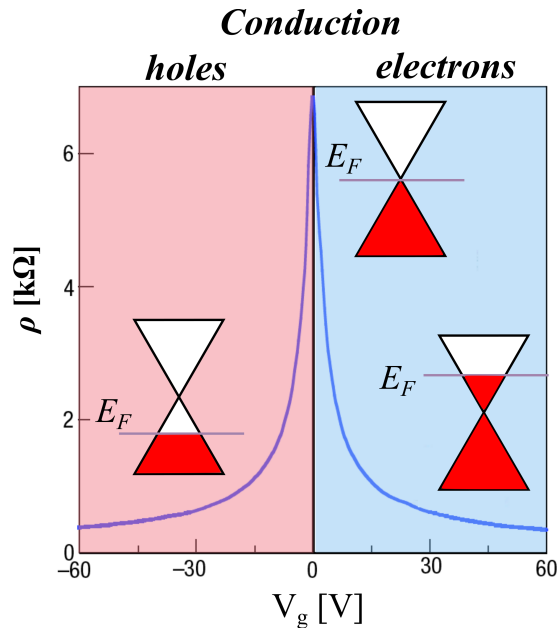


Figure 1.6: Ambipolar field effect in pristine graphene: the Fermi level is tuned by the applied gate voltage V_g . The resistivity is consequently modified, reaching a maximum at the Dirac point. In the pink (blue) zone, the transport is due to the holes (electrons). Taken and adapted from (9)

By sweeping the gate voltage V_g , the Fermi level in the graphene sheet is shifted from the Dirac point downwards (upwards) if $V_g < 0$ ($V_g > 0$) leading to p-doping (n-doping) of the graphene sheet. This determines the nature of the electrical transport. When the Fermi level is in the valence band ($V_g < 0$) or in the conduction band ($V_g > 0$), the transport is due to holes or electrons respectively.

The induced charge carrier concentration n is proportional to the applied gate voltage $n = \alpha V_g$. Thus by modifying the applied gate voltage, the charge density in the graphene sheet can be tuned (See Sec. 8.3 for the determination of α).

The graphene resistivity depends upon the charge carrier density as seen in Fig. 1.6. When the Fermi level corresponds to the Dirac point, the resistivity is maximum. This behaviour results from the density of state (DOS) in the graphene. At the Fermi level, the DOS is zero as inferred from Eq. 1.13 and as seen from Fig. 1.4. No state is available for the carriers, the resistivity is consequently large. Intuitively one would expect the resistivity to diverge but it shows a finite maximum value. This maximum value which constitutes a characteristic of Dirac fermions in 2D systems is still under discussion. Theoretical studies predict a value of $\frac{\pi\hbar}{4e^2}$ (10, 11, 12) while experiments reported values around $\frac{\hbar}{4e^2}$ (13). As soon as the Fermi level is shifted from the Dirac point, more states are available, the carrier concentration increases leading to a decrease the resistivity.

Graphene was assumed to be pristine until now, but the measured samples are far from this ideal case. Real graphene presents intrinsic doping due to structural defects as well as extrinsic doping due to external conditions (adsorbed molecules, charge transfer from the substrate,...). For doped graphene, when no external field is applied, the Fermi level is not

at the Dirac point but is shifted depending on type of doping. The Dirac point is reached for an applied gate voltage V_{Dirac} when the resistivity is maximum. The curve shown in Fig. 1.6 is then shifted horizontally, the maximum of resistivity being set for $V_g = V_{Dirac}$.

The carrier mobility μ links the drift velocity v_d , the speed with which the charge carriers move with the applied external electric field E : $v_d = \mu E$. The mobility is directly related to the conductivity σ by $\sigma = ne\mu$ where n is the charge carrier density. Although for pristine graphene the mobility does not depend on the charge carrier type, for doped sample it presents some asymmetry. Values for the mobility up to more than 200,000 $\text{cm}^2.\text{V}^{-1}.\text{s}^{-1}$ for free standing graphene (14) have been reported and a limit of 40,000 $\text{cm}^2.\text{V}^{-1}.\text{s}^{-1}$ is predicted for graphene on SiO_2 at room temperature (15). The difference in the mobility values is related to the amount of scattering centers in the sample.

Carbon nanotube

The conductance of the nanotubes is quantised at low-temperature taking values that are multiple of $G_0 = 2e^2/h$ the conductance quantum (with spin degeneracy). For metallic SWCNTs, the band structure indicates that near the Fermi energy two spin-degenerate bands are involved in the electronic transport. Two conducting channels are then available. In the ideal case, the conductance G is then given by $G = 2.G_0 = \frac{4e^2}{h}$ (16).

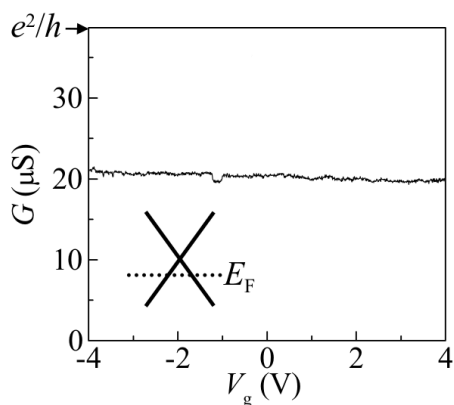


Figure 1.7: Conductance versus gate for a two terminal probe metallic SWCNT device at room temperature. Inset: Schematic view of the band structure and the position of the Fermi level. Taken from (17).

Bachtold *et al.* (18).

1.2 Connecting graphene

The properties of the junction formed between graphene and the connecting material have a dramatic influence on the performance of graphene devices. Thus understanding the parameters that govern the junction is crucial for further applications of graphene. In this section, characteristic properties of metal/graphene interfaces will be reviewed. Although several theories as well as experimental studies have been carried out, it still remains

At room temperature, for energies close to the Fermi level, the expected theoretical value $G = 2.G_0$ is not reached. The conductance of metallic tube does not change when the Fermi level is tuned as can be seen from Fig.1.7 but its value is limited by the quality of the contacts used to probe the tube. So the transparency of the contact for electron waves is a critical parameter to ensure a conductance value close to the theoretical value.

Since MWCNTs will be used in this work, it is worth to mention that in these tubes, the one or two shells most-outer define the transport properties since only these shells participate in the conduction process, as it has been shown by

1. BASIC PROPERTIES OF GRAPHENE AND CARBON NANOTUBES

unclear what parameters influence the transport at the metal/graphene junction. In addition, an overview of the published work on the electronic transport at CNT/graphene junctions will be presented. In contrast to the metal/graphene interface case, the CNT/graphene interface is a rather unexplored area. No specific theory has been reported up to now and only few measurements have been made.

1.2.1 Metal as leads

Work function

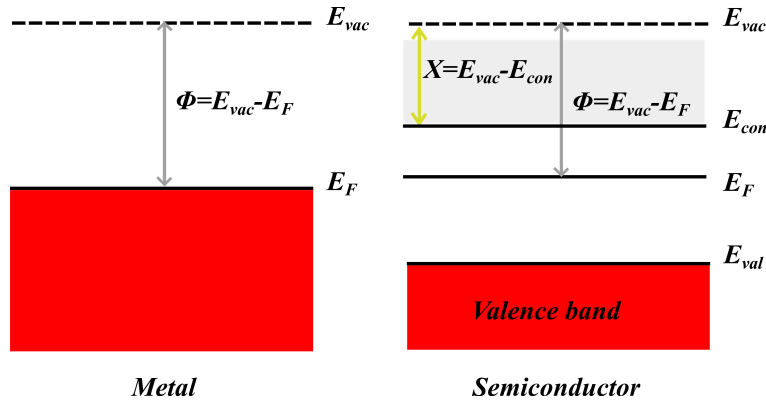


Figure 1.8: Definition of the work function ϕ for metal and semi-conductors. For the semi-conductor, the valence band (in red) and the conduction band (in grey) have been indicated. The electronic affinity has been indicated for the semi-conductor.

The work function is defined for metals as the energy required to remove an electron from the highest filled energy level and bring it outside the metal. The work function ϕ is then taken as the energy difference between the Fermi level and the vacuum level. For semiconductors, there is no electron at the Fermi level. Still, the work function is defined from the Fermi level, which lies in the gap. The value of the work function is not an intrinsic property of the semiconductor as it depends then on the doping. The electronic affinity χ , which is defined for semiconductors by the energy required to remove an electron from the bottom of the conduction band is in contrast an intrinsic property.

For pristine undoped graphene the work function value found in the literature is around 4.5-4.6 eV (19, 20, 21, 22, 23). The work function of graphene has been proven to be charge carrier density dependent with reported values ranging from 4.5 to 4.8 eV (24). Additional parameters may change the graphene work function, as for example strain due to the metal deposited (19). As for the carbon nanotubes, large-diameter SWCNTs and MWCNTs exhibit work function similar to that of graphene (21, 25).

Contact resistance between metal and graphene

When a metal/graphene junction is formed, the charge carriers transferred from one structure to another have to overcome a potential barrier. The hindering of the transport is reflected by the contact resistance that limits the device performances. Effects due to interfacial layers such as oxides or water contribute also to the contact resistance as well

as the interface roughness. The mechanisms contributing to the contact resistance have to be investigated and eventually controlled to make graphene reliable for electronic applications.

The transport in ideal metal/graphene junctions can be understood by using the Landauer-Buttiker formalism as presented extensively by S. Datta (26). The main idea is to model the charge carrier transport as a probability to transmit through the structure. Considering ballistic transport or coherent diffusive transport, the contact resistance R_c is given for ideal graphene-metal interface by the Landauer formula

$$\frac{1}{R_c} = \left(\frac{4e^2}{h} \right) \sum_{n=0}^M T_n \quad (1.19)$$

where e the elementary charge and h the Planck's constant. The spin and the valley degeneracies account for the factor 4 in the formula. The contact resistance is controlled by the number of conducting channels in the graphene M and by the transmission probability for the metal/graphene interface for each channel T_n .

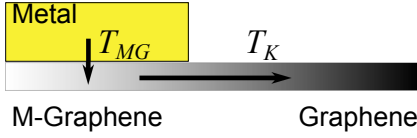


Figure 1.9: Schematic of the injection process model proposed by Xia et al. in (27).

Three different regions are considered: the coating metal, the graphene underneath the metal pad where the metal is adsorbed onto the graphene and finally the pure graphene region (27). The charge carrier transport at the junction is then seen as two successive sub-processes as depicted in Fig. 1.9, each of them associated with a transmission coefficient

- The transmission from the metal to adsorbed graphene region (referred to as M-graphene from now on). The transmission coefficient T_{MG} is determined by the coupling strength between the metal and the M-graphene.
- The transport from the M-graphene region to the pure graphene region. The electronic structure of the M-graphene as well as the doping level affects this transport process which is described by the transmission coefficient T_K .

When no reflection processes are considered, the total transmission for one channel is given by

$$T_{tot,n} = T_K T_{MG} \quad (1.20)$$

If the charge carriers are allowed to undergo reflections in both processes with following transmission coefficient $1 - T_{MG}$ (from the M-graphene to the metal) and $1 - T_K$ (from the graphene to the M-graphene), the total transmission for one channel $T_{tot,n}$ becomes (26)

$$T_{tot,n} = \frac{T_K T_{MG}}{(1 - (1 - T_K)(1 - T_{MG}))} \quad (1.21)$$

In order to account for real interfaces, the modification of the electronic structure of the graphene in the M-region is taken into account in the modified Landauer formula as well as random disorders modifying in the pure graphene region. The formula for the

1. BASIC PROPERTIES OF GRAPHENE AND CARBON NANOTUBES

contact resistance includes also the total transmission coefficient $T_{tot,n}$ and is given for a channel width W

$$\frac{1}{R_c} = \frac{4e^2}{h} \int_{-E_0}^{E_0} dE_1 f_1(E_1 - \Delta E_{FM}, \eta) \int_{-\infty}^{\infty} dE_2 f_2(E_1 - \Delta E_G) \frac{1}{W} \sum_{n=0}^{M_{mod}} T_{tot,n} \quad (1.22)$$

The first integral accounts for the M-region modified electronic structure. The density of states is model by the function f_1 that takes as parameter the doping level in the M-region ΔE_{FM} (i.e., the difference between the Fermi level and the Dirac point) and the coupling strength η . The energy E_0 characteristic of the bandwidth of d -orbital of transition metals ($E_0 \sim 1$ eV). The second integral renders the modification in the pure graphene channel by using the function f_2 as density of states that depends on the doping level in the pure graphene region ΔE_G .

To determine the characteristics of the two transmission processes involved in the charge transfer through the junction, the M-graphene region has to be investigated. The interaction between the metal and the graphene are the origin of the M-graphene region and are addressed in the next section.

Metal-graphene interaction

Connecting graphene with metal induces a charge transfer at the interface because of the Fermi-level difference. The charge transfer (or doping) occurring at the interface was thought to depend on the work function difference between the metal and the graphene $\phi_M - \phi_G$. Good contact should be then achieved by selecting metals with work function close to that of graphene. This assumption is contradicted by the experimental measurements. The contact resistance for copper/graphene contacts is one of the highest reported although copper has a work function close to that of graphene (~ 4.7 eV) (28).

Giovannetti *et al.* and Khomyakov *et al.* proposed a model to explain this discrepancy based on the type of metal/graphene interaction. They showed that the structure of the M-graphene underneath and around the metal can be significantly affected by the adsorbed metal, modifying consequently the work function in this region (22, 29). Thus the plain-metal work function should not be solely considered but the work function of the M-region ϕ_G to determine the doping level ΔE_F induced by connecting the metal

$$\Delta E_F = \phi - \phi_G \quad (1.23)$$

The modification of the graphene work function in the M-graphene region is determined by the charge reorganisation at the interface, which is mainly driven by the sort of interaction between the metal and the graphene. Therefore, Giovannetti *et al.* and Khomyakov *et al.* suggested to classify the connecting metals according to how they adsorb onto graphene:

- Physisorbed metals bind weakly to graphene (0.03-0.05 eV per carbon atom). The band structure of the graphene underneath the metal is preserved and the graphene

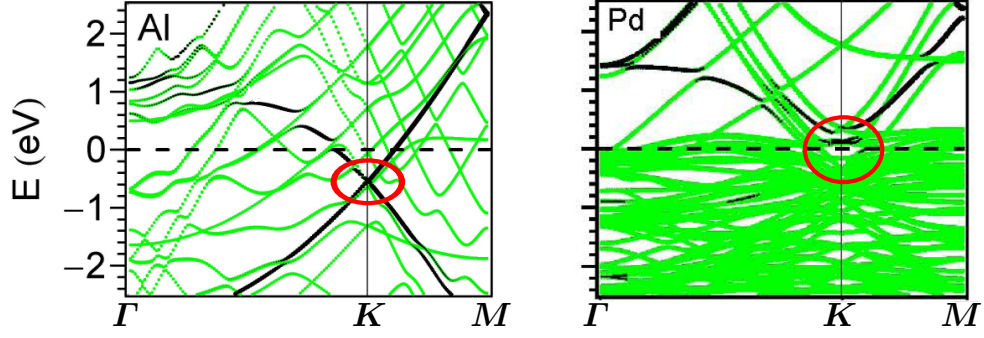


Figure 1.10: DFT Band structure calculations for two types of metals adsorbed on graphene. Left: aluminium contact. The graphene band structure is preserved (The Dirac point region is indicated with a red circle). Graphene is physisorbed on aluminium. Right: palladium contacts. The band structure of graphene is destroyed. Graphene is chemisorbed on palladium. Adapted from (22, 29).

Fermi level is shifted according to the charge transfer direction (Fig. 1.10 Left). Thus, the doping magnitude in the graphene ΔE_F can be inferred directly from the band structure. The work function ϕ for the M-graphene region takes into account two contributions: the charge transfer term $\Delta_{tr}(d)$ and the chemical interaction between the metal and the graphene term $\Delta_{chem}(d)$, which arises from Pauli's exclusion principle between the outermost s -orbital of the metal and the graphene π orbital (30). It is therefore strongly dependent on the metal-graphene distance d . ϕ is given then by

$$\phi = \phi_M - (\Delta_{tr}(d) + \Delta_{chem}(d)) \quad (1.24)$$

- Chemisorbed metals bind strongly to graphene by forming chemical bounds (0.05-0.4 eV per carbon atom). The metal d orbital and the graphene π orbital undergo a hybridisation process. This results in a graphene band structure that is significantly affected. The linear behaviour of the energy dispersion around the Dirac point vanishes (Fig. 1.10, right). The doping level cannot be inferred from the band structure anymore. The magnitude of the charge redistribution at the interface is higher than in the case of physisorbed metals, thus implying a larger modification of the M-graphene work function. The interaction process in the case of chemisorbed metal is still not well understood since no reliable model has been reported to compute the doping level and the covered-metal graphene work function for this case.

Table 1.1 gives for the usual connecting metal the sort of interaction with graphene.

Now considering the transmission process from the metal to the M-graphene, because of the weak interaction and the higher metal/graphene distance physisorb metals should be expected to show a lower transmission coefficient than the more strongly bonded chemisorb metals. For the M-graphene to graphene process, it is still not clear how the doping level influences the transport.

1. BASIC PROPERTIES OF GRAPHENE AND CARBON NANOTUBES

	Physisorbed	Chemisorbed
Connecting metal	Al, Ag, Au, Cd, Cu, Ir, Pt	Co, Ni, Pd, Ru, Ti
Binding Energy (per C atom)	0.03-0.05 eV	0.09-0.4 eV
Metal-graphene distance	$> 3.0 \text{ \AA}$	$< 2.5 \text{ \AA}$

Table 1.1: Classification of the usual connecting metals. The binding energies as well as the metal-graphene distances have been indicated. The results were taken from (30).

Contact resistance experiments

The results reported by Watanabe *et al.* (31) tend to substantiate the fact that chemisorbed metals are a better choice than physisorbed metals when it comes to establishing a contact to graphene. They carried out a contact resistance study for several types of connecting metals. Chemisorbed metals on graphene (titanium, palladium, nickel and cobalt) showed significant lower values for the contact resistance than the members of the physisorbed group (chromium, iron and silver). Robinson *et al.* measured the contact resistance for metal/gold contacts on graphene for titanium, copper, palladium, platinum and nickel (28). They showed that copper which belongs to physisorbed metal group, exhibited the highest contact resistance over one order of magnitude compared to the rest of the metals. But in the same study, the same range of contact resistance as the chemisorbed materials was observed for platinum which is a physisorbed metal on graphene, as demonstrated by DFT calculations by Khomyakov *et al.* (22) or by Slawinska *et al.* (32). The conclusion of the study are not consistent and do not validate the assumption that chemisorbed metals contact graphene better than physisorbed metals.

The study from Song *et al.* (33), displayed also some contradictory results. Indeed, the contact resistance at the metal/graphene interface was significantly higher for gold than for palladium, with about $10 \text{ k}\Omega \cdot \mu\text{m}$ difference. This observation could not be explained by considering the work function difference between metal and graphene, nor between covered-metal graphene and graphene since in both cases the difference was almost zero. The way graphene adsorbs onto these two metals is the key to understand the resistance difference. Gold binds only weakly to graphene through van der Waals forces (34, 35) while the binding between palladium and graphene is stronger and presents covalent bonding features (36, 37). The strong bond between graphene and the chemisorbed metals seems thus to insure low contact resistance. But the same study reports for two additional chemisorb metal onto graphene, chrome and nickel values about almost one order of magnitude higher or of the same range as for Gold.

This lack of consistency in the contact resistance value with no clear trend is found again in the literature. Besides the adsorption process, several parameters seem to contribute to the contact resistance in an uncontrollable fashion, such as the fabrication process or the measurement conditions, leading to a wide range of values even for the same metal as seen from Table 1.2. As an example, photo-resist residues used for standard lithography processes may contaminate the graphene device and increase the contact resistance by a factor of 6000 (28). Additionally, the measurements report different effect

for the gate: some studies claim that the contact resistance depends on the gate voltage while others observe no change with the gate for the same metal.

Metal	R_C ($\Omega \cdot \mu\text{m}$)	Experimental conditions	Gate dependence
Ni (38)	500	Thermal evaporation, T=300 K, Vacuum	No
Ni (39)	790 ± 300	Thermal evaporation, T=300 K, Ambient	Yes
Ti (40)	800 ± 200	Thermal evaporation, T=300 K, Ambient	No
Ti (41)	$500-2 \cdot 10^3$	(?), T=300 K, Ambient	Yes
Ti (38)	10^3-10^6	Thermal evaporation, 300K, Ambient	Yes
Pd (27)	185 ± 20	Thermal evaporation, 300K, Ambient	Yes
Pd (27)	120 ± 20	Thermal evaporation, 6K, Vacuum	Yes

Table 1.2: Contact resistance R_C as reported in the literature for several metals. The deposition technique, the measurement temperature and the gate dependence are as well indicated. For the contact resistance depending on the gate voltage, the minimum value is reported.

1.2.2 Multi-walled carbon nanotubes as leads

Motivation

The CNT/graphene junction presents several peculiar aspects. The first interesting point is the nature of the interaction between the two structures which is mostly due to the p_z orbitals, reason for terming the system as $\pi - \pi$ interaction system. The electric transport from a 1D system to a 2D system presents also an interesting. Until now, transport theory focused on for 2D metal contacts aspects where the contact geometry differs significantly from the CNT/graphene system.

Since the contact resistance limits the device performance, the inconsistency in the contact resistance measurements reduces the interest of integrating graphene in conventional or high-frequency electronic devices. As mentioned in Sec.1.2.1, the deposition technique is one of the many factors that might influence the contact resistance. During the deposition process, water, oxide layer or impurities can be trapped and influence the quality of the metal deposition. Since the deposition technique for metals and CNT differ, connecting the graphene with tubes could be viewed as a solution to eliminate or at least reduce the impact of undesirable contamination.

Moreover the interaction between CNT and graphene is weak. Therefore the tube should belong to the physisorbed materials class. Although it is still argued if chemisorbed metals constitute better connectors for graphene, the fact that graphene and metallic carbon nanotubes have similar structures could lead to more "homogeneous" junctions. This is reflected in the similar work functions that should lead to a reduced charge transfer at the interface and in consequence to a low contact resistance.

On a more device oriented perspective, connecting graphene with nanotubes could open the way to new fabrication processes. In fact, graphene and CNT can hold higher temperatures than the usual metals used as connecting leads. More importantly, CNT/graphene junctions could overcome the scaling down limitations of common device fabrication procedures such as lithography. Integrating CNT/graphene junctions could increase the device

1. BASIC PROPERTIES OF GRAPHENE AND CARBON NANOTUBES

density on a chip and therefore keep up with Moore's law that predicts an increase of the transistor density by a factor of two every 18 months. Finally, knowing the performances of CNT/graphene junctions is of great interest to progress toward the "all-carbon" electronics. Conversely, graphene could be used as electrode material to connect CNT which would constitute a step toward transparent electrodes.

Review of the published work

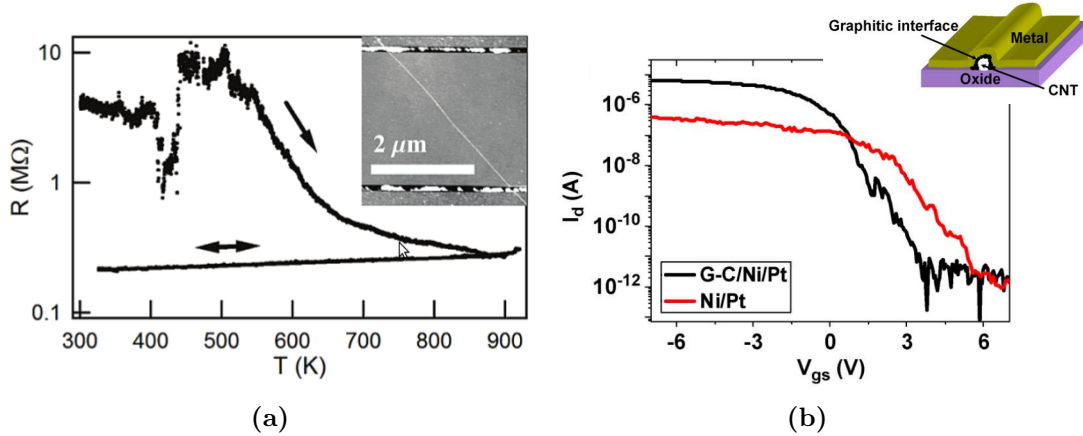


Figure 1.11: Fig. 1.11a: Temperature dependence of a CNT-Pt device resistance. An interfacial graphitic layer is synthesized at a temperature $\sim 880\text{K}$. Taken from (42). Fig. 1.11b: I_d - V_{ds} curves for CNT-Ni contacts with (black) and without (red) inter-facial graphitic layer. Taken from (43).

The first indications for CNT being good connectors for graphene were registered in the field of electric device production. Indeed, several studies reported improved performances after intercalating graphitic carbon layers, whose structure is related to graphene, between CNTs and the connecting metal (42, 43, 44). As seen from Fig. 1.11a, the resistance of a CNT-Pt device is probed with the temperature (measurement direction indicated by arrows). At a critical temperature ($\sim 880\text{K}$), a graphitic layer is formed between the CNT and the metal. With decreasing temperature, the resistance of the device remains low with weak temperature dependence. An other device made out of a CNT connected with palladium electrodes showed a significant increase of the On current, leading to an improvement in the On/Off ratio when graphitic carbon was used as interfacial layer (Fig. 1.11b).

Despite these hints at the CNT/graphene contact quality, only a few experiments have been carried on CNT/graphene junctions. A first study was reported for a similar system in 2000 by Paulson *et al.*. This work showed a lattice orientation dependence for the contact resistance at MWCNT/graphite junctions (45). An AFM tip was used to rotate a MWCNT on a highly oriented pyrolytic graphite surface (HOPG) and to measure the resistance at the interface. As seen from Fig. 1.12, the contact resistance exhibits a 60° periodicity indicating that the orientation of the MWCNT lattice with respect to the honeycomb HOPG lattice affects the electric transport. However, this study supposes

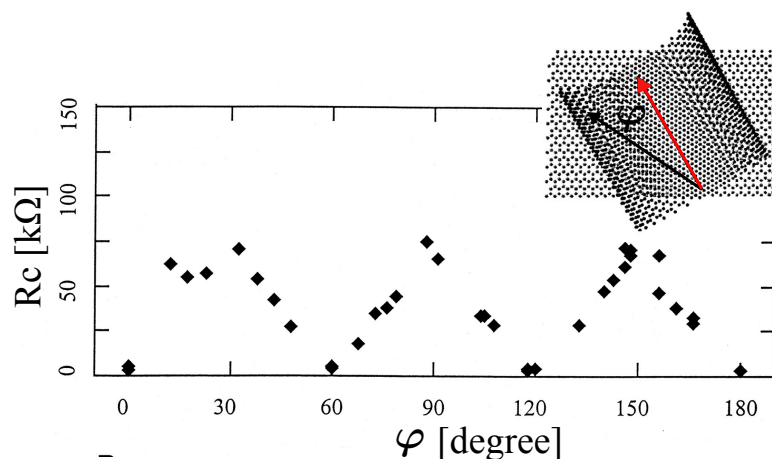


Figure 1.12: Contact resistance versus lattice alignment angle between the MWCNT and the graphite surface. The angle φ is measured from a reference position indicated by a red arrow in the inset. Adapted from (45).

that the MWCNT is a perfectly straight tube and that the AFM tip does not induce deformations while rotating the tube. These requirements are in practice hard to meet.

Only three studies focused on connecting graphene with CNTs. They tend to sustain that CNTs yield good connectors for graphene, because of the reduced contact resistance measured at the interface and the ohmic contact behaviour. In the first study, SWCNTs were connected with electrodes made of graphene oxide (rGO) that was chemically reduced to increase the conductivity (46). The report focuses mainly on the fabrication method which opens the way to build graphene devices without lithography steps by chemical deposition process (CVD) at high temperatures not withstood by the usual connecting metals. As seen in Fig. 1.13a, I-V measurements for SWCNT/rGO interface exhibit an ohmic behaviour and a resistance per length of tube of about $9 \text{ k}\Omega \cdot \mu\text{m}^{-1}$ that compares favorably with reported values (48). Although the junction is not made of pure graphene and the CVD process introduces impurities, the results give already a hint that CNTs could be a sustainable material to connect graphene. Another group reported connecting a thin film of unsorted SWCNT with mono- to few-layer graphene electrodes (49). The contact resistance at the interface SWCNT film/graphene was found to be negligible compared to the total resistance of the device.

In the most recent published study, I-V curves for a metallic SWCNT/graphene were measured (47). As presented in Fig. 1.13b, an ohmic contact behaviour can be observed as well as a saturation current close to the limit set by the optical phonon scattering ($\sim 25 \mu\text{A}$). A total resistance for the device of about $28 \text{ k}\Omega$ can be inferred from the I-V curves. The three studies miss an important characterisation for graphene devices. The measurements were made without tuning the carrier density in the graphene sheet. The position of the Dirac point and the type of doping were not determined, thus the charge carrier regime for which the measurements have been carried is unknown.

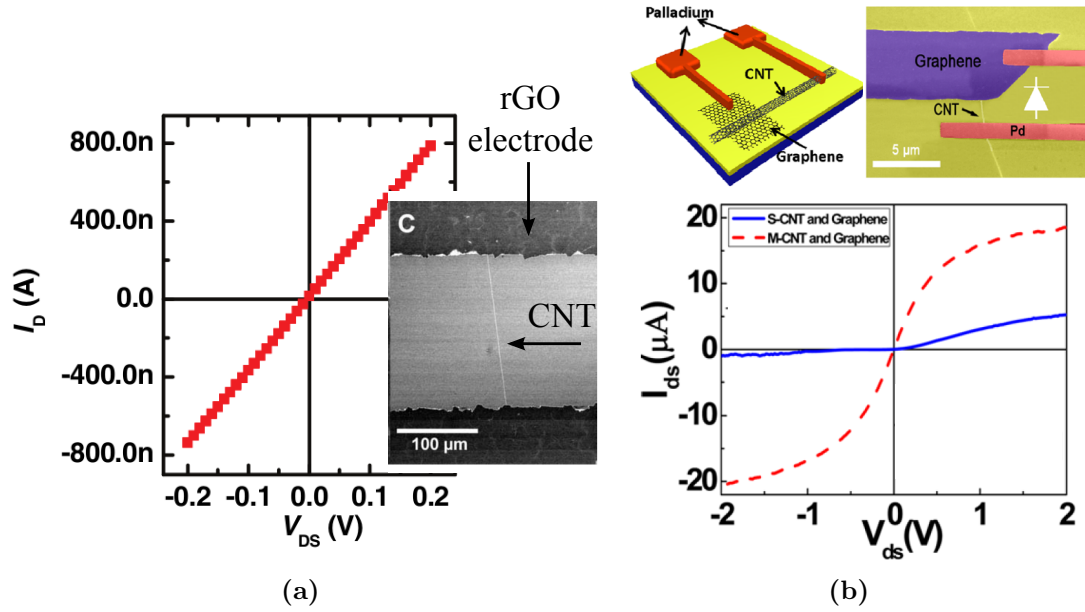


Figure 1.13: Fig. 1.13a: I-V curve for a SWCNT/reduced graphene oxide junction (shown in the inset). Taken from (46). Fig. 1.13b: I-V curves for metallic/few layers graphene junction (red curve) and for semi-conducting SWCNT/few layers graphene junction (blue curve). One side of the graphene has been connected with Palladium while the other side is formed by the SWCNT/few layers graphene junction part. Taken from (47).

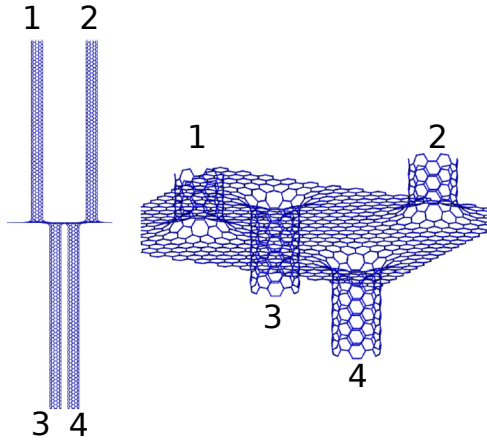


Figure 1.14: Example of SWCNT-graphene pillared structure. Taken from (50).

On the theory side, recently a study reported first-principle calculations for semiconductive SWCNT/graphene contacts, focusing mostly on the magnitude of the Schottky barrier at the interface (51). The barrier magnitude was found to be low (from 0.04 eV to 0.09 eV) compared to the values obtained for SWCNT/metal contacts (around 0.3 to 0.4 eV). Although these results were established for semiconductive nanotubes, they tend also to indicate that CNTs are suitable connectors for graphene.

It is worth to mention that the problem of CNT/graphene pillar systems has been addressed by several studies, a few focusing on electric transport properties (50, 52, 53) but mostly focusing on the hydrogen storage potential or other potential applications (54, 55, 56). In this configuration, CNT is attached to the graphene by a σ bond thus forming an homogeneous carbon cluster. Such a configuration presents a fundamental structural difference with that studied in this work where the bonding is not due to the π electrons. The electric transport properties are thus expected to differ greatly.

2

Structural properties

2.1 Introduction

In this part, the structural properties of sp^2 carbon-graphene systems are investigated by means of a semi-empirical quantum chemistry method. Two values are inferred from the calculations and are analysed: the equilibrium distance between the two graphitic systems and the adhesion energy. The equilibrium distance yields important information on the ground state geometry of the system. This value is of great importance because it will be used later on as input parameter for the charge distribution calculations (See Sec. 3 and 4). In addition, it is critical to understand the electronic transport properties for the carbon nanotube/graphene junctions (See Sec. 8.4). The adhesion energy indicates the strength of the binding between the subsystems.

Sec. 2.2 introduces the semi-empirical method used for the structural calculations. This class of methods relies on the Hartree-Fock method to solve the Schrödinger equation, using a parametrisation based on experimental parameters to speed up the calculations. A quick reminder on basic quantum physics as well as on the Hartree-Fock method is provided in Appendix. A. The description of the geometry used for the calculations and the results obtained are presented in Sec. 2.3.

2.2 Semi-empirical methods

Semi-empirical methods use the same framework as the Hartree-Fock method (See Appendix. A) to solve the Schrödinger equation but strive to scale down the computational effort by making at least two additional assumptions.

First, they focus on the valence electrons which are the electrons that are of interest in most cases. The core electrons are addressed together with the nuclei, bypassing the computation of the integrals involving them. For the valence electrons, the size of the basis set is held to a bare minimum. This minimum basis set contains only the occupied electronic orbitals when the atoms are in the ground state.

Speeding up the calculations is achieved as well by neglecting some of the most computational costly integrals appearing in the Fock matrix (See Eq. A.20 and Eq. A.21 in Appendix. A). This comes obviously at an accuracy cost that is offset by a parametrization of the remaining integrals based on experimental data.

2. STRUCTURAL PROPERTIES

2.2.1 NDDO method

The choice made for the neglected integrals is setting the various semi-empirical methods apart. All of these methods commonly do reduce to some extent the number of computed two-electron integrals, since these integrals are the most expensive to calculate. One way to go is actually to neglect the differential overlap between two atomic orbitals, meaning that the product of two atomic orbitals centered at different atoms is set to zero. Following the literature notation, the superscripts A and B are used to denote the atom at which an atomic orbital ϕ is centered. The previous assumption can be written: $\phi_\nu^A \phi_\mu^B = \delta_{AB}$. This assumption leads the overlap matrix \mathbf{S} to be a unit matrix. The Roothan-Hall equations (Eq. A.21) become:

$$\mathbf{F}\mathbf{c}_i = \epsilon_i \mathbf{c}_i \quad (2.1)$$

Additionally, all the integrals involving three or four different atoms as centres vanish. This approximation combined with the use of a minimal basis set, constitutes the neglect of diatomic differential overlap approximation (NDDO) (57). Although the number of integrals has been reduced, the one-centre and two-centre one-electron integrals as well as the one-centre and two-centre two-electron integrals still need to be evaluated.

For this purpose, a procedure known as modified neglected differential overlap (MNDO) was derived by Dewar and Thiel (58). The remaining non-zero integrals were not computed directly but instead parametrized in order to speed up the calculations. The parameters were obtained by fits based on both ab-initio results and experimental data bases as described in (58). Since the total energy is required, additionally to the electronic energy, a parametrization for the the nuclei repulsion term has been introduced.

2.2.2 PM6-D method

One of the most recent development in semi-empirical methods has been made by Stewart (59) with the MNDO derived PM6 method. In the PM6 method, data from up to 9000 chemical compounds were used to parametrize more than 80 elements. Although the PM6 performs well for systems driven by covalent bonds, significant discrepancies with experimental values were observed for non-covalent interactions such as hydrogen bonding and van der Waals forces.

Further improvements were presented by Rezac *et al.* (60) to render the non-covalent interactions in a more accurate way. In particular, a term was added to the Hamiltonian to account for the London dispersion forces. Such forces arise from the interaction between instantaneous atomic dipoles (or higher order multipoles) and therefore constitute one part of the van der Waals interaction. The dispersion forces are weak attractive long-ranged intermolecular interactions whose magnitude is up to a few hundreds of meV. The PM6 method with the London dispersion term included is termed as PM6-D. From the results drawn from Sec. 2.3.3, the van der Waals forces will play a crucial role in the binding between sp^2 -carbon structures. The good performance of the PM6-D method with the van der Waals interaction constitutes a decisive criterion for choosing this method over the rest of the semi-empirical methods.

The term implemented by Rezac *et al.* is reproduced here as it was first described in (61):

$$E_{dis} = - \sum_{i,j} f_{damp}(r_{i,j}, R_{i,j}^0) \frac{C_{6,i,j}}{r_{i,j}^6} \quad (2.2)$$

The dispersion energy is a pairwise addition of damped atomic contributions proportional to $r_{i,j}^{-6}$, where $r_{i,j}$ is the inter atomic distance. In the dispersion energy, the higher-order expansion terms are neglected. The atomic dispersion coefficients C_6 used have been determined for each atom species by Grimme (62) and, in the case of carbon, are well suited to describe sp^2 hybridized carbon. A damping function f_{damp} weights the atomic contribution in order to avoid divergence for small inter atomic distances. In addition to the inter atomic distance, the damping function takes as argument the van der Waals radius R^0 . Two parameters fitted with dispersion-driven molecule data set were introduced in the damping function to reproduce experimental results.

2.3 Equilibrium distance

2.3.1 Geometry description

The self-consistent-field (SCF) calculations were carried using the MOPAC2009 package that includes the PM6-D method (63). The structures used for the calculations were all constructed by defining a large unit cell ranging from 500 atoms to 1500 atoms (upper limit of MOPAC2009). By giving to MOPAC2009 boundary conditions along the three space coordinates, the calculations have been performed for the entire 3D structure.

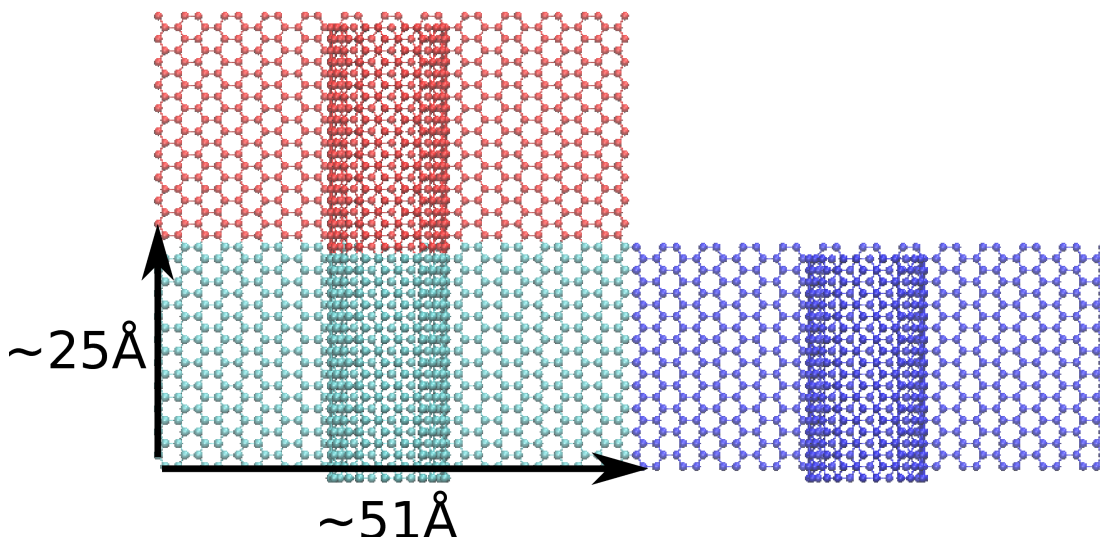


Figure 2.1: 3 Unit cells used for the MOPAC calculation. The structure is made of a CNT (9,9) and a graphene sheet. The translation vectors used in order to set the boundary conditions are represented only in the in-plane directions.

Each unit cell was made of two elements as seen of Fig. 2.1:

- a piece of graphene with a width of about 50-60 Å and a length of about 22-25 Å.

2. STRUCTURAL PROPERTIES

- a piece of carbon nanotube that has the same length as the graphene sheet.

Translation vectors were defined for both in-plane coordinates x and y in order to construct the whole system.

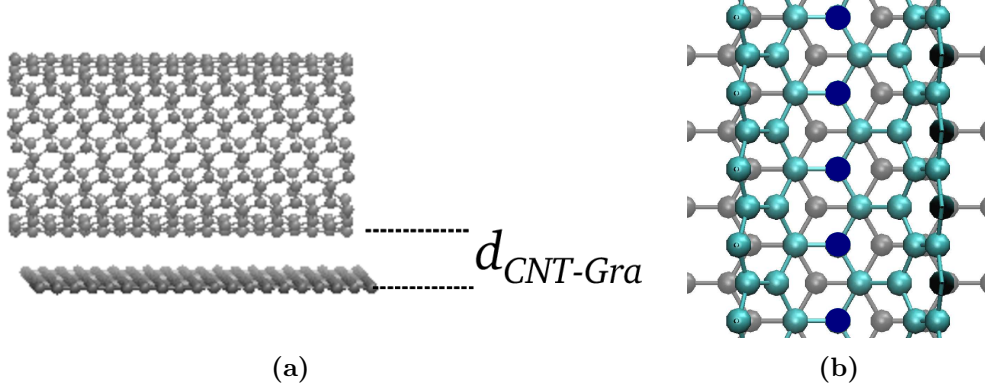


Figure 2.2: Fig. 2.2a: View of one unit cell. The distance between CNT and graphene has been labeled with $d_{CNT-Gra}$. Fig. 2.2b: Alignment of the CNT (blue atoms) and the graphene (gray atoms) lattice. The deep blue atoms are the closest atoms to the graphene and are the ones that are A-B stacked with the graphene atoms.

To ensure CNT-CNT inter cell interactions to be negligible, the spacing between two CNT was taken large enough (for example around 4 nm for the CNT (9,9)). The CNT was placed on top of the graphene sheet at a distance $d_{CNT-Gra}$ using the A-B stacking depicted in Fig. 2.2 for the orientation of the tube with respect to the graphene sheet for all calculations. For the row of CNT atoms closest to the graphene, the atoms were placed at the center of an hexagon formed by the graphene atoms.

The optimization of the geometry (i.e., the relaxation of the system) is a critical step in order to ensure a satisfying convergence. This has been achieved by means of the EigenFollowing (EF) algorithm in the framework of the Newton-Raphson method (64, 65). Relaxation has been first performed on each element of the unit cell separately. Each atom of the graphene was allowed to relax in the in-plane directions. For the carbon nanotube, each atoms except those of the very bottom row of atoms was allowed to relax in the each three spatial coordinates. Since the atoms of the very bottom row are taken as reference for the definition of the distance carbon nanotube-graphene $d_{CNT-Gra}$, the vertical coordinate ($z=cst$) for this row was fixed and the two other coordinates were free to relax. The optimized geometries obtained after this step, were used together as input to perform a new SCF calculation.

2.3.2 Binding energy

Since the equilibrium distance d_{eq} between the CNT and the graphene sheet is determined by the binding energy minimum, the procedure for calculating this energy is explained in this part. For a CNT lying on top of a graphene sheet at a distance d , the total energy is

labeled $E_{Gra+CNT}(d)$ and the binding energy $\Delta E_{Bin}(d)$ is defined by

$$\Delta E_{Bin}(d) = E_{Gra+CNT}(d) - E_{Gra+CNT}(\infty) \quad (2.3)$$

where $E_{Gra+CNT}(\infty)$ is the total energy when there is no interaction between the CNT and the graphene. This formally corresponds to the subsystems being located at an infinite distance from each other. While $E_{Gra+CNT}(d)$ is retrieved directly from the MOPAC2009 output, extracting $E_{Gra+CNT}(\infty)$ requires more effort. Indeed, the trivial approach defining $E_{Gra+CNT}(\infty)$

$$E_{Gra+CNT}(\infty) = E_{Gra,0} + E_{CNT,0} \quad (2.4)$$

as the sum of $E_{Gra,0}$ and $E_{CNT,0}$ which are respectively the total energy for the graphene and the CNT calculated separately, is wrong because of the basis set superposition error that arises for SCF methods using finite basis sets. The SCF calculations for $E_{Gra,0}$ and for $E_{CNT,0}$ use actually a more restrained basis set of function than the SCF calculations for $E_{Gra+CNT}(d)$. A procedure was established to sidestep this technical hurdle. In order to evaluate $E_{Gra+CNT}(\infty)$, SCF calculations were run for the CNT located at a very large distance to the graphene sheet (typically about a few nanometers), insuring no CNT-graphene interaction but at the same time using the same set of basis function as for the computation of $E_{Gra+CNT}(d)$.

As experimental measurements of the CNT-graphene distance have yet not been performed, the value drawn on for the sake of comparison is the adhesion energy. Indeed, experimental values measured using an AFM are available for CNT/graphene systems (66). The adhesion energy E_{adh} is merely defined as being the minimum value of the binding energy. In the literature, two normalizations for E_{adh} are found: either the contact length is used as normalization factor or the number of atoms taking part in the binding. The first normalization procedure is preferred here, since the second one requires counting the binding atoms which is not straightforward considering the geometry of the system.

2.3.3 London dispersion forces

MOPAC2009 output yields besides the total energy, the dispersion force contribution E_{dis} to the total energy. Since the binding energy computed by the PM6 method $\Delta E_{Bin,PM6}$ and by the PM6-D method $\Delta E_{Bin,PM6-D}$ are related by

$$\Delta E_{Bin,PM6-D} = \Delta E_{Bin,PM6} + E_{dis} \quad (2.5)$$

the role of the dispersion force in CNT/graphene hybrid structures comes out clearly by comparing both $\Delta E_{Bin,PM6}$ and $\Delta E_{Bin,PM6-D}$ for the same structure.

As seen in Fig. 2.3, when the dispersion term is disregarded ($\Delta E_{Bin,PM6}$ green curve), the value for the equilibrium distance is close to that found in the literature for the interlayer distance in multilayer graphene (i.e., around 3.34 Å). In addition, the PM6 results indicate a very weak binding between the CNT and the graphene. The adhesion energy for the PM6 method is found to be at least an order of magnitude smaller than the

2. STRUCTURAL PROPERTIES

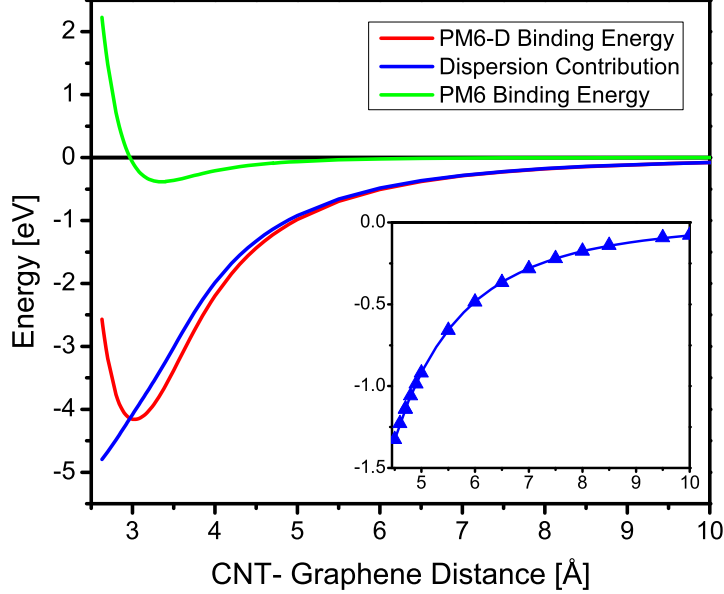


Figure 2.3: Binding energy computed with and without including the London dispersion term as well as the individual contribution of the London term. All energies are plotted versus the CNT-graphene distance. The calculation was done for a CNT (5,5). Inset: Fit of the dispersion energy tail. The dots represent the computed values and the solid line represents the power law (Eq. 2.6).

experimental values (66). For the CNT (5,5)/graphene system, the length of the unit cell corresponds to the contact length (i.e., about 25 Å), consequently the adhesion energy lies around 0.015 eV/Å.

When the dispersion term is taken into account ($\Delta E_{Bin,PM6-D}$, red curve in Fig. 2.3), the equilibrium distance value shifts toward lower values. For the CNT (5,5), the equilibrium distance found is around 3.02 Å. Moreover the binding is stronger since the adhesion energy E_{adh} is around 0.17 eV/Å and lies now in the experimental value range. This result corroborates thus the essential role played by the dispersion forces in the CNT/graphene binding.

Now focusing on the dispersion contribution E_{dis} , represented in Fig. 2.3 (blue curve) for a CNT (5,5)/graphene system, this long-ranged contribution outweighs the rest of the interactions in the attractive part of the binding energy and accounts for most of the attractive forces. For large inter-structure distances ($d_{CNT-gra} > d_{eq}$), the tail of the dispersion energy presents an algebraic decay. Indeed, for such distances, the dispersion term can be regarded as a sum of undamped r^{-6} inter atomic contributions (see Sec. 2.2.2). The integration carried out over the whole structure determines the resulting asymptotic power law that governs the attractive interaction between the sub-structures.

A short review of the power law for several parallel structures is found in (67, 68) for example and is reproduced in Table 2.1:

System	Power law
Thin wires (1D)	$1/d^5$
Thin plates (2D)	$1/d^4$
π -conjugate layers	$1/d^4$
Thick plates (3D)	$1/d^2$

Table 2.1: Asymptotic power law for several parallel structures. d denotes the subsystems separation after (67, 68).

Since the CNT(5,5)/graphene system involves two substructures with different dimensionality, the anisotropy hinders a straightforward integration of the inter atomic contributions. The resulting power law has been thus determined by a fit of the tail:

$$E_{dis} \propto -\frac{C_6}{d^\alpha} \quad ; \quad C_6 = 260 \text{ and } \alpha = 3.5 \quad (2.6)$$

The numerically obtained exponent $\alpha = 3.5$ does not relate to any of the structures listed in Table 2.1. The asymptotic interaction energy for CNT/graphene systems presents thus a different behaviour contrasting with the usual structures, giving therefore already a glimpse of the peculiarities of such system.

2.3.4 Curvature effect

Contrary to the multilayer graphene case, where all atoms are binding atoms, in CNT/graphene systems, because of the curvature, the only atoms that actually participate in the binding are restricted to a region around the CNT. Thus the stretching of the binding π orbital due to the neighboring atoms should be limited. Consequently the equilibrium distance should be smaller than the one for multilayer graphene.

This statement is clearly verified as the equilibrium distance for CNT (5,5), (9,9) and (15,15) inferred from Fig. 2.4 ranging from 3.02 Å for (5,5) to 3.06 Å for (15,15), is significantly smaller than the graphite interlayer distance 3.34 Å. The adhesion energy ranges from 0.17 eV/Å to 0.27 eV/Å as shown in Table 2.2.

CNT	d_{eq} [Å]	E_{adh} [eV/Å]	R_{cnt} [Å]
(5,5)	3.02	0.17	3.44
(9,9)	3.04	0.21	6.19
(15,15)	3.06	0.27	10.31

Table 2.2: Computed equilibrium distance and adhesion energy for CNT (5,5), (9,9) and (15,15). The radius is indicated for each CNT.

In addition, this result reveals a radius-equilibrium distance correlation. Indeed, since the CNT (n, n) radius increases with the chiral index: the larger the radius of the CNT, the larger the equilibrium distance. This correlation confirms actually the fact that the more atoms participate in the binding, the more important are the repulsive forces. The dispersion forces are not significantly affected by such short-ranged scale changes in the structures. A second correlation can be inferred considering the adhesion energies and the CNT radii. The binding becomes stronger for larger CNT as more atoms are involved in

2. STRUCTURAL PROPERTIES

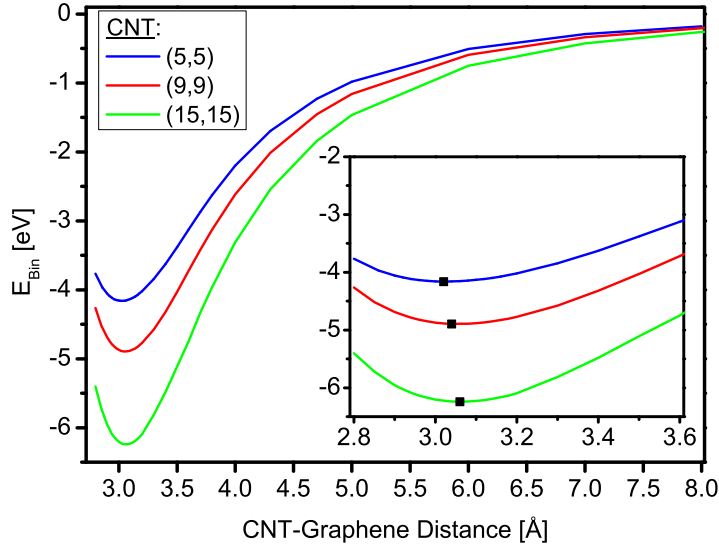


Figure 2.4: Binding energy versus the CNT/graphene distance for CNT (5,5), (9,9) and (15,15) /graphene systems. Inset: Zoom around the minimum of binding energy. The black dots correspond to the minimum of binding energy.

the binding. The binding energy should then have as limit, in the case of a CNT of infinite radius, the graphene-graphene interaction value.

Focusing on the whole sp^2 -carbon/graphene structure, the bilayer graphene gives the upper limit for the repulsive force and for the equilibrium distance while the fullerene adsorbed on graphene gives the lower limit for both values, as shown in Fig. 2.5. The equilibrium distance exhibited a stepwise change with the dimensionality modification of the adsorbed structure. Calculations for the C_{60} fullerene were carried using the procedure described in Sec. 2.3.1 with the unit cell drawn in the inset of Fig. 2.5. For the bilayer, the results were established by F. Symalla (69).

The results of the calculations are in good agreement with previous works based partly on the LCAO- S^2 + vdW method (66, 70) where local-orbital DFT is combined with intermolecular perturbation theory to render the van der Waals interaction as presented in (71). Other studies use the molecular mechanics frame (MM+) and render the van der Waals forces with an adapted Lennard-Jones potential, whose repulsive part is described by an exponential term instead of the usual r^{-12} term (72).

Method	d_{eq} [Å]	E_{adh} [eV/Å]
PM6-D	3.02	0.17
MM+ (72)	~ 3.2	0.21
LCAO- S^2 + vdW (66)	~ 2.9	0.33

Table 2.3: Equilibrium distance and adhesion energy for CNT (5,5) computed using different methods.

Table 2.3 shows that indeed each calculation predicts an equilibrium distance signifi-

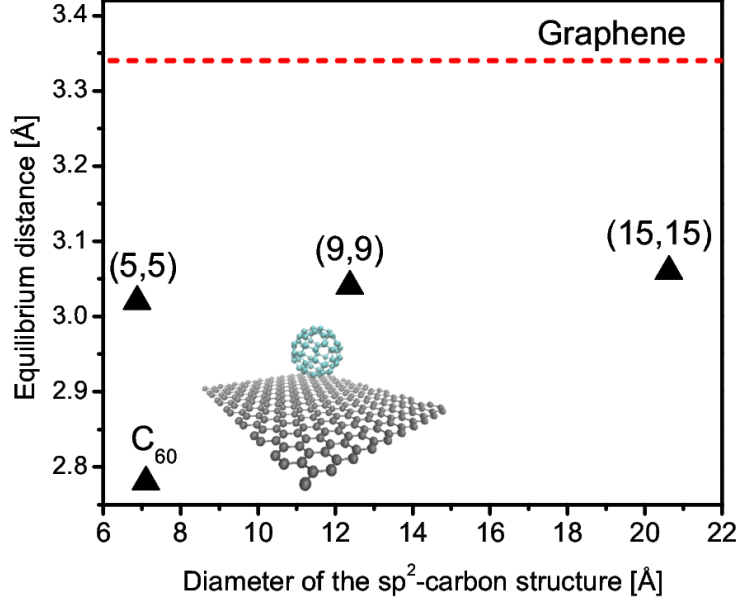


Figure 2.5: Equilibrium distance for several sp^2 -carbon structures adsorbed on graphene. Inset: Unit cell used for the C_{60} /graphene calculations.

cantly lower than for the graphene-graphene case. For the adhesion energy, the method PM6-D yields lower values than the two other methods, in particular when compared to the LCAO-S² + vdW method. Since the former method uses an unscreened term to account for the van der Waals forces, it overestimates at short distances their contribution and therefore gives a lower equilibrium distance and a higher adhesion energy.

Nevertheless, the results obtained with the PM6-D method compares well to the values presented in the experimental part of (66). The adhesive energy could be inferred between a CNT and a graphene surface by mean of an atomic force microscope with a CNT attached to the tip and by recording the approach and retract curves. The experimental values lie between $0.13 \text{ eV}/\text{\AA}$ and $0.47 \text{ eV}/\text{\AA}$ for long nanotubes ($l > 100 \text{ nm}$).

For further applications (see Sec. 3.3 and Sec. 5.1), the equilibrium distance was calculated for CNT (n, n) with chiral index up to $n = 50$.

The data obtained with MOPAC for the tubes CNT $(5,5)$, $(9,9)$ and $(15,15)$ have been used make a crude extrapolation by assuming that

$$d_{eq} = d_0 + A \exp\left(-\frac{R}{R_0}\right) \quad (2.7)$$

with d_{eq} the equilibrium distance for a CNT with a radius of R . The limit for the equilibrium distance was set to be the graphene-graphene distance (i.e., $d_0 = 3.34 \text{ \AA}$). The parameters A and R_0 were determined by the extrapolation: $A = -0.34 \text{ \AA}$ and $R_0 = 103 \text{ \AA}$. The equilibrium distance for a CNT $(50,50)$ that has a radius of $\sim 34 \text{ \AA}$ is about 3.16 \AA . Thus, for over an order magnitude increase for the radius, the equilibrium distance in-

creased by approximately 0.14 Å.

2.4 Conclusion

The results of structural calculations have been presented in this part. The semi-empirical PM6-D method based on the neglect of diatomic differential overlap approximation (NNDO) and implemented in the code MOPAC2009 has been used to determine the interactions in different graphitic structures with emphasis on the CNT/graphene systems.

First, the calculations showed that the dispersion forces make a prominent contribution to the binding between CNT and graphene that is reflected in the strength of the binding and the equilibrium distance. Neglecting the dispersion force or not taking it properly into account, leads to nonphysically weak bonding. The asymptotic behaviour for the dispersion forces was found to follow a $1/d^{3.5}$ power law contrasting with the usual power laws.

The equilibrium distance between sp^2 -carbon structures and graphene showed a significant dependence on the dimension of the involved sp^2 -carbon structures. For CNT, the computed distance was found to be around 3.02 to 3.06 Å. As for the strength of the binding given by the adhesive energy, the value led approximately between 0.17 eV/Å to 0.27 eV/Å. The radius dependence of both structural values has been analysed and the following trend could be drawn: the more atoms participates in the binding, the strongest the binding grows and the further apart the substructures are.

Finally, the equilibrium distance has been inferred by from the computed data for larger CNT. A fitting step has been performed in order to overcome the computational limitations. An equilibrium distance up to 3.16 Å has been found for the largest CNT with a radius of 3.4 nm.

3

Analytical calculations

This part addresses the charge redistribution in the graphene sheet that occurs when building a CNT/graphene junction. Both substructures are held at a different potentials. For example, during the measurement process, the electric potential difference between graphene and carbon nanotube may vary, in particular if graphene is back-gated as it is in common transport measurement technique. From an electrostatic point of view, this leads to a modification of the charges distribution when the structures are brought close to one other. A picture of the charge redistribution is essential to understand the charge transport in the junction. Indeed, the injected charges have to "move" across the energy landscape arising from the charge redistribution.

A special focus has been put on the influence of CNT on the charge distribution in the graphene sheet. Indeed, connecting graphene with metal electrodes leads to significant charge transfer which at the interface extends over a significant distance into the non-contacted graphene sheet. The electrostatic models used for the calculations show that the charge redistribution in case of a CNT used as electrode has a reduced extension in the graphene sheet.

First a 2D electrostatic model has been used to calculate the charge distribution in the graphene sheet when the CNT is placed on top of it. To obtain the charge density, the Laplace equation with specific boundary conditions is solved by applying the conformal mapping technique (73). The inferred potential yields then the charge density on the graphene sheet. The results are analyzed along with the influence of geometrical parameters such as the tube radius.

3.1 Laplace Equation

Assuming the graphene sheet is an infinite plane and the CNT is an infinitely long cylinder of radius $R_{cnt,0}$, the system can be reduced to a 2D system by considering the cross section perpendicular to the CNT axis. The graphene is consequently modeled by an infinite straight line parallel to the x-axis and the CNT by a circle of radius $R_{cnt,0}$ placed at a distance $R_{cnt,0} + \epsilon$ above the graphene. The values for ϵ were taken from Sec. 2.3.4. For convenience, in the rest of this part, we will focus on CNT (n,n) i.e., armchair tubes, with n being an integer, and we approximate the circumference of the CNT by a circle.

3. ANALYTICAL CALCULATIONS

This simplification is justified in the continuum approach we are taking, neglecting the structural arrangement of the atoms in the CNT and in the graphene.

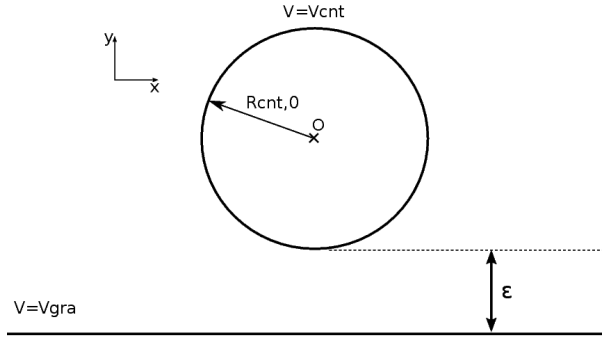


Figure 3.1: Initial geometry. The graphene was modeled by a straight line, the CNT by a circle of radius $R_{cnt,0}$.

Conventional variable separation method for solving the Laplace equation works for few simple geometries as rectangles or disks. The geometry of the CNT/graphene problem is already too complicate to try the variable separation method. This is confirmed in hindsight by the potential expression found which is not a product of two functions of independent variables.

A diagram of the initial geometry is shown in Fig 3.1. The graphene is set to a potential V_{gra} , while the CNT is set to V_{cnt} . The reference point for the potential has been taken at infinity. These boundary conditions and the Laplace equation

$$\nabla^2 V = 0 \quad (3.1)$$

determine the electrostatic potential V for the geometry described above. The Laplacian operator ∇^2 is defined in the

Cartesian coordinates (x,y) .

3.2 Conformal mapping technique

3.2.1 Conformal transformations

The conformal mapping technique described in the following part is used to map an inconvenient geometry to a new geometry. The electrostatic problem is then solved for the new geometry and the inferred solution is transformed back to the original coordinates, yielding the solution to the initial problem.

On an intuitive level, conformal transformations are "smooth" transformations which preserve the local angles and the sense of rotation, thus introducing no local distortion in the resulting mapped region.

The Laplace equation is known to be invariant under conformal transformation (see (73) for a proof). This assertion implies that if a function $\phi(x, y)$ satisfies the Laplace equation, then the function in the mapped region, $\psi(u, v)$ so that $\phi(x, y) = \psi(u(x, y), v(x, y))$ is also solution of the Laplace equation. The interest of the conformal mapping technique becomes clear. If the Laplace equation is too tedious to be solved for a given geometry, the conformal mapping technique allows to solve it for a new and easy geometry, providing that a conformal transformation mapping exists from the initial geometry to the new one.

3.2.2 Laplace Equation solution

Two conformal maps were applied to the initial geometry depicted in Fig. 3.1. The first transformation maps the initial circle and the initial line into two non concentric circles

shown in Fig. 3.2 a). While the second one maps two non concentric circles into two concentric circles. The final geometry is drawn in Fig. 3.2 b).

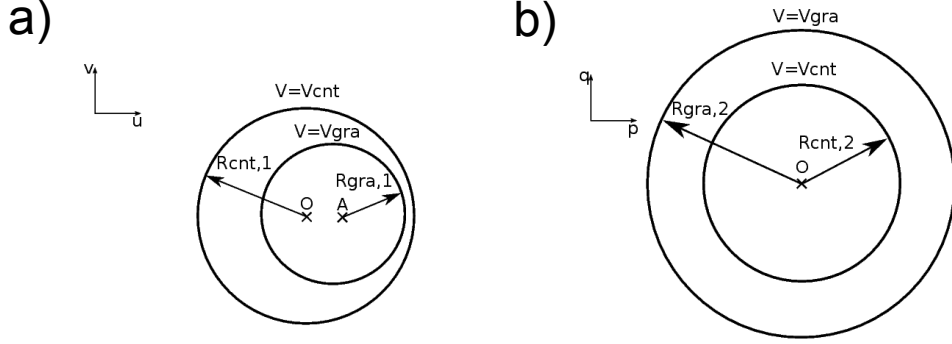


Figure 3.2: a): Geometry obtained by applying the first conformal map $G(z)$.
b): Geometry obtained by applying the second conformal map $H(w)$.

Before detailing the conformal transformations used, the different coordinate systems need to be defined. The initial geometry is described in the $(O_{x,y}, x, y)$ coordinate system. The first map transforms this coordinate system into $(O_{u,v}, u, v)$, while the second transformation gives the final coordinate system $(O_{p,q}, p, q)$.

The first conformal mapping transformation G is given by

$$G(z) = w = \frac{(R_{cnt,0} - \epsilon)\epsilon}{2R_{cnt,0} - \epsilon} + \frac{i\epsilon^2}{z - 2i\epsilon} \quad (3.2)$$

where $z = x + iy$ and $w = u + iv$, $z, w \in \mathbb{C}$ and $x, y, u, v \in \mathbb{R}$. Applying G to the initial geometry (Fig. 3.1) yields the geometry shown in Fig. 3.2 a). The original circle $C_{cnt,0}$ (radius: $R_{cnt,0}$, center: $O_{x,y}$) is mapped to a new circle $C_{cnt,1}$ (radius: $R_{cnt,1}$, center: $O_{u,v}$) while the straight line is transformed to a circle $C_{gra,1}$ (radius: $R_{gra,1}$, center: $A_{u,v}$). The coordinates of the point $A_{u,v}$ are given by

$$u_{A_{u,v}} = \frac{(2R_{cnt,0} - 3\epsilon)\epsilon}{4(2R_{cnt,0} - \epsilon)}, \quad v_{A_{u,v}} = 0. \quad (3.3)$$

The expressions for the radii read

$$R_{cnt,1} = \frac{R_{cnt,0}\epsilon}{|\epsilon - 2R_{cnt,0}|}, \quad R_{gra,1} = \epsilon/4. \quad (3.4)$$

The expressions u_1 and u_2 are defined for later use

$$u_1 = u_{A_{u,v}} - R_{gra,1}, \quad u_2 = u_{A_{u,v}} + R_{gra,1}. \quad (3.5)$$

For the second conformal mapping transformation H , a Moebius transformation was applied in order to map the circles previously obtained by using G into two concentric circles centered on $O_{p,q}$. The expression of $H(w)$ is given by

$$H(w) = t = \frac{w - ab}{aw - b} \quad (3.6)$$

3. ANALYTICAL CALCULATIONS

with $t = p + iq$, $t \in \mathbb{C}$, $p, q \in \mathbb{R}$ and a and b defined by

$$a = \frac{R_{cnt,1}^2 + u_1 u_2 + \sqrt{(R_{cnt,1}^2 - u_1^2)(R_{cnt,1}^2 - u_2^2)}}{R_{cnt,1}(u_1^2 + u_2^2)} \quad (3.7)$$

$$b = R_{cnt,1}. \quad (3.8)$$

This time, the circle $C_{cnt,1}$ is mapped under the transformation H into the circle $C_{cnt,2}$ (radius: $R_{cnt,2}$) and the circle $C_{gra,1}$ is transformed into the circle $C_{gra,2}$ (radius: $R_{gra,2}$). Both circles $C_{cnt,2}$ and $C_{gra,2}$ are centered at $O_{p,q}$ as shown in Fig. 3.2 b).

$R_{cnt,2}$ has a simple value since it has been mapped to the unit circle

$$R_{cnt,2} = 1 \quad (3.9)$$

while the expression for $R_{gra,2}$ is the following

$$R_{gra,2} = \frac{R_{cnt,1}^2 - u_1 u_2 + \sqrt{(R_{cnt,1}^2 - u_1^2)(R_{cnt,1}^2 - u_2^2)}}{R_{cnt,1}(u_1^2 - u_2^2)}. \quad (3.10)$$

By applying successively the transformations G and H , the expression of $p(x, y)$ and $q(x, y)$ can be inferred since

$$\Re(G(z)) = \Re(w) = u(x, y) \quad \Im(G(z)) = \Im(w) = v(x, y) \quad (3.11)$$

and

$$\Re(H(w)) = \Re(t) = p(u, v) \quad \Im(H(w)) = \Im(t) = q(u, v) \quad (3.12)$$

where \Re stands for the real part and \Im for the imaginary part.

The final geometry (Fig. 3.2 b)) matches the one of a capacitor made of two infinitely long and concentric cylindrical shells. The inner cylinder (radius: $R_{cnt,2}$) is at the potential V_{cnt} and the outer cylinder (radius: $R_{gra,2}$) is at V_{gra} . The solution of Laplace's equation is easy for this simple geometry and yields the following potential between the two cylinder capacitor:

$$V(p, q) = V_{cnt} + \frac{\Delta V}{c} \left(\ln(\sqrt{p^2 + q^2}) - \ln(R_{cnt,2}) \right) \quad (3.13)$$

where $\Delta V = V_{gra} - V_{cnt}$ and $c = \ln\left(\frac{R_{gra,2}}{R_{cnt,2}}\right)$.

Using the expression of $p(x, y)$ and $q(x, y)$ in Eq. 3.13 provides the potential expression for the initial geometry $V(x, y)$.

3.3 Potential and charge density

Potential map

When holding both structures at a different potential, the induced potential is expected to exhibit a significant drop in the area between CNT and graphene which will be referred to

from now on as the junction region. Away from the junction region, the potential should not differ from that of the graphene sheet in nearby regions and it should go to zero for regions far away from both structures. In order to illustrate this fact, a map of the electric potential is represented in Fig. 3.3 for a CNT (5,5) with $V_{cnt} = 10$ V and $V_{gra} = 1$ V.

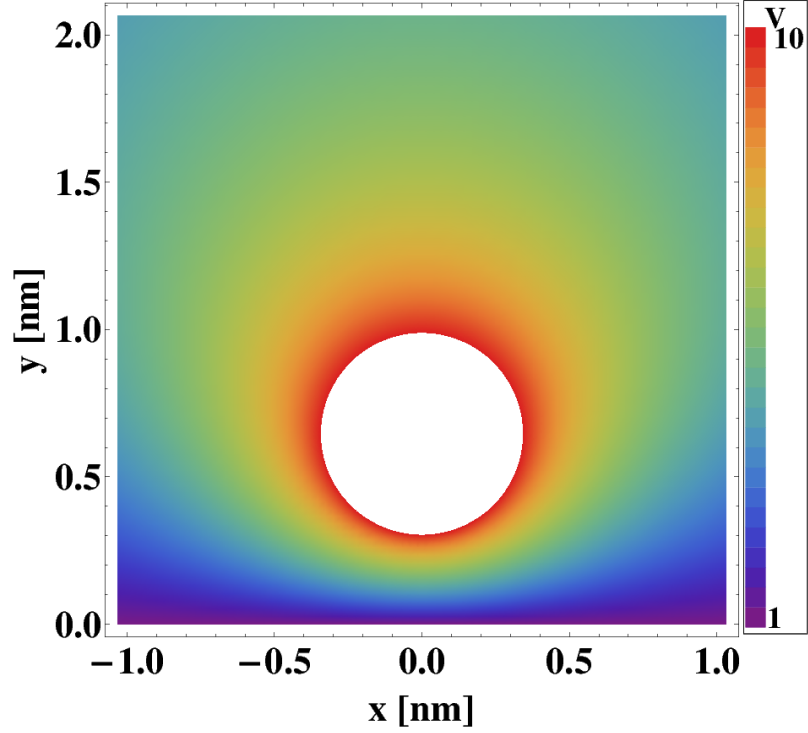


Figure 3.3: Map of the electric potential for a CNT (5,5). The tube is represented as a white circle. The potential of the nanotube is $V_{cnt} = 10$ V, the graphene is maintained at $V_{gra} = 1$ V

Charge density

Since the considered system is a 2D system, the linear charge density $\lambda(x)$ for the graphene sheet is given in the $(O_{x,y}, x, y)$ coordinate system by

$$\frac{\partial V}{\partial x}(x, y) = -\frac{\lambda(x)}{\epsilon_0}. \quad (3.14)$$

Since the effective potential difference at the junction is hard to determine, a large range for the potential difference from $\Delta V = 9 \cdot 10^{-3}$ V to 9 V has been used for the calculations. Nevertheless, the influence of the potential difference on the results has proven to be easy to handle, because it could be worked as a proportionality coefficient. Indeed, the modulus of the maximum charge density represented in the Fig. 3.4 inset displays a clear linear behaviour with the potential difference. The linear dependence between the potential difference and the charge density has been confirmed by studying the normalised charge density to the potential difference, as all the curves collapse into a single curve.

3. ANALYTICAL CALCULATIONS

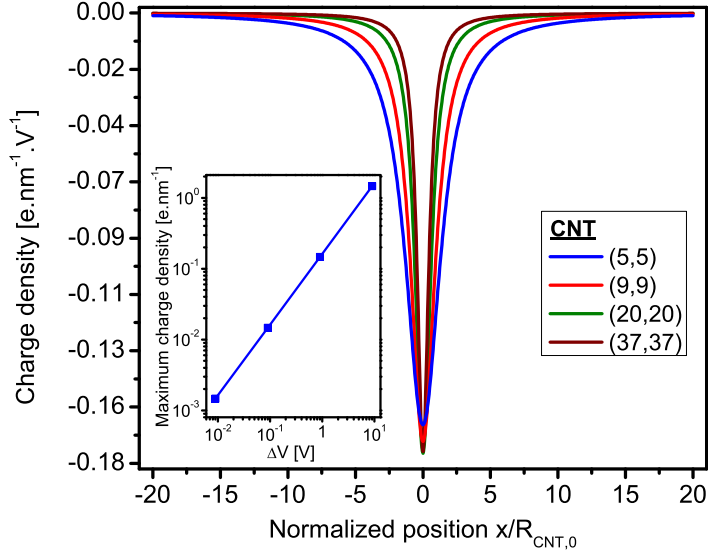


Figure 3.4: Charge density for the CNT (5,5), (9,9), (20,20) and (37,37) normalised to the potential difference ΔV . The distance has been normalised to the radius of the tubes. Inset: Modulus of the maximal charge density versus the potential difference ΔV for a CNT (5,5).

Fig. 3.4 shows the charge density $\lambda(x)$ normalised to the potential difference ΔV for CNT (5,5), (9,9), (20,20) and (37,37). The charge density profile exhibits a sharp peak in the junction region and reaches its maximum at the closest point to the CNT. Such charge accumulation does only occur in a region of the graphene sheet close to the CNT, as the charge density profile tends quickly toward to the neutrality elsewhere. The influence of the CNT on the charge distribution in the graphene sheet is thus spatially limited to a small portion of it, around the junction region.

The maximum charge accumulation is $-1.67 \times 10^{-1} \text{ e.nm}^{-1}.\text{V}^{-1}$ for the CNT (5,5) while for larger radius CNT the maximum is $-1.74 \times 10^{-1} \text{ e.nm}^{-1}.\text{V}^{-1}$, indicating that the the type of CNT considered does not play a significant role on the maximum of accumulated charge.

The simple 2D electrostatic gives a glimpse of the charge redistribution taking place at the interface between a CNT and a graphene sheet. The charge distribution in the graphene sheet is not affected on a large scale by the coupling with the CNT. This observation will be made clear and supplemented in the next section using a model that provides better accuracy, down to the atom scale.

4

Numerical calculations

The analytical calculations have shown that the influence of the CNT on the graphene charge distribution is confined to regions around the CNT. However, the analytical calculations did not take into account the atomic structure. A 3D atomic model also based on classical electrostatics, coined as "charge-dipole" model, has been used to overcome such limitations. It leads to obtain a more precise picture of the charge distribution around the CNT. In particular, the influence of CNT termination or the shape of the graphene sheet edges can be addressed with such model.

First the developments that led to the charge-dipole model are presented in Sec. 4.1 followed by a presentation of the model (Sec. 4.2). Although the charge-dipole model is an atomic model, it is not very sensitive to changes in the structure caused by geometry optimisation. It yields results with good accuracy for unrelaxed structures, thus providing an important computational time gain. Under this assumption, the geometry of the junction used for the calculations is described in Sec.4.4. To decrease the computational time, the scaling properties of the model are analysed in Sec. 4.5. The optimal length for the graphene sheet to be used for the calculations is determined. The influence length is defined and will be used further to characterise the effect of the CNT on the charge redistribution in the graphene sheet. After having determined that the model scales proportionally with the potential difference (Sec. 4.6), the results obtained by the charge-dipole model are presented in the last part of the chapter. For both structures, the CNT and the graphene sheet, the charge distribution is presented and analysed as well as the influence of structural parameters such as the termination type for the CNT and the shape of the graphene edge (Sec. 4.7 and Sec. 4.8).

4.1 Development of the charge-dipole model

The main idea conveyed by the "charge-dipole" model is to consider that to each atom i can be associated a net charge q_i and a dipole moment \mathbf{p}_i . The charge-dipole model is more accurate than the 2D classical electrostatic model discussed in Sec. 3, since it takes into account not only the charges but also the dipoles and yields an atomic description of the system. The electronic configuration of the sp^2 -hybridised carbon is also well reflected. The net charges account for the displacement of the mobile π -electrons while the dipoles

4. NUMERICAL CALCULATIONS

account for the tightly bound σ -electrons. For a given system, the pair of values $\{q_i, \mathbf{p}_i\}$ associated with each atom are determined by minimizing the total electrostatic energy E_{tot} .

The model has been first suggested by Olson and Sundberg (74) as an improvement and extension to previous works on molecular polarisability. Before the prevalent model used for polarisation calculations had been the "atom dipole interaction" model which took into account the dipoles and not the net charges, as described in a reference study published by Applequist *et al.* (75).

The idea of associating with each atom of a molecule a net charge and a dipole to determine electronic properties has then been successfully applied by Applequist *et al.* to compute the polarizability of several fullerenes (76). Stern implemented the charge-dipole model to render the electrostatic interactions as part of a molecular mechanics force field (77).

The charge-dipole model has been presented in its current development by Mayer in 2005 to compute the polarization of metallic CNT (78). In the same year, he found a satisfying renormalisation to avoid the divergence arising when considering the charge distribution around the atom as point charge (79). Further work published in 2007 improved the accuracy of the model (80). Further results on fullerenes, nanotubes and hydrocarbons molecules polarisation were carried using the framework of the charge-dipole model (81, 82, 83). Additionally to polarisation calculations, the charge-dipole model could render in a satisfying way the electrostatic field induced deformations of CNT cantilevers (84) and charge rearrangement in charged CNT (85).

In a recent work, Wang and Scharstein applied the model to a graphene sheet held at a defined potential in order to compute the charge distribution (86). They compared the results obtained with the charge-dipole model to the charge distribution obtained by a classical electrostatic analytical model. The charge-dipole model results matches with the analytical conclusions, showing the expected charge enhancement effects on the edge of the graphene and allows to draw conclusions on an atomic scale.

4.2 Presentation of the charge-dipole model

The charge-dipole model is described in the following part as presented and parametrized by Mayer in 2005 and extended in 2007 (79, 80). As already mentioned above, each atom i is associated with a net charge q_i and with a dipole moment \mathbf{p}_i .

Total electrostatic energy

The total electrostatic energy for a N -atom system and its associated charge-dipole values $\{q_i, \mathbf{p}_i\}$ reads

$$\begin{aligned}
 E_{tot} = & \frac{1}{2} \sum_{\substack{i,j=1 \\ i \neq j}}^N q_i T_{q-q}^{i,j} q_j - \sum_{\substack{i,j=1 \\ i \neq j}}^N q_i \mathbf{T}_{q-p}^{i,j} \mathbf{p}_j - \frac{1}{2} \sum_{\substack{i,j=1 \\ i \neq j}}^N \mathbf{p}_i \mathbf{T}_{p-p}^{i,j} \mathbf{p}_j \\
 & + \frac{1}{2} \sum_{i=1}^N q_i T_{q-q}^{i,i} q_i - \sum_{i=1}^N q_i \mathbf{T}_{q-p}^{i,i} \mathbf{p}_i - \frac{1}{2} \sum_{i=1}^N \mathbf{p}_i \mathbf{T}_{p-p}^{i,i} \mathbf{p}_i \\
 & + \sum_{i=1}^N q_i (\chi_i + V_{i,ext}) - \sum_{i=1}^N \mathbf{p}_i \cdot \mathbf{E}_{i,ext}.
 \end{aligned} \tag{4.1}$$

The interaction between the additional charges carried by the atom i and the core of the atom is described for by the affinity χ_i . External parameters such as the set potential $V_{i,ext}$ and the applied electrostatic field $\mathbf{E}_{i,ext}$ are also taken into account in the expression of the electrostatic energy.

The first three terms in E_{tot} are the mutual interaction terms between atoms, the next three terms contain the self-energy terms whereas the two last terms are the single-atom interaction terms. The terms T_{q-q} , \mathbf{T}_{q-p} , \mathbf{T}_{p-p} contain respectively the charge-charge, charge-dipole, dipole-dipole interactions in vacuum. These terms are in fact tensors whose dimensionality ranges from zero for the charge-charge term to two for the dipole-dipole term.

The charge-charge interaction term is given by

$$\frac{1}{2} \sum_{\substack{i,j=1 \\ i \neq j}}^N q_i T_{q-q}^{i,j} q_j \tag{4.2}$$

where $T_{q-q}^{i,j}$ stands for the charge-charge interaction tensor in vacuum. If $r_{i,j}$ is the distance between the atom i and the atom j , and \mathbf{r}_i the coordinate of the atom i , the regular expression for $T_{q-q}^{i,j}$ is then :

$$T_{q-q}^{i,j} = \frac{1}{4\pi\epsilon_0} \frac{1}{r_{i,j}} \tag{4.3}$$

The charge-dipole interaction term has the following expression

$$- \sum_{\substack{i,j=1 \\ i \neq j}}^N q_i \mathbf{T}_{q-p}^{i,j} \mathbf{p}_j \tag{4.4}$$

where $\mathbf{T}_{q-p}^{i,j}$ is the charge-dipole interaction tensor in the vacuum. The regular expression for $\mathbf{T}_{q-p}^{i,j}$ can be derived from $T_{q-q}^{i,j}$ by:

$$\mathbf{T}_{q-p}^{i,j} = -\nabla_{\mathbf{r}_i} T_{q-q}^{i,j} \tag{4.5}$$

4. NUMERICAL CALCULATIONS

The dipole-dipole interaction term has the following expression

$$-\frac{1}{2} \sum_{\substack{i,j=1 \\ i \neq j}}^N \mathbf{p}_i \mathbf{T}_{p-p}^{i,j} \mathbf{p}_j \quad (4.6)$$

where $\mathbf{T}_{p-p}^{i,j}$ is the dipole-dipole interaction tensor in vacuum. As for the charge-dipole interaction tensor, the regular expression for $\mathbf{T}_{p-p}^{i,j}$ can be derived from the previous terms by applying the operator ∇ :

$$\mathbf{T}_{p-p}^{i,j} = -\nabla_{\mathbf{r}_j} \otimes \nabla_{\mathbf{r}_i} T_{q-q}^{i,j} \quad (4.7)$$

Regularization of the net charge density

When a point charge distribution is considered, the charge-charge, charge-dipole and dipole-dipole terms do diverge when $r_{i,j} \rightarrow 0$. A regularization of the net charge distribution has been introduced to avoid such divergence. To be able to define the terms $T_{q-q}^{i,i}$, $\mathbf{T}_{q-p}^{i,i}$, $\mathbf{T}_{p-p}^{i,i}$, the net charge density for each atom has been regularized by a Gaussian distribution centered on the atom. The atom i carrying a net charge q_i has its charge distribution given by

$$\rho_i(\mathbf{r}) = \frac{q_i}{\pi^{3/2} R^3} \exp\left(-\frac{|\mathbf{r} - \mathbf{r}_i|^2}{R^2}\right) \quad (4.8)$$

where R is the width of the Gaussian distribution. Using the Eq. 4.8 in the expressions for the interaction tensors terms leads then to the following expressions

$$T_{q-q}^{i,j} = \frac{1}{4\pi\epsilon_0} \frac{\text{erf}\left(\frac{r_{i,j}}{\sqrt{2}R}\right)}{r_{i,j}} \quad (4.9)$$

$$\mathbf{T}_{q-p}^{i,j} = \frac{1}{4\pi\epsilon_0} \frac{\mathbf{r}_{i,j}}{r_{i,j}^3} \left[\text{erf}\left(\frac{r_{i,j}}{\sqrt{2}R}\right) - \sqrt{\frac{2}{\pi}} \frac{r_{i,j}}{R} \exp(-r_{i,j}^2/2R^2) \right] \quad (4.10)$$

$$\begin{aligned} \mathbf{T}_{p-p}^{i,j} = & \frac{1}{4\pi\epsilon_0} \frac{\mathbf{3}r_{i,j} \otimes \mathbf{r}_{i,j} - r_{i,j}^2 \mathbf{Id}_3}{r_{i,j}^5} \left\{ \right. \\ & \left[\text{erf}\left(\frac{r_{i,j}}{\sqrt{2}R}\right) - \sqrt{\frac{2}{\pi}} \frac{r_{i,j}}{R} \exp(-r_{i,j}^2/2R^2) \right] - \\ & \left. \sqrt{\frac{2}{\pi}} \frac{1}{R^3} \frac{\mathbf{r}_{i,j} \otimes \mathbf{r}_{i,j}}{r_{i,j}^2} \exp(-r_{i,j}^2/2R^2) \right\} \end{aligned} \quad (4.11)$$

where \mathbf{Id}_3 is the size 3 identity matrix and erf is the Gauss error function

$$\text{erf}(x) = \frac{2}{\sqrt{\pi}} \int_0^x \exp(-t^2) dt. \quad (4.12)$$

The self-energy terms are obtained as limiting case in the expressions of the interaction

tensors 4.9, 4.10, 4.11 when $r_{i,j} \rightarrow 0$:

$$T_{q-q}^{i,i} = \frac{1}{4\pi\epsilon_0} \frac{\sqrt{2}}{\sqrt{\pi}R} \quad (4.13)$$

$$\mathbf{T}_{p-q}^{i,i} = 0 \quad (4.14)$$

$$\mathbf{T}_{p-p}^{i,i} = -\frac{1}{4\pi\epsilon_0} \frac{\sqrt{2}}{3\sqrt{\pi}R^3} \mathbf{Id}_3. \quad (4.15)$$

As pointed out in (80), the dipole-dipole self-interaction $\mathbf{T}_{p-p}^{i,i}$ term is equal to α_{iso}^{-1} which is the polarisability of the carbon atoms in sp^2 carbon structures. Thus assuming an isotropic polarisability, the following relation can be used to link the parameter R (i.e., the width of the Gaussian distribution) and the polarisability

$$\frac{\alpha_{iso}}{4\pi\epsilon_0} = 3\sqrt{\frac{\pi}{2}} R^3. \quad (4.16)$$

The parameter R has been then determined using experimental data to reproduce the mean polarisability of fullerenes and lateral polarisability of CNT (78). R was set to 0.06862 nm for the calculation, corresponding to a polarisability of $\frac{\alpha_{iso}}{4\pi\epsilon_0} = 0.12149001 \text{ nm}$ and was used in all the recent work cited in Sec 4.1.

Minimization of the energy

For a system of N -atoms, the $\{q_i, \mathbf{p}_i\}$ for each atom are determined by minimizing the total electrostatic energy E_{tot} given by Eq.4.1. The minimization is carried out by requiring that for each atom i

$$\frac{\partial E_{tot}}{\partial q_i} = 0 \quad \text{and} \quad \frac{\partial E_{tot}}{\partial \mathbf{p}_i} = 0$$

This leads to solve a $4 \times N$ linear equations system.

If the sum of the net charge is required to be equal to a specific value Q_{tot} , an additional equation is added to the linear equation system determined previously. The minimization of the expression $E_{tot} - \lambda(\sum_i q_i - Q_{tot})$ with respect to the variable λ yields the additional equation

$$\frac{\partial E_{tot}}{\partial \lambda} = 0$$

The implementation of the charge-dipole model has been done using the C++ programming language. The resolution of the linear equation system was performed with the routine DGESV called by the C++ code. This routine is part of the LAPACK package (87) written in Fortran. Structures with up to about 10.000 atoms could be solved using the random access memory (RAM) resources of the Opus Cluster from the Steinbuch Centre for Computing (SCC). The size of the systems handled with the charge-dipole model is therefore larger than with ab-initio methods or even semi-empirical methods.

4.3 Code validation

The C++ code has been validated by reproducing results from the literature. First, the charge distribution in a graphene sheet has been computed as it has been reported by Wang and Scharstein *et al.* (86). They confirmed the following classical electrostatic result: for a rectangular graphene sheet held at a certain electric potential with an amount of external charges, the electric charges tend to accumulate on the edges and on the corners. Silvestrov *et al.* (88) had already studied such charge accumulation effect but using analytical electrostatic model. Wang and Scharstein thus used a numerical charge-dipole based model to compute the charge distribution in free-standing graphene, without any substrate consideration. The graphene sheet was relaxed by using adaptive intermolecular reactive bond order potential functions (AIREBO). The same calculations but without any relaxation of the geometry have been carried out using the C++ code based on the following procedure.

The $8 \text{ nm} \times 5 \text{ nm}$ graphene sheet has been generated with the parameters described later in Sec. 4.4. The graphene flake was held at a potential of $V_{gra} = 1 \text{ V}$ and the reference was taken at infinite distance. An amount of additional charges is introduced in the graphene sheet.

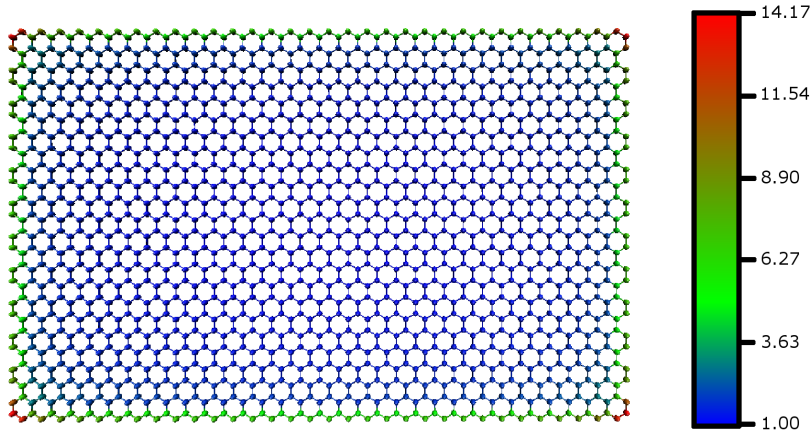


Figure 4.1: Density of net charge for a graphene flake. A color scale is used to represent the charge density for each atom. Red stands for a high charge density, blue for a lower one. The density has been normalised to that in the middle of the graphene sheet: $q_0 = 8.1 \cdot 10^{-4} e$ per atom.

Fig. 4.1 illustrates the charge distribution for the unrelaxed graphene sheet. The charge has been normalised to that in the middle of the graphene sheet. It shows as expected charge enhancement at the edges and corners. Additionally, the value of the net charge reaches in the corners its maximum value (i.e., about 14 times the charge at the centre of the flake). The range of the normalised charge density is thus in perfect agreement with the values obtained by Wang and Scharstein (86). The results for the non-relaxed structure matches perfectly the results for the relaxed graphene.

As a second test, the net charge distribution has been computed for an uncapped CNT (5,5) made of 110 atoms having an excess of $Q = 20 e$ charges. DFT as well as electrostatic moment calculations have been reported for the CNT (5,5) system additionally to the charge-dipole method (89, 90, 91). The expected U-shape curve was obtained for the charge distribution (Fig . 4.2). First, the charge-dipole model calculations exhibit little variation between unrelaxed/relaxed structures. The value of the net charge differs slightly only for the end atoms, which undergo the most important positional change during the relaxation process. When compared to DFT and moment method results, the charge-dipole model results show a lower charge value for the end atoms for both unrelaxed/relaxed structures. Indeed, the normalised charge given by the charge-dipole is around 1.8 to 2 whereas for the DFT and moment method it is around 2.5-2.7. In the center part thus the results obtained by all three methods show good agreement, the DFT calculations yields a slightly lower value but shows some oscillation that could be related to numerical instabilities.

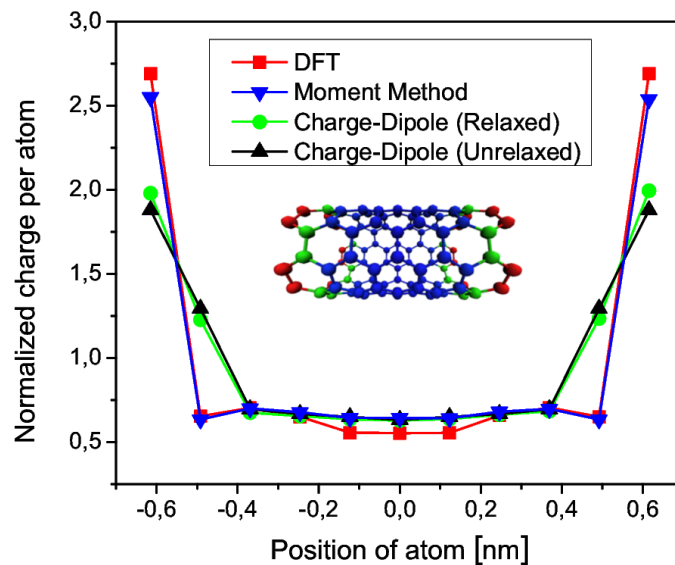


Figure 4.2: Normalised net charge along the (5,5) CNT axis with respect to the average net charge per atom. The results for the unrelaxed/relaxed CNT using the charge-dipole model are represented as well as results of DFT calculations from (90) and results of using an electrostatic moment method (91). Inset: Net charge per atom depicted using a color scale. The blue colour indicates a low net charge while the green denotes a significant amount of net charge and the red colour stands for strong accumulation of charge.

Beside the validation test of the C++ code, reproducing already published work leads to conclude that for the charge-dipole model the benefit of geometry optimisation is not significant. Indeed, unrelaxed and relaxed structures show almost the same charge distribution. The charge-dipole model is not sensitive to changes in the atoms position of the order of magnitude of that introduced by the relaxation processes. Thus, for the rest of

4. NUMERICAL CALCULATIONS

the work, this costly computational step will not be performed in order to speed up the calculations.

4.4 Geometry

Since the charge-dipole model is a 3D model that takes into account the atomic structure, the geometry used as input for the calculations differs from that used for the analytical calculations and therefore it needs to be redefined here. The CNT-graphene junction was modeled by a rectangular sheet of graphene and a carbon nanotube placed on top of the graphene sheet. As for the 2D analytical calculations, the output of the semi-empirical structural calculations from Sec. 2.3.4 is used to determine the equilibrium distance ϵ between graphene and CNT. Only in Sec. 5.2, the distance ϵ has been set to different values. The carbon-carbon in-plane bond was taken from the literature and corresponds to $a = 0.142$ nm. The stacking of the atoms is A-B, meaning that for the CNT, its closest atoms to the graphene flake is located at the center of a hexagonal cell. The coordinate system used for the calculations as well as the different structural parameters are depicted in Fig. 4.3.

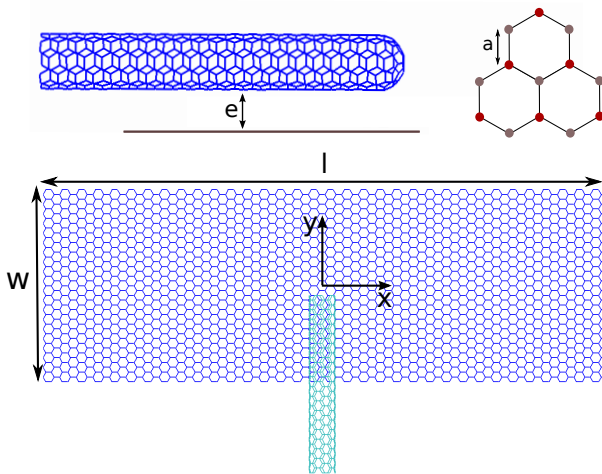


Figure 4.3: Parameters and coordinate system used for the calculations

containing $N_{cnt} = 380$ atoms. The junction length (i.e., the length of the part of the CNT lying on top of the graphene flake) is approximatively 2.25 nm, the rest of the CNT is suspended away from the sheet.

The choice of the CNT (5,5) makes sense when it comes to cap the nanotube. Indeed capping the CNT (5,5) is easily done with a C_{30} hemisphere made by halving of a C_{60} molecule ($N_{cnt} = 420$) and attaching it to the CNT end lying on top the graphene sheet. The free standing end was left uncapped. To study the influence of the radius on the results, CNT (n,n) with n up to 50 (i.e., up to radius about 3.4 nm) were generated by repeating enough unit cells in the y direction assuring a junction length of about 2.25 nm.

The width of the graphene sheet was fixed through all the calculations to $w \sim 5.00$ nm while the length varied from $l \sim 5.00$ nm to 50.00 nm. The number of atoms in the graphene sheet ranged consequently from $N_{gra} = 984$ to $N_{gra} = 9512$.

Although the charge-dipole model does not take into account the band structure, for the coherence of the study, only metallic CNT have been used to form the junction. Most part of the analysis has been carried with a CNT (5,5) generated by repeating 19 elementary cells in the y direction, thus having a non-capped length of about 4.60 nm and

4.5 Charge profile and scaling of the model

The charge-dipole model yields a picture of the charge reorganisation that occurs when CNT and graphene are brought together and held at different potentials, forming a CNT-graphene junction. The charge-dipole model is used to determine the spatial extent of the charge redistribution in the graphene sheet. An obvious limitation of the charge-dipole model and, in general, of electrostatic-based models is that they assume that a sufficient number of states are available for the electrons in both structures. They do not consider any band structure effects. For graphene, this implies that in the vicinity of the Dirac point the results have to be considered with caution.

As mentioned above, the calculations were made using a CNT (5,5). The first task was to determine how the net charge redistribution scales with the length l of the graphene flake. Knowing the optimal length for the graphene flake helps to reduce the computational cost of the simulations but also ensure the accuracy of the results. At the same time, the initial calculations were used for a preliminary analysis of the charge distribution. For this purpose, several lengths ranging from $l \sim 5.00$ nm to ~ 50.00 nm have been used to run the simulations. The net charge profile was analysed in the graphene along the length of the sheet near the junction region as well as far from the CNT, following the line drawn in the inset of Fig. 4.4. The calculations were carried for a potential difference $\Delta V = V_{cnt} - V_{gra} = 9$ V, the graphene was held at $V_{gra} = 1$ V while the CNT at $V_{cnt} = 10$ V. The neutrality of the system is ensured by requiring the total charge to be zero. This condition and the potential difference ΔV fix the amount of charges in each structure.

Charge profile

As depicted in Fig. 4.4, the charge profile exhibits a sharp peak close to the position of the CNT on an otherwise flat part of the profile. The charge distribution profile for the atoms in the graphene flake experiences considerable variation close to the junction region. The closest the graphene atoms are located to the CNT, the strongest the charge accumulation. On the other hand, the further the graphene atoms from the CNT, the weaker the charge accumulation. For atoms located a few nm away from the CNT ($x \geq 2 - 3$ nm), the charge profile flattens when the influence of the CNT becomes less prevalent, meaning that the extension of the charge redistribution is limited. The atoms located on the row forming the edges of the graphene sheet have significantly higher charge values as displayed by charge profile kink for the outermost point. This is due to electrostatic edge effects: the charges tend to accumulate at the edges of the structure.

Scaling of the model

No significant change in the charge profile around the junction region is observed when changing the length of the graphene sheet as illustrated in Fig. 4.4. The accumulation peak in the charge profile has the same shape through all calculations. For a length of $l \sim 5.00$ nm, the maximum is about $-10.97 \times 10^{-2} e$ per atom while for $l \sim 50.00$ nm

4. NUMERICAL CALCULATIONS

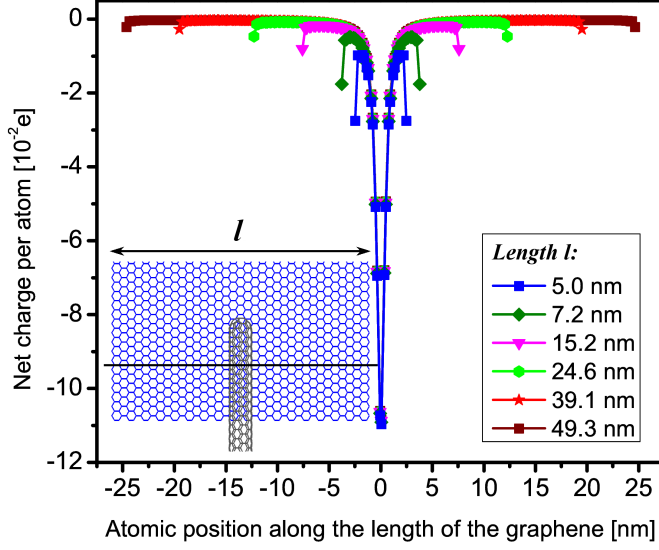


Figure 4.4: Charge per atom in the junction region along the length of the graphene flake. Different lengths for the graphene flake have been used.

the values is about $-10.85 \times 10^{-2} e$ per atom. These values correspond to the charge carried by the atom closest to the CNT. As for the edge effects, characterised by charge accumulation at the end of the graphene sheet, narrower graphene flakes exhibit stronger effects up to $-2.76 \times 10^{-2} e$ per atom for a $l \sim 5.00$ nm length. With increasing length, the edge effects become less significant. An additional effect of the scaling is that for lengths larger than ~ 15 nm, the additional charge of atoms located away from the CNT is almost zero. The influence of the CNT is confined to a few atomic rows near the junction region. For shorter sheets, the influence of the CNT and the edge effects can not be analysed independently since the charge value stays well above neutrality through all the sheet. For the rest of the study, a value of $l \sim 25$ nm was chosen for the length of the graphene sheet assuring on one hand negligible edge effects and on the other hand allowing to define clearly the CNT influence zone.

Influence length $l_{5\%max}$

For a more accurate analysis of the extension of the charge redistribution in the graphene sheet, the value $|q|_{5\%max}$ has been defined. It corresponds to 5% of the maximal absolute value for the net charge and it is located in the part where the charge profile starts to flatten. Thus, the length on the graphene sheet $l_{5\%max}$ where the charge profile reaches $|q|_{5\%max}$ is a good indicator of how far the CNT affects the charge distribution in the graphene sheet. In Fig. 4.5, $l_{5\%max}$ is shown for different values of graphene sheet length. For small lengths, $l_{5\%max}$ is limited to the very few atomic rows near the junction because of the edge effects and it cannot give a reliable information over the extension of the CNT influence on the graphene. $l_{5\%max}$ increases with the length of the graphene sheet until it

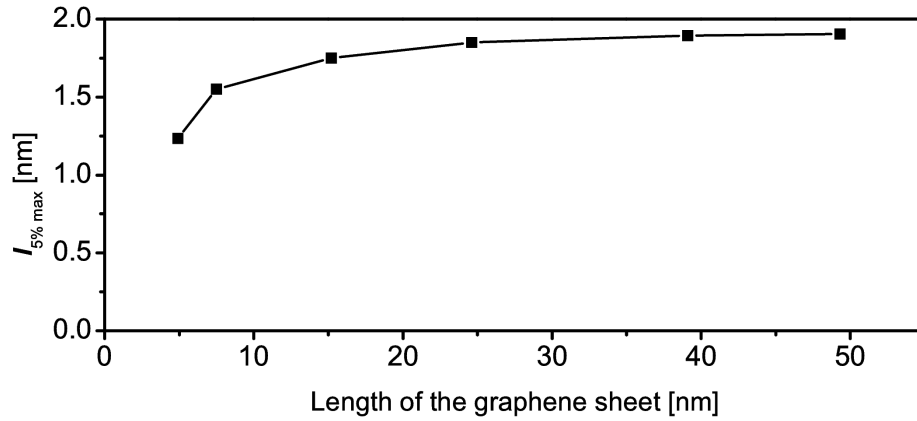


Figure 4.5: Length on the graphene sheet where the net charge corresponds to $|q|_{5\%max}$ for different graphene sheet widths.

reaches a limit value around 1.9 nm. This limit value defines the influence length of the CNT on the graphene.

4.6 Effects of the potential difference

The results inferred from the analytical calculations presented a linear behaviour with the potential difference $\Delta V = V_{cnt} - V_{gra}$. The charge distribution computed with the charge-dipole model scales proportionally with the potential difference as well. The shape of the charge profile in the graphene sheet and the length over which the carbon nanotube affects the charge in the graphene do not change with the potential difference.

This result was established comparing the maximum of net charge obtained and the charge profile for several values of ΔV . The left plot in Fig. 4.6 shows the charge profile for $\Delta V = 5V, 9V, 15V$ and $18V$. The charge profile exhibits the same shape for each potential difference.

As depicted in the inset in the right part of Fig. 4.6, the values for the maximal depletion ranges from $-6.0 \times 10^{-2} e$ for $\Delta V = V_{cnt} - V_{gra} = 5V$ to $-22.9 \times 10^{-2} e$ for $\Delta V = 18V$. They present a linear behaviour with respect to ΔV . The same observations have been made for the mean value of the charge in the graphene sheet. The charge profile seems thus to scale proportionally with the potential difference ΔV . This trend is confirmed when analysing the charge profiles normalised to the potential difference ΔV as depicted in the right part of Fig. 4.6. Consequently, all charge values will be from now on normalized to the potential difference.

4.7 Charge distribution in the graphene sheet and in the CNT

The charge distribution in the tube and in the graphene sheet is addressed in this section. In addition, the modification in the charge distribution have been investigated when

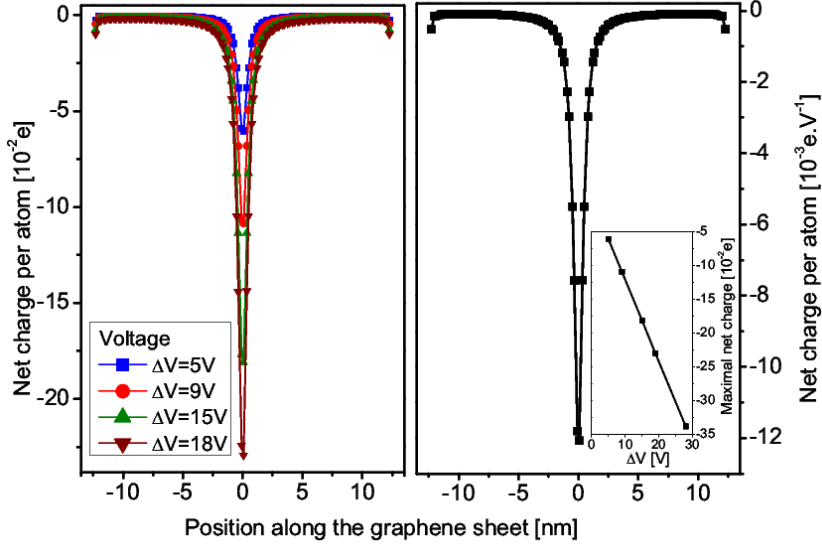


Figure 4.6: Left: Net charge profile along the length of the graphene sheet in the middle of the junction region for $\Delta V = 5V, 9V, 15V, 18V$. Right: Net charge profile along the length of the graphene sheet in the middle of the junction region normalised to the potential difference ΔV . Inset: Maximum charge depletion for several potential differences ΔV .

changing the type of CNT termination. The comparison was carried between CNT with open ends (i.e., uncapped CNT) and CNT with closed ends (i.e: capped CNT).

First the charge distribution for a junction with an uncapped CNT (5,5) has been analysed. A view of the charge redistribution near the junction region is depicted in Fig. 4.7. As expected, for the atoms located close to the junction the charge value significantly differs from the average charge, denoting a charge accumulation/depletion in this region. More precisely, the strongest charge variations are found at the end of the CNT that lies on top of the graphene and in the graphene parts lying under the CNT.

Charge distribution in the open-ended CNT

The charge distribution in the top- and bottom-rows (see inset Fig.4.8) has been addressed. The atoms of the CNT along the top row experience a significant change in their net charge only at the ends. Indeed, as inferred from Fig. 4.8, the net charge ranges from 0.32 to $0.40 \times 10^{-2} e$ per atom and per Volt for central atoms. The end atoms at each end of the CNT, experience a higher charge variation due to edge effects.

This observation contrasts with the behaviour displayed by the bottom atoms of the CNT. The charge profile exhibits two clear parts: a weakly charged part outside the junction region and a highly charged part in the junction region with in between a transition region. The bottom-row atoms show a charge increase in the junction part since they experience a significant influence of the graphene flake. Their charge does not vary significantly and has values around $1.70 \times 10^{-2} e$ per atom and per Volt. Away from the junction part, except for the end atom, the influence of the graphene lessens therefore the

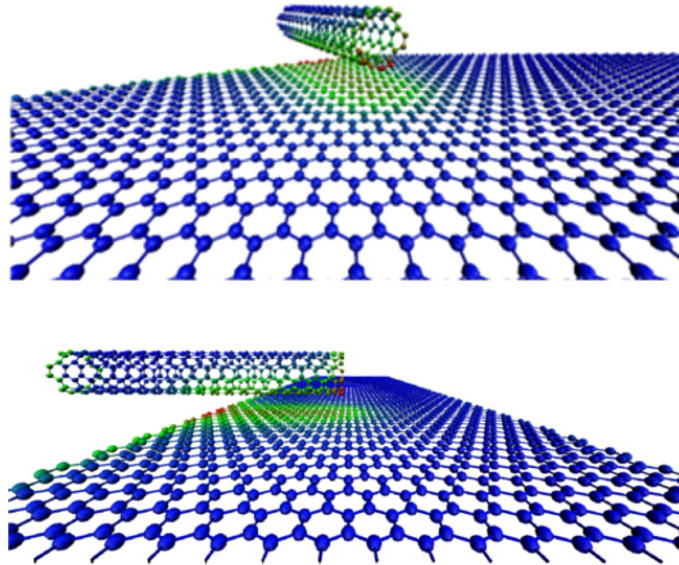


Figure 4.7: Net charge density for an uncapped metallic CNT (5,5)-graphene junction. The net charge has been normalised for the CNT as well as for the graphene to the average charge per atom for each structure. The color scale indicates the magnitude of the charge redistribution. The blue colour indicates a net charge close to the average while the green denotes a significant variation to the average and the red colour stands for a strong variation to the average.

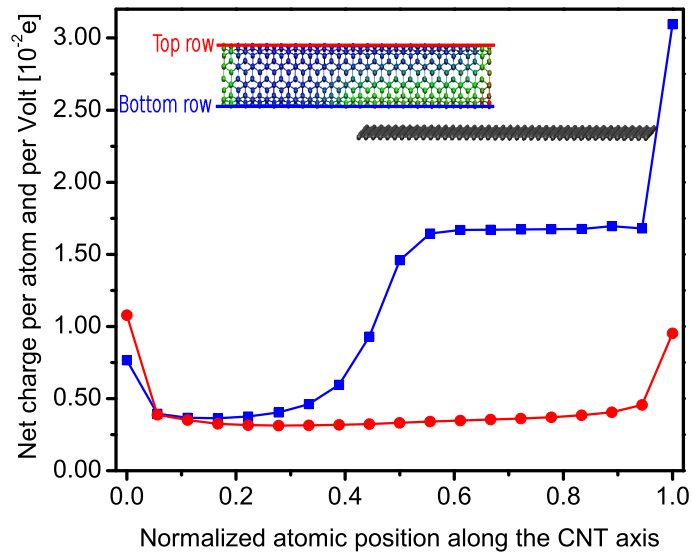


Figure 4.8: Net atomic charge density for an open-ended CNT (5,5) part of CNT-graphene junction normalised to the length of the CNT. The net charge profile has been represented for the top atomic row (red curve) and for the bottom atomic row (blue curve).

4. NUMERICAL CALCULATIONS

charge exhibits values close to the top rows atoms net charges. The charge profile for the central row did not show significantly difference with the top row. This implies that only the closest atom row to the graphene are affected by the charge redistribution.

For the CNT, the charge accumulation is then restricted to the closest rows of atoms to the graphene sheet. These atoms carry a charge about 4 to 5 times higher than the atoms away from the junction region or the atoms further away from the graphene sheet.

Charge distribution in the graphene

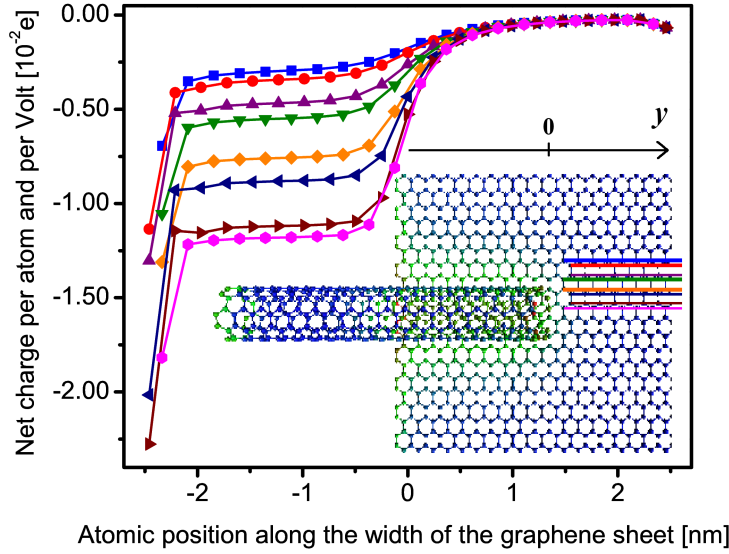


Figure 4.9: Charge density profile along the width of the graphene flake for different rows of atoms. The colours correspond to the different atomic rows with $x = cst$.

In the graphene sheet, the same trend as in the CNT is observed for the charge redistribution. The junction area exhibits a significant charge accumulation while regions located further away from the tube tend the charge neutrality. As already mentioned in Sec. 4.5, the significant charge redistribution takes place in the graphene only in a limited region around the tube. The influence length is about 1.90 nm in the perpendicular direction to the tube axis. The analysis of the net charge profile across the x and y directions in the graphene sheet makes evident the contrast between the low-charge and high-charge regions. This analysis substantiates the value of the influence length and leads to identify the characteristics of the high-charge region.

Apart from the edge atoms, the charge distribution is homogeneous in the junction region along the direction of the tube axis (i.e., along the width of the sheet). In contrast, the charge value tends quickly toward the neutrality for the atoms outside the junction region. Perpendicular to the tube axis (i.e: along the length of the sheet), as expected, the value of the net charge decreases with the distance to the axis of the CNT. These features are clearly illustrated by the representation along the width of the charge profile in the sheet

4.7 Charge distribution in the graphene sheet and in the CNT

in Fig. 4.9. In the junction region, for the row of atoms located closest to the tube axis, the net charge per atom varies from -1.11 to $-1.22 \times 10^{-2} e$ per atom and Volt (pink curve in Fig. 4.9), while for the row located close to the radius of the CNT (5,5), the net charge has already diminished significantly, ranging from -0.72 to $-0.81 \times 10^{-2} e$ per atom and Volt (the orange line in Fig.4.9). For a distance of approximately twice the CNT radius (blue curve in Fig. 4.9), the net charge value has dropped by more than a factor of three, being around $-0.35 \times 10^{-2} e$ per atom and Volt.

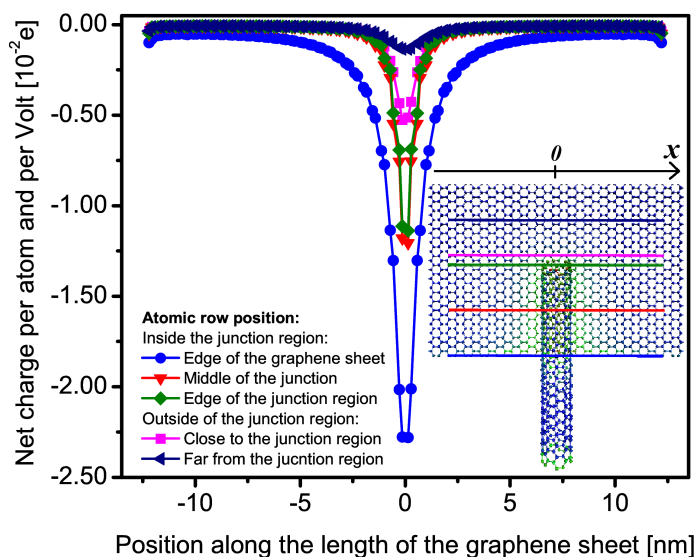


Figure 4.10: Charge profile along the length of the graphene flake for different rows of atoms. The colours displayed in the top figure correspond to the different atomic rows with $y = cst$.

The analysis of the charge profile along the length of the graphene sheet confirms the quick drop of the charge value with the increasing distance to the CNT axis and made evident the homogeneous distribution of the charge in the junction region. As seen in Fig. 4.10, the charge profile shows a strong variation for atoms close to the CNT, while it presents a steep drop a few atomic rows away from the CNT axis reaching a value close to charge neutrality. As already pointed out, the charge value does not show significant variation in the junction region along the length of the graphene. The charge profile in the middle of the junction region (red line in Fig. 4.10) and the profile at the end of the tube (green lines in Fig. 4.10) present no significant contrast. Moreover, the influence of the tube is clearly limited across the graphene not only in the width but also in the length. The rows of atoms that are not located under the tube (pink and dark blue lines in Fig. 4.10) contrast with the previous mentioned rows, since the magnitude of the peak in the charge profile decreases quickly with the distance from the tube. This results in a flatter charge profile and values close to neutrality.

Now focusing on the edge atoms, the charge enhancement effect are clearly noticeable. The atoms located in the junction region at the edge of the graphene flake undergo the

4. NUMERICAL CALCULATIONS

strongest variation in their net charge charge. From Fig. 4.10 (blue line), the net charge carried can reach up to $-2.27 \times 10^{-2} e$ per atom and Volt, almost twice the maximal value for atoms in the middle of the junction region.

The analysis of the net charge distribution across the graphene sheet leads to following conclusions. First, the charge transfer is significant only in a limited region underneath the tube. The spatial extent of this region is about a few atomic rows. The net charge carried by the atoms outside this region is insignificant. Secondly, the charge distribution is homogeneous in the junction region along the direction of the tube axis. Finally, the net charge value is significantly higher for graphene edge atoms. This particular region needs consequently further studies (See. 4.8)

Capped CNT

Since it is not clear which structure the termination of the CNTs has, both cases, open-ended and capped, have been considered in the calculations. The influence of the termination on the charge distribution is addressed in the following part. Open-ended CNTs exhibit sharp edge termination, leading to a strong charge enhancement at the edges as seen in the previous section. Because the half-fullerene structure used as a cap has smoother edges, capped CNTs are expected to show less charge enhancement effect.

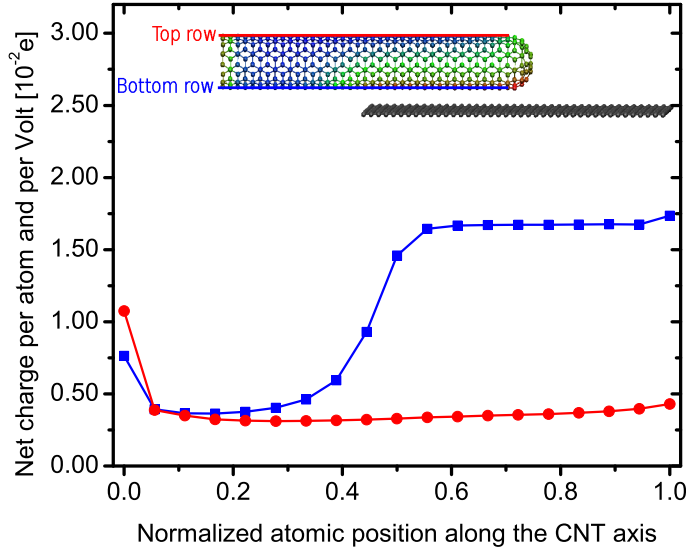


Figure 4.11: Atomic charge density for a capped CNT (5,5) of a CNT (5,5)-Graphene junction. The charge has been represented for the top atomic row and for the bottom atomic row.

Closing the end of the CNT does not modify significantly the charge distribution in the central part of the CNT as observed in Fig. 4.11. The charge profile along the tube follows the same trend as seen in Fig. 4.8. The values of the charge match those for the case of open-ended CNT. In contrast, the edge effects are much less prevalent at the

junction end of the capped nanotube as they are for the case of an open-ended CNT. The atom carrying the maximal charge in the CNT is still found at the termination of the CNT, but exhibits a lower charge. Indeed, for a open-ended CNT, the maximal charge was $3.10 \times 10^{-2} e$ per atom and per Volt while for a capped nanotube it is only $1.91 \times 10^{-2} e$ per atom and per Volt as shown in Fig. 4.12. The charge distribution in the half-hemisphere cap is in agreement with the trend already pointed out that atoms closer to the graphene sheet undergo the highest net charge variations. The top atoms in the cap exhibit charge values ($\sim 0.50 \times 10^{-2} e$ per atom and per Volt) similar to the top row atoms in the central part of the CNT.

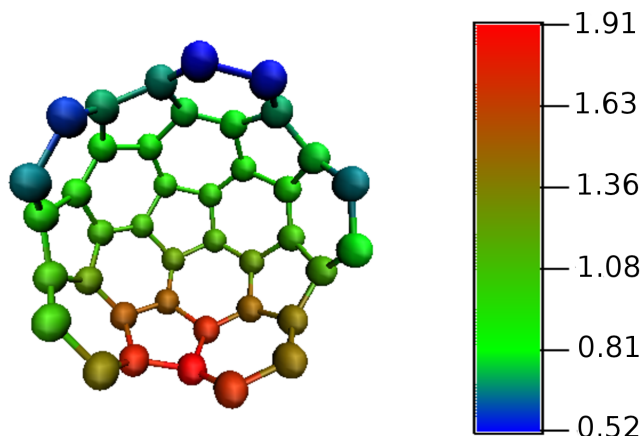


Figure 4.12: Charge distribution in the C_{30} molecule used as cap for the CNT (5,5). The color scale indicates the value of the net charge per Volt in $\times 10^{-2} e$.

The analysis of the cap-induced changes on the charge (Fig. 4.13) leads to identify two different regions in the graphene sheet. The upper half of the graphene sheet concentrate the highest variation in the charge. As expected, the atoms closest to the cap experiences the most significant variations. For the atoms closest to the cap, the increase in the charge is almost three times larger than for the open-ended CNT. These atoms already showed charge values in the open-ended CNT case around $0.50 \times 10^{-2} e$ per atom and per Volt, the capping results then in a significant increase in their charge value. Further away along the length of the sheet, the atoms experience some variations in their charges (green colour in Fig. 4.13) but still do not carry significant charge. The values are close to the neutrality. The charge distribution does not present any change in the lower half of the sheet, where the tube is located (region below the black line in Fig. 4.13). Thus, the structure of the CNT ends does not influence the charge distribution in the junction region.

4.8 Effects of the edges of the graphene flake

In the previous parts, the conclusions for the charge distribution were drawn mostly based on the regions of the sheet labeled as "middle of the junction" regions, where the charge profile was almost constant along the width of the sheet. As already pointed

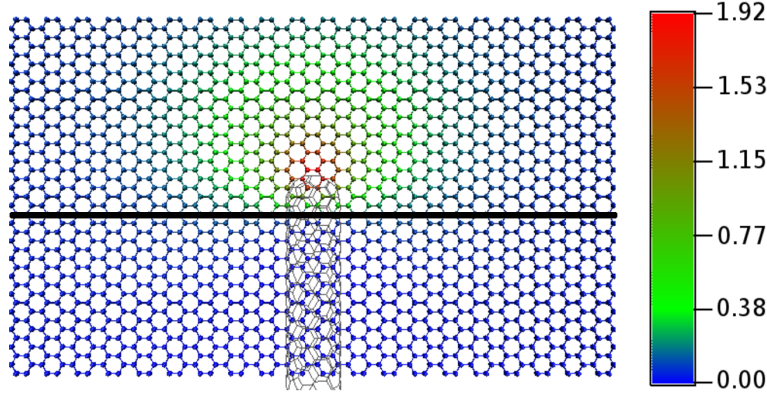


Figure 4.13: Relative difference in the charge density in the junction region part of the graphene flake when considering a capped nanotube over an uncapped nanotube. The relative difference is given by: $(q_{gra,capped} - q_{gra})/q_{gra}$ and is indicated with the color scale. Below the black line, the charge distribution is not affected by the CNT end structure.

out in Sec. 4.7, the charge distribution for the edge of the graphene sheet contrasts with that for the rows in the middle of the junction. There the charge enhancement was stronger. Fig. 4.15 shows that the maximal charge value on the edge row is $\sim -2.27 \times 10^{-2} e$ per atom and per Volt while for the middle part of the junction, it is only around $\sim -1.22 \times 10^{-2} e$ per atom and per Volt. The electrostatic charge enhancement at the edge of a structure can be invoked to explain the higher net charge values exhibited by the atoms forming the edge of the graphene sheet.

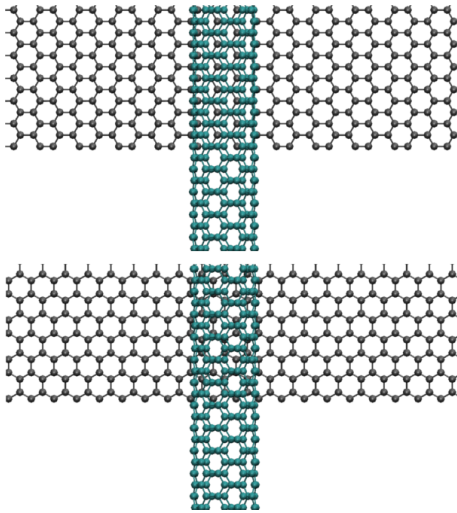


Figure 4.14: Edge of the junction region. Top: Armchair configuration. Bottom: Zigzag configuration.

For the edge row, besides the higher maximal value, the peak in the charge profile has a broadened shape, meaning that the charge accumulation extends further into the graphene sheet. Indeed, the length for which the charge value is 5% of the maximum was found to be for the edge row about $l_{5\%max} \sim 3.30$ nm while for the middle of the junction $l_{5\%max} \sim 1.90$ nm. Here this length can not be used to measure the influence of the CNT as it has been in as defined in section 4.5, since additionally to the CNT effects, the electrostatic edge enhancement effects have to be taken into account.

So far, the calculations were carried with armchair edges for the junction region as represented in top of Fig. 4.14. For completeness, calculations were performed for junctions with zigzag edges as shown at the bottom of Fig. 4.14. As illustrated in Fig. 4.15, for both edge

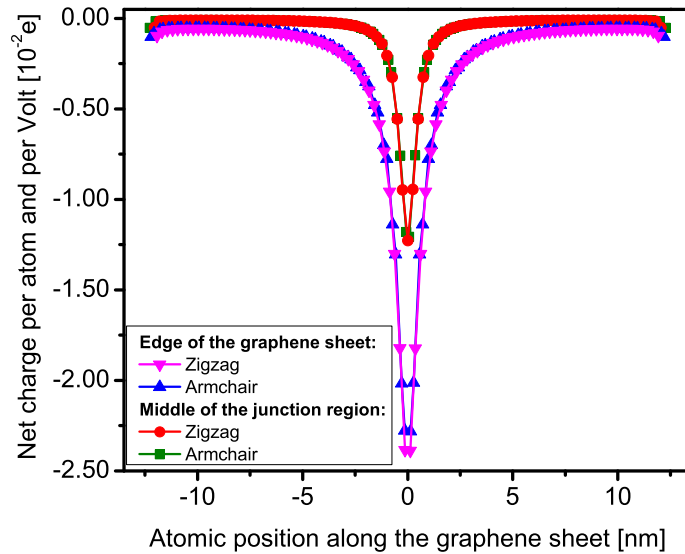


Figure 4.15: Charge per atom in the junction region along the width of the graphene flake for different edge configurations. Charge profile has been drawn along the graphene edge taking part in the junction and for the middle of the junction.

configurations, the maximum value for the charge in the graphene flake is located in the junction region and on the closest atoms to the CNT.

Overall, the edge configuration (armchair or zigzag) does not have a significant influence on the net charge. Only the atomic row forming the edge itself presents some contrast. For this atom row, the atoms of the zigzag edges have a higher charge accumulation value than their armchair counterpart. A slightly larger accumulation of about $-2.38 \times 10^{-2} e$ per atom and per Volt is found for zigzag edges compared to $-2.26 \times 10^{-2} e$ per atom and per Volt for armchair edges. For atoms located away from the edges, as expected, the influence of the edge configuration is not discernible. The values for the maximal charge for both the zigzag configuration and armchair configuration is $\sim -1.22 \times 10^{-2} e$ per atom and per Volt.

Considering $l_{5\%max}$ for a cut along the graphene in a middle of the junction, there is no significant variation due to the type of edge involved in the junction ($l_{5\%max} \sim 1.90$ nm). Even on the edge row $l_{5\%max}$ does not show a significant contrast between both edge configuration ($l_{5\%max} \sim 3.40$ nm for zigzag edges, $l_{5\%max} \sim 3.30$ nm for armchair edges).

4.9 Conclusion

The charge distribution has been computed for a CNT/graphene system using the "charge-dipole" model, a 3D electrostatic model. It scales down to the atom allowing a more accurate description than the analytical calculations presented in Sec. 3.

The analysis of the charge distribution shows clearly two regions for the graphene sheet:

4. NUMERICAL CALCULATIONS

- a high charge concentration region in the vicinity of the CNT/graphene interface. In this region, the charge is homogeneous in the graphene sheet along the CNT axis. The maximum charge is carried by the atoms closest to the CNT.
- a low charge concentration region (neutral region) a few rows away from the CNT. The influence length gives a limit where this region is located. For the CNT (5,5), it starts 1.9 nm away from the tube.

The extent of the charge accumulation in the graphene sheet gives an indication about how strong the CNT modifies the graphene beneath and around it. This extension was proven to be limited. Moreover, the influence of several structural parameters on the charge distribution could be studied. Capped and non-capped CNT were used to build the junction. The influence of the CNT termination on the charge distribution in the graphene sheet was found to be confined to a few atoms around the termination. The effect of the graphene sheet edge has been also addressed. The type of edge has no influence on the charge distribution in the high charge concentration region away from the edge. These structural parameters do not modify significantly the charge distribution and therefore are not likely to influence the electronic transport.

If the middle of the junction is considered, the analytical calculations are good enough to study the charge distribution and the extent of the CNT influence over the graphene sheet charges. However, for a more precise analysis, the charge-dipole model has to be used. Because it is a 3D model and it takes the atomic structure into account, the charge-dipole model could address the change in the distribution induced by capping one end of the tube. The charge distribution for different edge configurations could also be studied with the charge-dipole model. The edge effects were found to be limited to the atoms forming the edges. The analytical calculations could not have given access to these informations.

5

Results for the charge distribution

For both models, the main characteristics of the charge distribution of the CNT/graphene junctions have been identified and discussed in Sec. 3 and Sec. 4. One clear main trend emerges from the results: both models indicate that the charge accumulation/depletion is spatially limited to regions around the junction.

So far only small nanotubes have been used for the calculations (i.e., the CNT (5,5)). In the experiments, thin multi-walled nanotubes (MWCNT) have been used to fabricate CNT/graphene junctions. These MWCNT have radii of about an order of magnitude larger than the CNT (5,5). In this section, the charge distribution will be computed for larger tubes and results drawn for the scaling of the influence length with the radius.

Additionally to the radius of the tube, the distance between the tube and the graphene sheet will be modified and the changes induced on the charge distribution are also presented in this section. From the results of electrical transport measurements presented in Sec. 8, the distance between the tube and the graphene turns out to influence dramatically the contact resistance at the junction. The analysis of the change in the charge distribution with the distance could be the first step to understand the contact resistance variation.

5.1 Scaling of the influence length $l_{5\%max}$ with the radius of the CNT

The scaling of the influence length $l_{5\%max}$ with the radius has been investigated by replacing the CNT (5,5) of the previous computations by tubes with larger radius. 12 different armchair CNTs (n,n) with radii ranging from ~ 0.38 nm to ~ 3.35 nm (and the chiral index n ranging from 7 to 50) have been used, giving then twelve different junction configurations. The equilibrium distance between the tubes and the graphene has been inferred from the results of Sec. 2.3.4. The maximum of charge has been defined by considering the charge for the middle of the junction and by determining the maximum along a cut across the graphene sheet.

First, the limited extent of charge accumulation is also observed in case of larger CNT. This trend is clearly revealed when the atoms carrying a charge value higher than 5% of the maximum charge $|q|_{5\%max}$ are represented for larger CNT, as in Fig. 5.1.

Additionally, the lateral extension of the charge redistribution in the graphene sheet tends to be more restricted to regions close to the CNT when the radius increases. This

5. RESULTS FOR THE CHARGE DISTRIBUTION

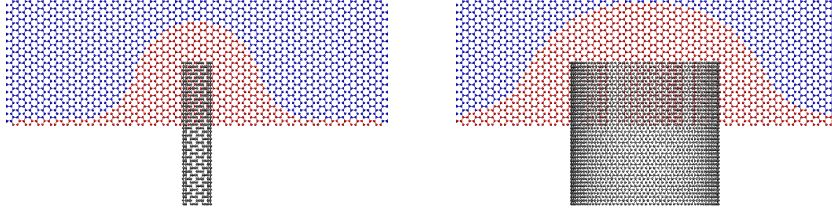


Figure 5.1: View of the extension of the CNT influence on the graphene sheet for a CNT (7,7) (left) and a CNT (37,37) (right). Atoms in red have a charge value $|q| \geq |q|_{5\%max}$, while atoms in blue have a charge value $|q| \leq |q|_{5\%max}$.

trend is clearly observed in the variation of $l_{5\%max}$ with the radius of the CNT for either analytical calculations or charge-dipole model (Fig. 5.2). For each junction configuration, the influence length $l_{5\%max}$ has been determined by considering the maximum of the charge value at the middle of the junction. The influence length increases with the radius of the tube as illustrated in Fig. 5.2 (top), ranging from 2/2.5 nm to 5.5/6.5 nm depending on the model considered. To study how the influence region on the graphene sheet changes with the radius of the CNT, $l_{5\%max}$ has been normalised to the radius of the CNT in Fig. 5.2 (bottom).

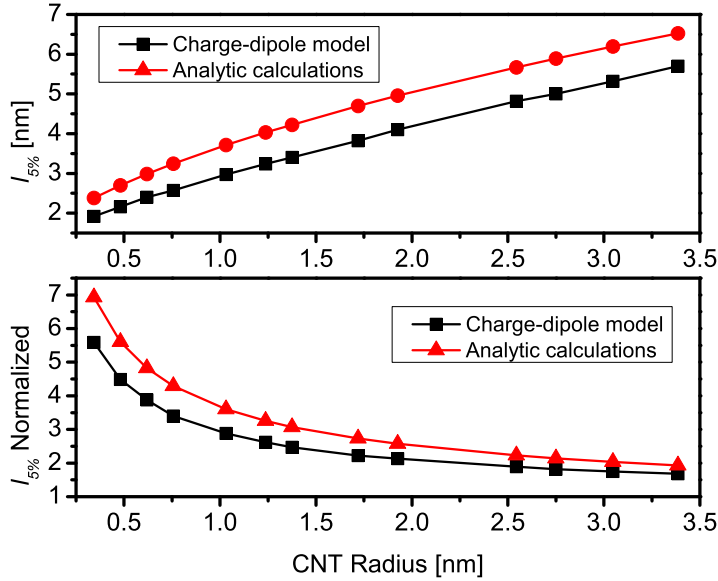


Figure 5.2: Influence length $l_{5\%max}$ versus the radius of the CNT used for the junction (top). $l_{5\%max}$ has been normalised to the radius of the CNT (bottom). $l_{5\%max}$ has been computed analytically and using the charge-dipole model.

The charge-dipole model gives for the CNT (50,50) a normalised influence length $l_{5\%max}$ of only about 1.7 times the radius of the tube itself, while for the tube (7,7) $l_{5\%max}$ is about 4.5 times the radius. The results of the analytical calculations yield higher values for $l_{5\%max}$ but follows the same tendency as the charge-dipole model, $l_{5\%max} = 1.9 \cdot R_{CNT}$ for the CNT (50,50) and $l_{5\%max} = 5.6 \cdot R_{CNT}$ for CNT (7,7).

A important point in the analytical calculations is the lack of edge effects, since the graphene is modeled as an infinite sheet. The values for $l_{5\%max}$ are taken far from the edges in the case of the charge-dipole model. Thus edge effects can be ruled out to justify the differences arising between the two models. A reliable explanation for the different $l_{5\%max}$ values between the two models lies in the charge-dipole interaction that tends to prevent the charge from spreading out in the graphene sheet and pin them in the junction region.

5.2 Effects of the CNT-Graphene distance

The effects of the CNT-graphene distance $d_{CNT-Gra}$ on the charge distribution in the graphene sheet have been addressed in this section. In Sec. 2.3.4, the equilibrium distance between several CNT and a graphene sheet has been computed by means of the semi-empirical PM6-D method. Up to now, no experimental value is available for the equilibrium distance. The experimental value for interlayer distance in graphite is the closest experimental value available. The experimental definition of the graphene-nanotube distance is not straightforward since graphene is not perfectly flat due to thermal fluctuations. Corrugations of up to 1 nm in the out-of-plane direction have been reported in suspended graphene (92). Furthermore the equilibrium distance may vary during the experiment. In particular for back-gated graphene transistors, the gate voltage sweep may draw the tube toward the graphene or push it away. Furthermore, trapped impurities may also locally modify the distance between the two structures. The picture of a perfectly flat junction has then to be modified. Taking into account the range of all modifications is out of scope but as a starting point, the effect on the charge distribution arising from a change in the distance between the CNT and the graphene has been determined.

The CNT (5,5) has been used to build the junction. This tube constitutes the upper limit for the extent of the CNT influence with respect to the radius as seen in Sec. 5.1. The charge distribution profile across the graphene sheet is represented for several $d_{CNT-Gra}$ and for both models in Fig. 5.3. The range of distances used for the calculations covers both experimental and computed ranges, from $d_{CNT-Gra} = 2.4 \text{ \AA}$ to 3.8 \AA .

The overall shape of the charge profile does not change significantly with the distance $d_{CNT-Gra}$. Indeed, the region of influence of the CNT is still confined to a few atomic rows around the CNT and does not extend far into the graphene. The only noticeable modification is the value of the charge distribution peak. The closer the tube to the graphene sheet, the higher the value of the maximum charge. Thus, the variation of $d_{CNT-Gra}$ does only affect significantly the atoms located close to the CNT.

Since both models give the same trend, the charge-dipole model has been used to study in detail the charge variation with the distance $d_{CNT-Gra}$ for atoms close to the CNT, along the row pictured in the top part of Fig. 5.4. The closest atom to the CNT (blue atom in Fig. 5.4) undergoes the strongest change in charge value with increasing distance: it carries a net charge of $-17.3 \times 10^{-2} e$ for $d_{CNT-Gra} = 2.4 \text{ \AA}$ and a net charge of $-7.4 \times 10^{-2} e$ for $d_{CNT-Gra} = 3.8 \text{ \AA}$.

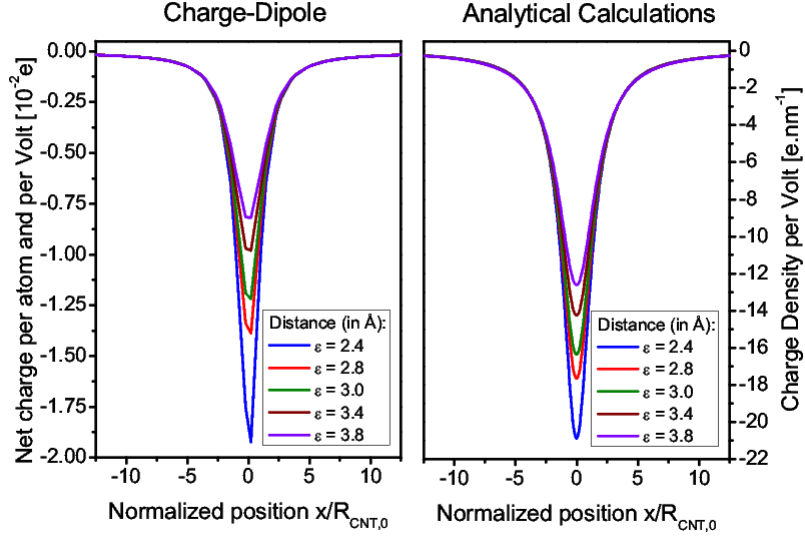


Figure 5.3: Left: Charge profile in the graphene given by the charge-dipole model for different equilibrium distances d_{CNT-Gr} . Right: Charge density profile computed analytically in the graphene for different equilibrium distances d_{CNT-Gr} .

This behaviour is clearly seen in Fig. 5.4, where the charge has been represented for atoms sitting at several distances from the closest atom to the CNT. The charge has been normalised for each atomic row to that for the distance $d_{CNT-Gr} = 2.4 \text{ \AA}$. For the atoms sitting one row to three rows away from the closest atom to the CNT (respectively red, green and brown atoms), the change in the net charge is significant when the distance d_{CNT-Gr} varies. When compared to the charge value these atoms carry for $d_{CNT-Gr} = 2.4 \text{ \AA}$, the charge reduction is about 0.6 times for the first-row atom and about 0.15 times for the third-row atoms. For rows further away, the loss is smaller and it becomes eventually negligible for the atom 5 rows away from the closest one to the CNT (purple atom).

5.3 Conclusion

The charge distribution in the graphene sheet at the junction has been investigated by changing two structural parameters: the diameter of the CNT and the distance between the tube and the graphene.

First, the calculations show that tubes with large diameters have limited influence over the charge distribution in the graphene. The extension of the charge redistribution in the graphene has been found to be less than 2 times the tube radius. This value can be compared to the extension in the graphene sheet of the doping due to metal leads, which is on the micrometer scale.

The change in the tube-graphene distance does affect only the graphene atoms the closest to the CNT. It has no influence on a large scale in the graphene sheet.

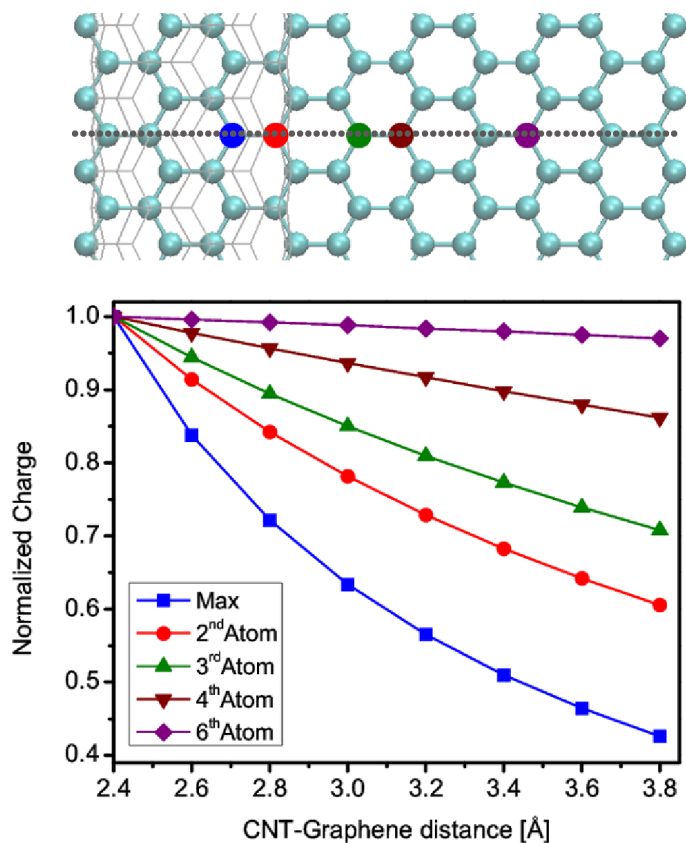


Figure 5.4: Normalised charge versus the CNT-graphene distance for atoms along the row defined in the top figure (dashed line). Along this row, the normalised charge is indicated for the closest to the CNT (Max), the 2nd closest, the 3rd closest, the 4th closest and 6th closest. Top: Zoom in the junction region. The charge of the coloured atoms has been drawn.

These results have helped to characterise the electronic structure of graphene in the vicinity of the tube. They will be used in the experimental part to identify the mechanism governing the contact resistance (see Sec.8.4).

5. RESULTS FOR THE CHARGE DISTRIBUTION

6

Sample preparation

6.1 Introduction

Until now all the graphene/CNT junctions reported in the literature have been made using "stochastic" methods, relying on a random more than on a controlled fabrication process. In the study carried by Pei *et al.* (47), the graphene has been first deposited onto the substrate. The tubes were then directly grown on the graphene by chemical vapor deposition (CVD). Since the growth direction of the tube during the CVD process can not be fully controlled, only few CNT were lying on the graphene flakes. A similar technique has been used to grow SWCNT on pre-patterned arrays of reduced graphene oxide electrodes (rGO) (46). Neither of these studies use pure monolayer graphene to build the junctions but either few-layers graphene or 10-nm thick rGO layers. One reason is due to CVD process step, which is carried out under gas flow and at high temperatures (around 800 – 850 ° C), which weakens the monolayer graphene binding with the substrate and therefore may causes the graphene to fold or to fly away.

The closest realization of a pure monolayer/CNT junction has been reported by Engels *et al.* (93), using the opposite steps sequence as in the previously mentioned studies (Fig. 6.1). The only probed junction was a mixed mono- and bilayer graphene/CNT junctions fabricated by growing the CNTs followed by graphene deposition. Besides, the CNT turned out to consist of bundle of tubes according to AFM characterisation.

The fabrication of controlled graphene/CNT junctions has to overcome several limitations mostly due to the CVD method used to grow the CNTs, as already alluded to in the previous paragraph. An inherent drawback of CVD tube growth is the lack of selectivity over the type of CNT obtained. The chirality of the grown tubes is random. Therefore

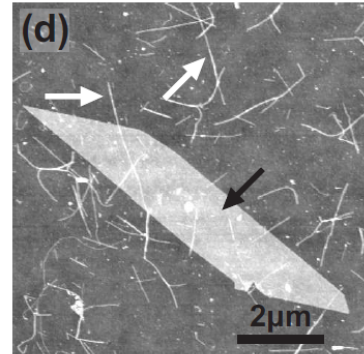


Figure 6.1: AFM picture of CNT/graphene junctions as reported by Engels *et al.* (93). The fabrication method relies on a high concentration of tubes to randomly fabricate CNT/graphene junctions. No control can be achieved on the number and on the position of the junctions.

6. SAMPLE PREPARATION

semiconductive as metallic tubes can end up building up the junction. As an alternative for metal leads to connect graphene, the semiconductive tubes are of no interest since they may introduce a Schottky barrier. Control of over parameters such as the location and the number of junctions fabricated have also proven to be tedious if not impossible. Moreover, the growth of nanotubes by CVD requires a metallic catalyst. Since the purification after CVD may damage the graphene, the samples are contaminated with residual metallic particles (iron, copper,...).

In this work, a graphene/CNT junction fabrication technique has been developed that tries to overcome the hurdles previously mentioned. Instead on relying on CVD to grow the tubes, a wet deposition technique has been used combined with atomic force microscopy nanomanipulation. With the developed technique over more than 250 monolayer graphene flakes could be connected with CNTs.

MWCNTs were preferred over SWCNTs as building block for the junction. MWCNTs are well suited to connect to graphene because they most likely exhibit a conductive behaviour. Indeed, the gap energy is inversely related to the diameter of the CNT. For the MWCNTs used in this work, the diameter ranges from 9 nm to 12.5 nm which corresponds to a gap energy of 0.0306 to 0.0426 eV, close to the value for the thermal voltage $k_B T \simeq 0.0258$ eV at room temperature ($T=300$ K). Unlike the SWCNTs, no separation step needs to be performed to sort out MWCNTs and ensure they are metallic. Control over the position as well as over the number of junctions fabricated has been ensured by dragging off selected tubes onto the graphene with the tip of an atomic force microscope (AFM). Indeed, the AFM in-plane scanning range allows an accurate positioning of the MWCNTs on graphene. The CVD inherent catalyst particle contamination could be avoided by spin coating MWCNTs in solution directly onto the workpiece. In addition, the nanomanipulation process allows a mechanical "cleaning" of the tube. As the tubes are dragged onto the substrate, a trail of the surfactant molecules is left behind.

6.2 Graphene

6.2.1 Substrate preparation

Highly doped silicon wafers with a 300-nm thick thermal oxide layer on top have been used as substrate for all the experiments and could act as back gate. Arrays of markers were deposited onto the wafer using e-beam lithography (described in Sec. 6.5) to ensure a proper orientation and alignment on the substrate. The metals deposited for the alignment markers, either palladium or gold, were chosen for giving a good scanning electron microscope contrast. After cleaning and removing the residual impurities by means of an oxygen plasma, the wafers were cut into small pieces of less than 1 cm length.

6.2.2 Graphene deposition

Natural graphite flakes from the company NGS Naturgraphit GmbH were used as raw material for the graphene fabrication (94). Natural graphite was preferred over highly oriented pyrolytic graphite (HOPG), since it presents monocrystal domains of a larger

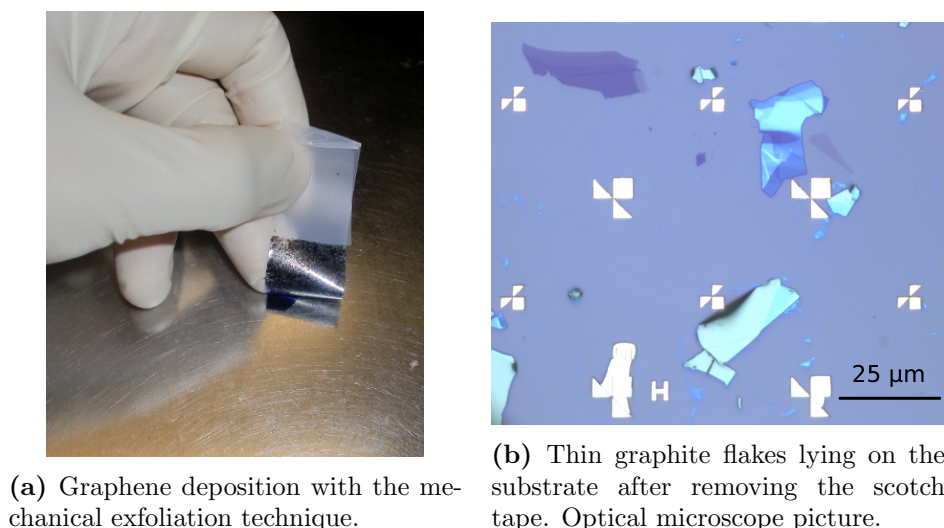


Figure 6.2: Graphene deposition

extension than HOPG, therefore yielding larger graphene flakes. The graphene flakes were obtained by means of the mechanical exfoliation technique. This graphene production method was first reported by Novoselov *et al.* in 2004 (2) and takes advantage of the graphite structure. The weak interlayer van der Waals interaction facilitates breaking the interlayer bound and peel the bulk graphite.

The "scotch tape technique" is used to cleave graphite by removing a few layers from it (Fig. 6.18a). The scotch tape is then folded a couple of times to thin the graphite flakes sticking on the tape down to a thickness of few atomic layers. The tape is then pressed onto the substrate leaving a random stack of flakes of different thickness on it, as seen on the optical microscope image in Fig. 6.2b. The random distribution and size of the flakes combined with the lack of control over the thickness make it arduous to spot and identify graphene sheets on the substrate.

6.2.3 Graphene characterisation

Optical microscopy

The next step after the graphene deposition consists of an optical check of the substrate performed using an optical microscope at high magnification.

Although graphene is only one atom thick, one of its most striking features is the contrast it presents with the SiO_2/Si substrate, as first reported by Blake *et al.* (95). Roddaro *et al.* (96) explained this effect by the very sensitive transparency dependence of the graphite layers on their thickness. The "relative amplitude of the interfering [reflexion] paths" along the air/graphite/ SiO_2 interface can be modulated depending on the thickness of the

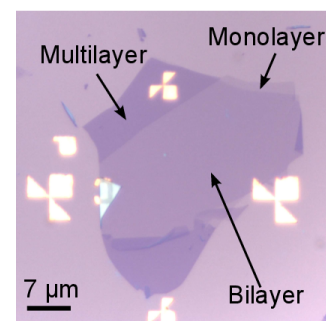


Figure 6.3: Optical microscope picture showing the contrast between mono-, bi- and multilayer graphene. The lower the contrast, the thinner the flake.

6. SAMPLE PREPARATION

graphite flake, leading to "resonant cancellation of reflection by destructive interference at specific wavelengths" that can be detected with the optical microscope.

Monolayer graphene sheets present the lowest optical contrast of all graphitic sheets. In practice, the sample is scanned with an optical microscope, searching for flakes presenting low optical contrast. These flakes are strong candidates to be mono-layer or at least few layer graphene. Fig. 6.3 gives a hint at how strong is the optical contrast for mono-, bi- and multilayer graphene is. The optical characterisation technique is a first means to sort out of the material lying on the substrate. But since this technique relies on the human eye and appreciation, a second characterisation is performed to validate the optical observation.

Raman spectroscopy

Raman spectroscopy is a fast and non-destructive technique to characterise graphene flakes with thickness of up to at least 3 layers. It has already been intensively used to study other sp^2 -carbon structures. For example, metallic and semiconductive nanotubes exhibit features in their Raman spectra that can tell them apart (see (97) for a review on Raman spectroscopy on CNT). The first Raman spectroscopy study on graphene was reported by Ferrari *et al.*, in 2006 (98), and since then Raman spectroscopy has become a standard characterisation method for mono-, bi- and multilayer graphene (99, 100). The Raman effect rises from the interaction between on one side photons and the other side atoms and molecules. Photons are likely to undergo elastic scattering from the atoms and molecules, the incoming and the scattered photon have then the same kinetic energy and therefore the same wavelength. This phenomena is known as "Rayleigh scattering". A small proportion of photons however may be scattered inelastically, exciting in that case a phonon. The scattered photon may have a lower energy (Stokes scattering) or a higher energy (anti-Stokes scattering) than the incoming photon. Thus the wavelength of the scattered photon exhibits a shift with respect to the one of the incoming photon. This shift is detected by a spectrometer and the Raman spectrum can be inferred (intensity of the scattered photons versus the wavelength shift).

The Raman spectrum of graphitic structures presents three remarkable peaks: the G peak located at around 1580 cm^{-1} , the G' peak (also termed as 2D peak in the literature) and the D peak. The position of the last two peaks depends on the excitation wavelength, showing a dispersive behaviour.

For a wavelength of $\lambda = 633\text{ nm}$, the position of the D peak is around $\sim 1350\text{ cm}^{-1}$ and the G' peak appears around $\sim 2700\text{ cm}^{-1}$. The G peak is due to a first-order Raman

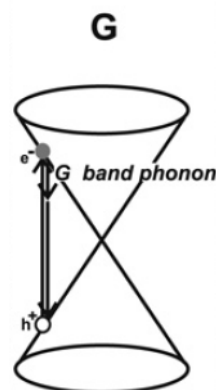


Figure 6.4: G peak mechanism: creation of an electron-hole pair by the incident photon and recombination involving in-plane transversal or longitudinal optical phonon. Source: L.M. Malard *et al.* (100)

scattering process involving the doubly degenerate in-plane transversal and longitudinal optical phonons at the Γ point of the Brillouin zone (see Fig.6.4). The incident photon creates an electron-hole pair. The electron then excites either an in-plane transversal or longitudinal optical phonon and recombines emitting a photon with lower energy.

In contrast, the D and G' peaks are due to second-order double-resonance Raman scattering processes (Fig. 6.5). Both processes start with the creation of an electron-hole pair by the incident photon. During the G' peak process, the created electron interacts with an in-plane transversal optical phonon and is scattered inelastically to a state in the opposite valley of the Brillouin zone.

A second inelastically scattering process also occurs with an in-plane transversal optical phonon but the electron is scattered back to the initial valley.

When the electron is recombining, the emitted photon has a lower energy than the incident one. In the D peak process, an elastic scattering by a defect replaces one of the two inelastic scattering processes occurring in the G' peak process. In addition, the D peak process is an intra-valley process.

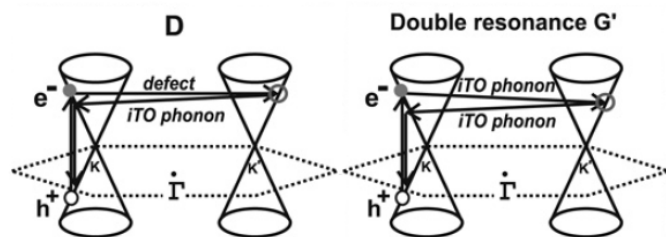


Figure 6.5: D and G' peaks mechanism: second order double-resonance Raman scattering. iTO phonon stands for in-plane transversal optical phonon. Source: L.M. Malard et al. (100)

The Raman spectroscopy allows two characterisations for the graphene flake. First, the Raman spectrum yields information on the quality of the flake. Since the D peak process involves defect scattering, the intensity of the peak can be linked to the number of defects in the flake. Secondly, the thickness of the graphene flake can be determined since the shape and the intensity of the G' peak change with the number of layers. The G' peak process is sensitive to the band structure around the Dirac point because of the electronic states involved in the process. Mono-, bi-, tri- and multilayers present a significantly different band structure around the Dirac point and present therefore different peak features. As shown in Fig. 6.6, the spectrum of monolayer graphene exhibits a sharp symmetric G' peak that can be described by a Lorentzian function. The spectrum of a bilayer shows overall a broader G' peak with a noticeable hump at low-energy side of the peak. The G' peak can be fitted by four Lorentzian functions each accounting for one Raman scattering process involved. With increasing number of layers, the G' peak broadens and loses in intensity. It tends thus to exhibit features similar to the graphite G' peak.

The Raman spectrometer used for the graphene characterisation at the INT is a customised WiTec Micro Raman. It is integrated into an optical microscope used to locate precisely the flake to be analysed. Once the position is found, a helium-neon laser with a wavelength of 633 nm is focused to a spot on the graphene sample. Particular attention has been paid to the thermal stability of the measurement, keeping the power of the incident laser around ~ 1 mW to prevent sample heating. The spectrometer is made of two sensors: a 1024 channel charge-coupled device (CCD) for broad spectrum recording and

6. SAMPLE PREPARATION

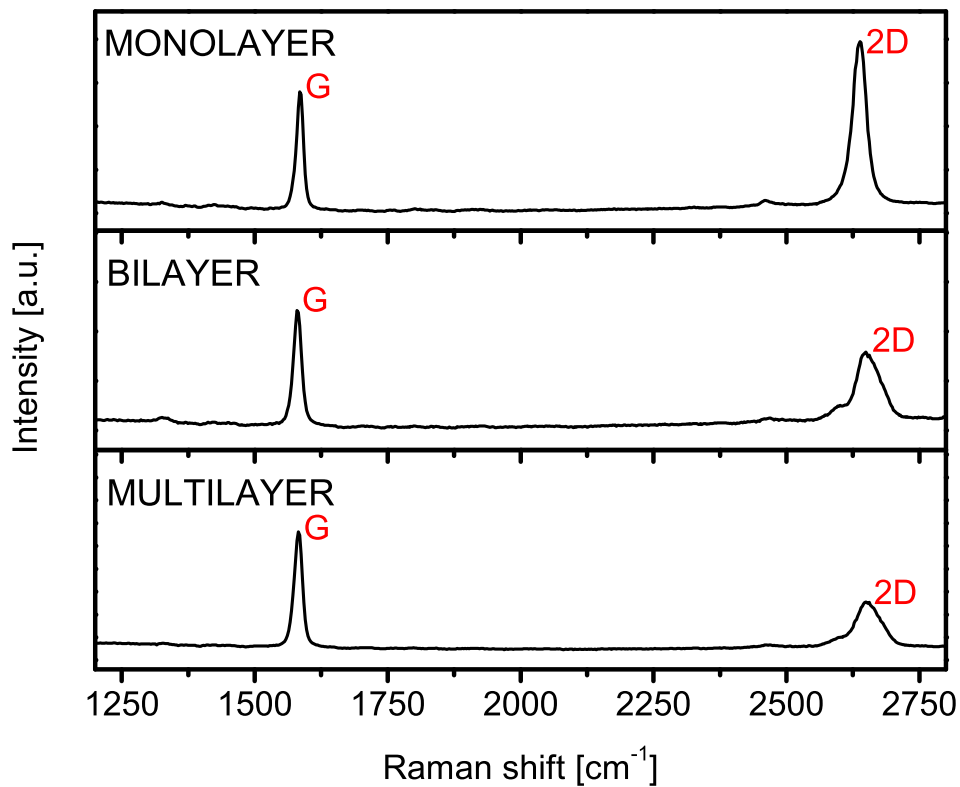


Figure 6.6: Raman spectra for a mono-, bi- and multilayer graphene on Si/SiO₂ substrate. The peaks G and 2D are indicated.

an avalanche photodiode (APD) for precise measurements at a given wavelength. When using the CCD, the integration times was set to 90 s.

6.3 Multi-walled carbon nanotubes

6.3.1 Solution of carbon nanotubes

The carbon nanotubes used for the samples are thin multi-walled carbon nanotubes (MWCNT). They were produced by catalytic chemical vapor deposition by the company Nanocyl (reference number NC3100 (101)). The data sheet gives scanning probe microscope measurements about $\sim 1.5 \mu\text{m}$ for the average length and about $\sim 9.5 \text{ nm}$ for the average diameter. The MWCNT are in powder form and therefore need to be put into solution for further applications. CNT are insoluble in water or organic solvents as they tend to aggregate into bundles. Their large surface area and high flexibility helps the attractive van der Waals forces to bind the CNTs together. To obtain a dispersion of CNT a common method is the use of surfactant. The surfactant molecules are adsorbed on the CNT surface and wrap the tubes, as seen in Fig. 6.7, thus keeping them separated from each other. To prepare the dispersion a few grams of MWCNT powder are put in an aqueous 2 % sodium cholate solution. Sodium cholate (chemical formula: $\text{C}_{24}\text{H}_{39}\text{O}_5\text{Na}$), is a bile salt commonly used as surfactant for CNT dispersion (103). The solution is sonicated to separate the tubes already packed into bundles, thus allowing the surfactant to intercalate between the tubes. A purification step to remove the amorphous carbon and residual impurities is then performed using a centrifuge. After this step, the dispersion is ready but contains tubes with a broad length distribution.

Tubes of about $\sim 1 \mu\text{m}$ to $1.5 \mu\text{m}$ are well suited for building the junction. Tubes out of this length range would act as a hurdle in the nanomanipulation phase. An additional step to sort out the tubes by the length is then performed with the size-exclusion chromatography technique (SEC). This technique is based on transit time through a porous medium which depends on the molecule's length. The solution is poured into the top of a column filled with porous gel and slowly passes through the column. Long nanotubes cannot enter the pores and thus come out first at bottom of the column. Short tubes enter the pores, having then a longer transit time through the column and thus coming out later. The emerging solution is stored in chronologically labeled fractions.

6.3.2 Characterisation

Since long nanotubes have a short transit time in the SEC column, only the first fractions of the SEC are of interest for the fabrication of CNT/graphene junctions. To assure that

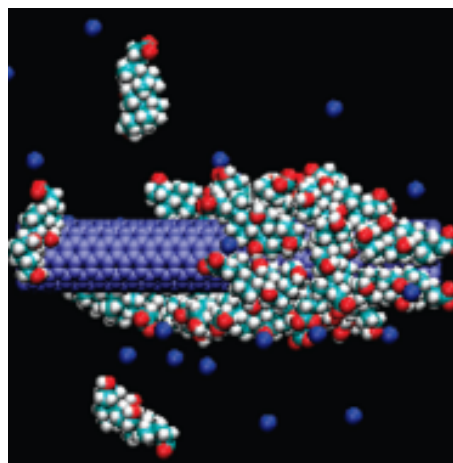


Figure 6.7: Results of molecular simulation showing how sodium cholate (SC) molecules wrap a CNT (6,6) (blue molecule). Two single SC molecule are represented on top and at the bottom of the picture. The calculations and the picture are taken from (102).

6. SAMPLE PREPARATION

the nanotubes contained in a fraction are well suited, a few drops of the fraction are spin-coated on a clean substrate. Next, the substrate is washed with distilled water to remove the surfactant.

A scan of the substrate in few areas is then performed using an atomic force microscope (AFM), yielding information on the length and on the diameter of the tubes, as seen in Fig. 6.8. As inferred from height profiles of Fig. 6.8, the diameter of the selected tubes ranges from 9 nm to 12.5 nm.

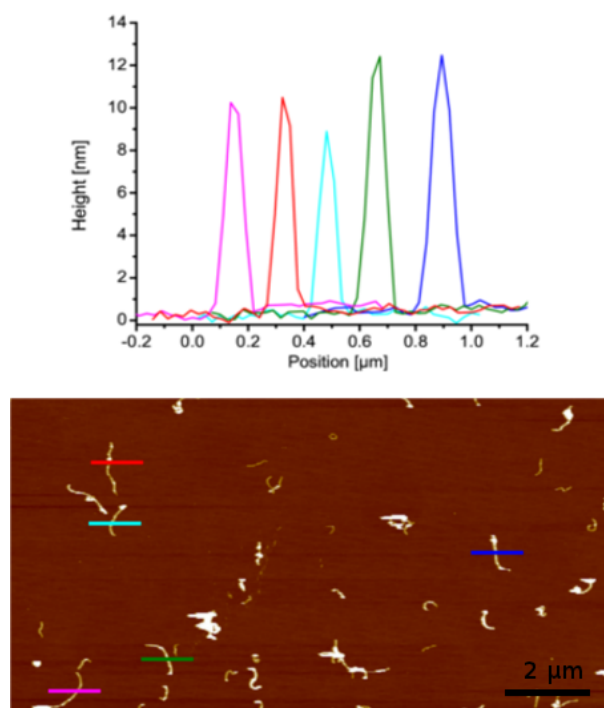


Figure 6.8: Atomic force microscopy (AFM) image of multi-walled carbon nanotubes spin-coated on a silicon substrate. The height profile is represented along the coloured cuts. The height profiles have been shifted with respect to each other for better visibility.

Additional parameters concerning the quality of the dispersion itself can be inferred from the AFM pictures. Indeed, the homogeneity of the dispersion as well as its stability over time can be checked easily along with the tube concentration. To illustrate this, the AFM picture of a poor-quality dispersion is shown in Fig. 6.9. Tubes are scarce on the substrate and are mostly bundled together as seen on the left part of the picture. The small dots on the top right part are remnants of surfactant. The bigger particles are impurities contained in the solution and that were not removed by the centrifugation process.

Once the parameter and quality checks have been run and the best suited fraction has been determined, the MWCNT are deposited onto the graphene samples with the spin-coating technique already used for the analysis of the SEC fractions. This time a few drops of the MWCNT solution are put on the graphene sample. The sample is then rotated at around 4000 rpm. Distilled water is used afterwards to clean the sample. This deposition step has proven to be critical for the graphene sheet, since it may happen that

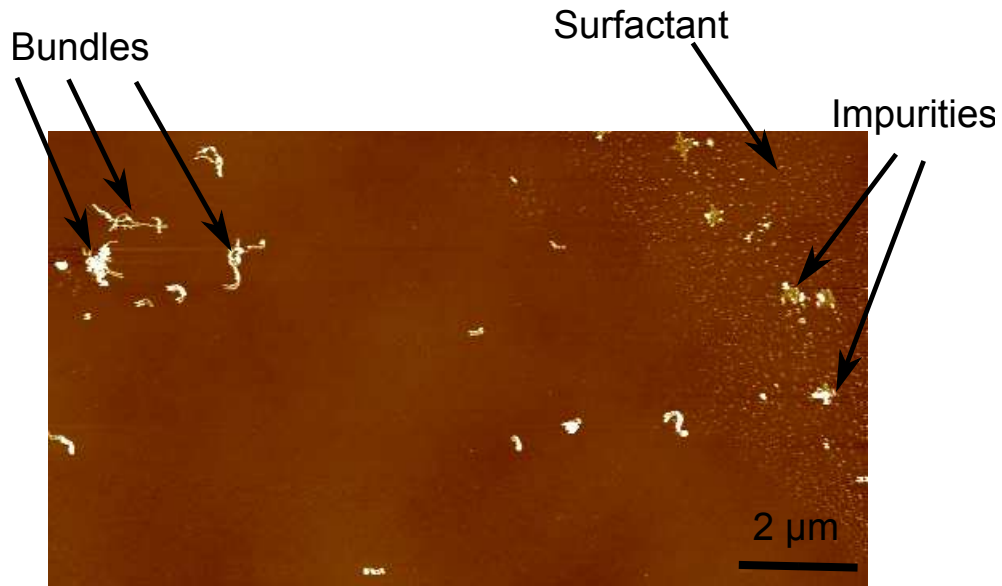


Figure 6.9: Poor quality MWCNT dispersion spin-coated on a Si/SiO₂ substrate. MWCNT bundles, surfactant rest and impurities, as well as low tube concentration are clearly visible on the AFM picture

the sheet folds back on itself because of the combined effects of the surfactant and of the centrifugal force.

6.4 Nanomanipulation of MWCNT

Several steps of the MWCNT/graphene junction fabrication process make use of an atomic force microscope (AFM). The primary function of an AFM is to image and to measure areas on a micrometer scale down to the atomic scale, acting thus as a control tool. As already mentioned, the AFM picture is used to determine the quality of the MWCNT solution.

After the MWCNT deposition on the graphene sample, an AFM picture of the graphene sheet and its surrounding region is also taken to assure that enough nanotubes are lying close to the graphene. The AFM is used again at the very last step of the fabrication process to check the final result.

The operation mode for the AFM through all the experiments is the so-called "intermittent contact mode" (IC-Mode) also labeled as "Tapping Mode". In this mode, a piezoelectric drives the cantilever to oscillate with a frequency close to its resonance frequency (standard value: 95% of the cantilever resonance frequency), letting the tip come briefly into contact with the sample surface. Common tapping mode cantilevers (such as the NSC15 from the MikroMasch company (104)) have a resonance frequency about 300 to 350 kHz. The amplitude of the oscillations is usually used as feedback control parameter. When the tip comes close to the sample surface, the amplitude of the tip oscillation is reduced due to the attractive forces. The topography of the surface can then be monitored by the error signal between the measured amplitude and the set-point amplitude as well

6. SAMPLE PREPARATION

as the height profile. The IC-Mode has been preferred over the contact mode (C-Mode), in which the tip is constantly in contact with the sample. This could lead to damaging the sample because of the repulsive forces arising between the tip and the sample when they are in contact.

The use of the AFM tip as a "nanomanipulator" has already been reported for pushing particles or clusters on diverse substrates (105, 106, 107, 108). Among other molecules, MWCNT can be manipulated and arranged to build devices without undergoing structural damage (109, 110, 111). The usual manipulation procedure relies on switching off the feedback loop so that the tip comes close to the sample surface. The tip is then used as a "rake" to push or pull the nanotube along the scan direction.

The manipulation and the control require three scans:

- First scan (Fig. 6.10a): feedback loop on. The MWCNT to be manipulated is imaged as well as the surrounding area.
- Second scan (Fig. 6.10b): feedback loop off. From the set-point position, the tip is lowered from a selected distance $-z_{offset}$. The slow scan axis is disabled so that only a selected line is scanned. The tip comes into contact with the MWCNT. While the tip moves, the MWCNT is pushed along the scan direction.
- Third scan (Fig. 6.10c): feedback loop on. A scan is performed to check the new position and orientation of the MWCNT.

The second scan is the critical step in the manipulation process since disabling of the feedback loop may lead the tip to crash onto the sample. Because the distance between the tip and the sample can not be known precisely, the optimal distance the tip as to been lowered from the set point position is determined stepwise. Before performing the scan with the feedback loop off, the tip is lowered from a distance $-z_{offset}$ from the setpoint position. During the scan, the distance between the tip and the CNT is monitored by the amplitude signal. To prevent a crash, $-z_{offset}$ is increased gradually after each scan. As the tip comes closer to the sample, the amplitude signal decreases and eventually reaches zero when the tip contacts the sample, giving the optimal $-z_{offset}$.

One limitation of the manipulation is the high needs of AFM tip. The tips are easily worn out as the disabled feedback loop does not prevent them on pressing onto the substrate. Moreover, impurities such as glue rest due to the graphene fabrication process may accumulate on the tip apex resulting on a blunt tip. In some rare cases, during the manipulation process the MWCNT may stick to the tip and no reliable method has been found to retrieve it.

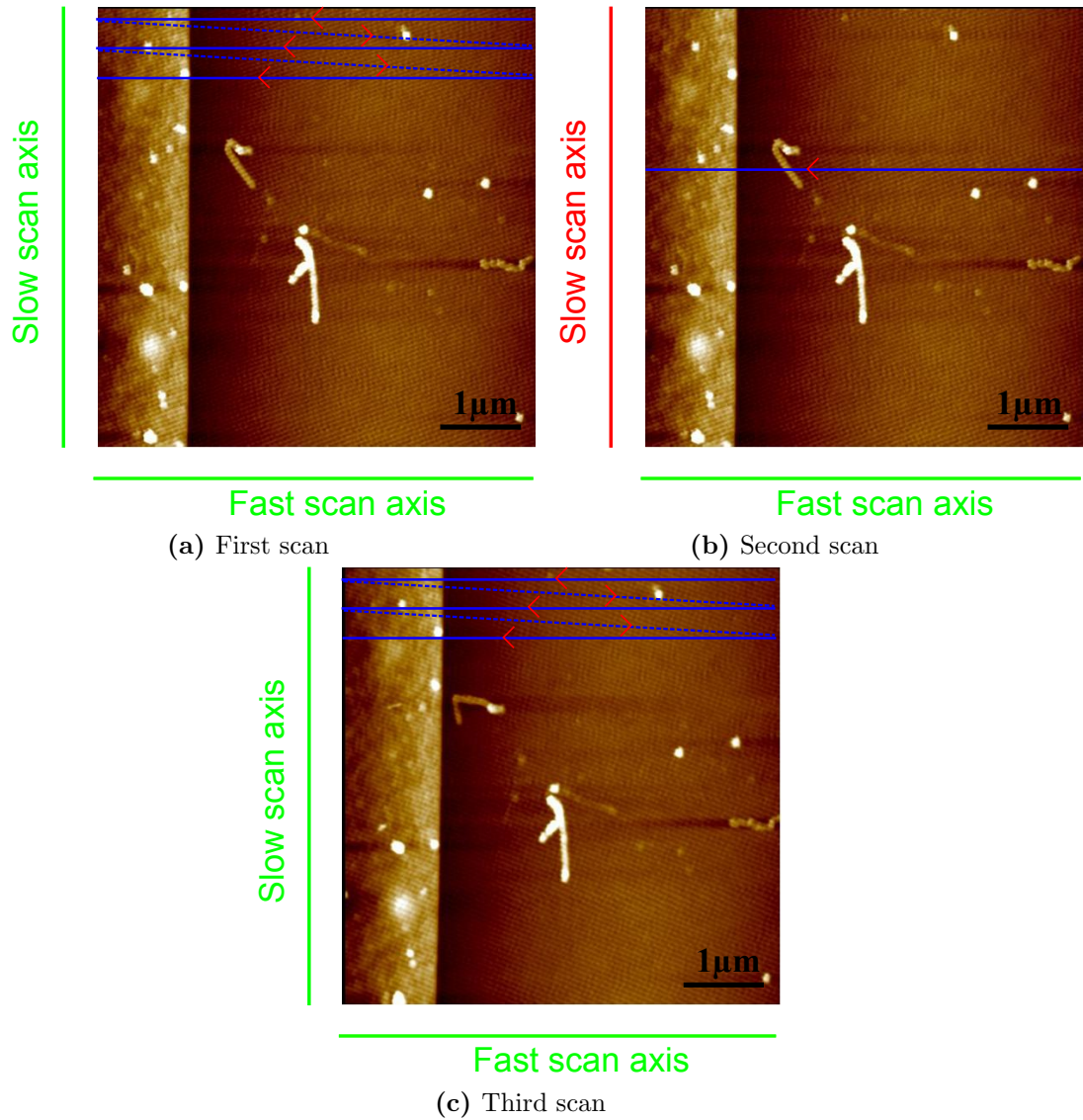


Figure 6.10: MWCNT manipulation procedure. The red arrows indicate the scan direction. For each scanned line, two sets of signals are recorded: for the forward (solid blue lines) and for the backward direction (dashed blue lines)

6. SAMPLE PREPARATION

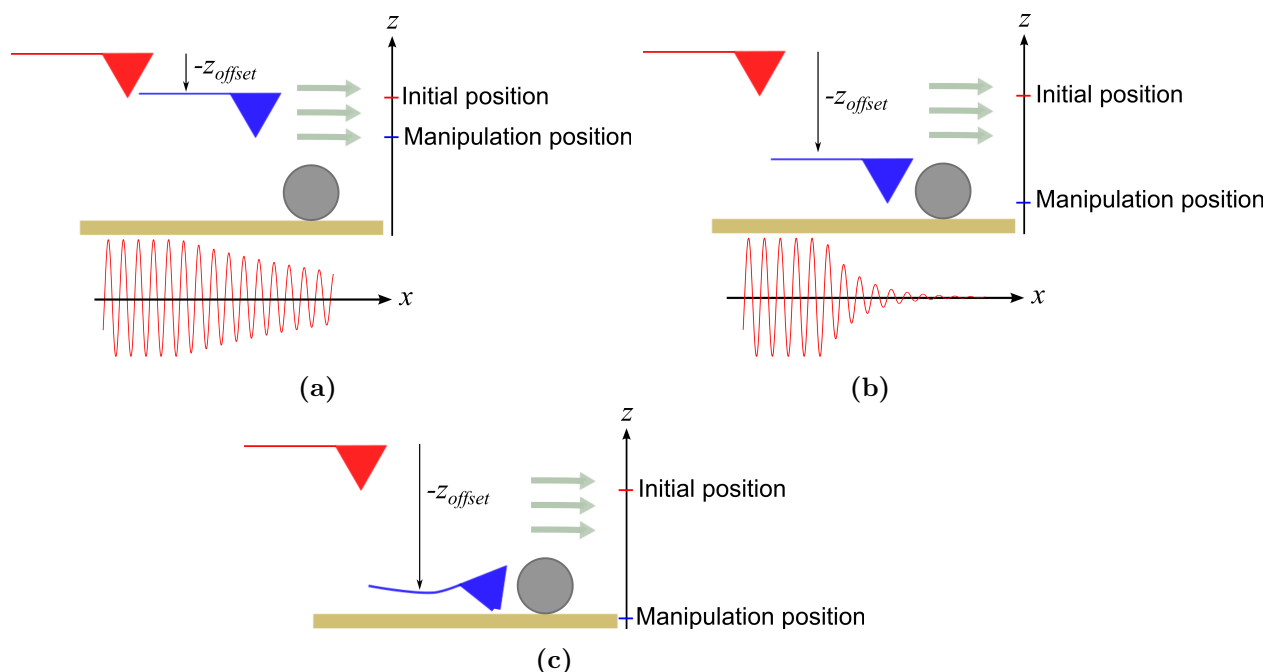


Figure 6.11: Schematic representation of the tip lowering process. The tip is lowered from a distance $-z_{offset}$. The set-point distance is taken as reference for the distance $-z_{offset}$. The oscillation amplitude along the scanned line is represented below the first two pictures. Fig. 6.11a: The distance $-z_{offset}$ is too large to bring the tip in contact with the tube. The amplitude signal does not vanish but slightly decreases when the tip scans the tube. Fig. 6.11b: The distance $-z_{offset}$ is the optimal distance for the nanomanipulation. The amplitude signal vanishes as soon as the tip come into contact with the tube. Fig. 6.11c: The distance $-z_{offset}$ was set too high, the tip crashed onto the sample.

The AFM used at the INT for imaging and nanomanipulation are the MultiMode and the Dimension Icon, both from the company Bruker. The Multimode operates with the Nanoscope controller III while the Dimension Icon runs with the upgraded version of it, the Nanoscope controller V.

The difference in the controllers makes the nanomanipulation more tedious when using the MultiMode. Indeed, its controller does not allow any reorientation of the scan direction without rotating the scan window. Moreover the Dimension Icon software comes with a mode (termed as "NanoMan") that helps to set the proper parameters for the nanomanipulation.

After the nanomanipulation step, 6 to 15 MWCNT are lying on the graphene flake depending on the flake size and configuration. Each of them forms a MWCNT/graphene junction as shown in Fig.6.13. An AFM picture is taken with at least one alignment marker on it. This is essential for the lithography step to ensure a proper alignment of the contacts with the sample.



Figure 6.12: Dimension Icon AFM



Figure 6.13: AFM picture of a sample ready for the lithography step. 11 MWCNT have been dragged off onto the graphene flake. On the left side, an alignment marker is visible.

6.5 Electron beam lithography

Once the MWCNT/graphene junctions have been fabricated, the device needs to be connected to the measurement set-up. In this scope, metallic contacts and leads are deposited on the sample. The first step is the fabrication of a mask on the sample surface. The mask leaves exposed the parts of the sample where the metal should be deposited and protects the rest of the sample by covering it. A usual technique to create masks with nanometric to micrometric features is the electron-beam lithography (e-beam lithography).

For that a layer of resist, mostly a polymer, is used to cover the sample. In the case of the so-called positive resists, the exposure to the electron beam triggers a scission in the polymer main chain breaking the bounds between the atoms. The exposed regions of the resist consist of smaller molecules that can be dissolved by an appropriate solvent (selective solvent).

First, the sample is coated with a polymethyl methacrylate layer (PMMA). The PMMA is a commonly used positive resist in e-beam lithography. A few drops of a commercial 4.5 % solid PMMA solution in anisol from the company All-resist GmbH are deposited onto the sample.

The thickness of the layer obtained by spin-coating depends on the rotation speed. The lithography parameters such as the exposure time, the doses and the beam dwell time have been optimized for a 200 nm thickness PMMA layer. The benchmarks given by the PMMA manufacturer indicate a 200 nm thickness layer for a rotation speed of 6000 rpm. Ellipsometry measurements confirmed the value for the thickness. The sample is then backed

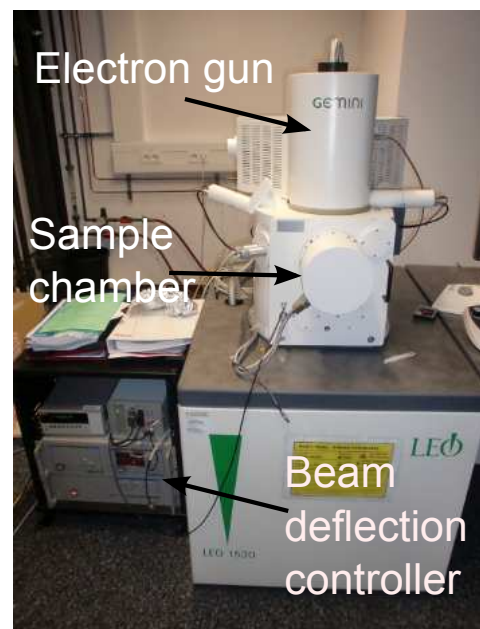


Figure 6.14: The Leo 1530 system used for the e-beam lithography with the beam deflection controllers on the left side.

6. SAMPLE PREPARATION

at 165 ° C for about 30 min to evaporate the rest of solvent and to harden the PMMA layer. The sample is then ready to undergo the e-beam lithography process. The e-beam lithog-

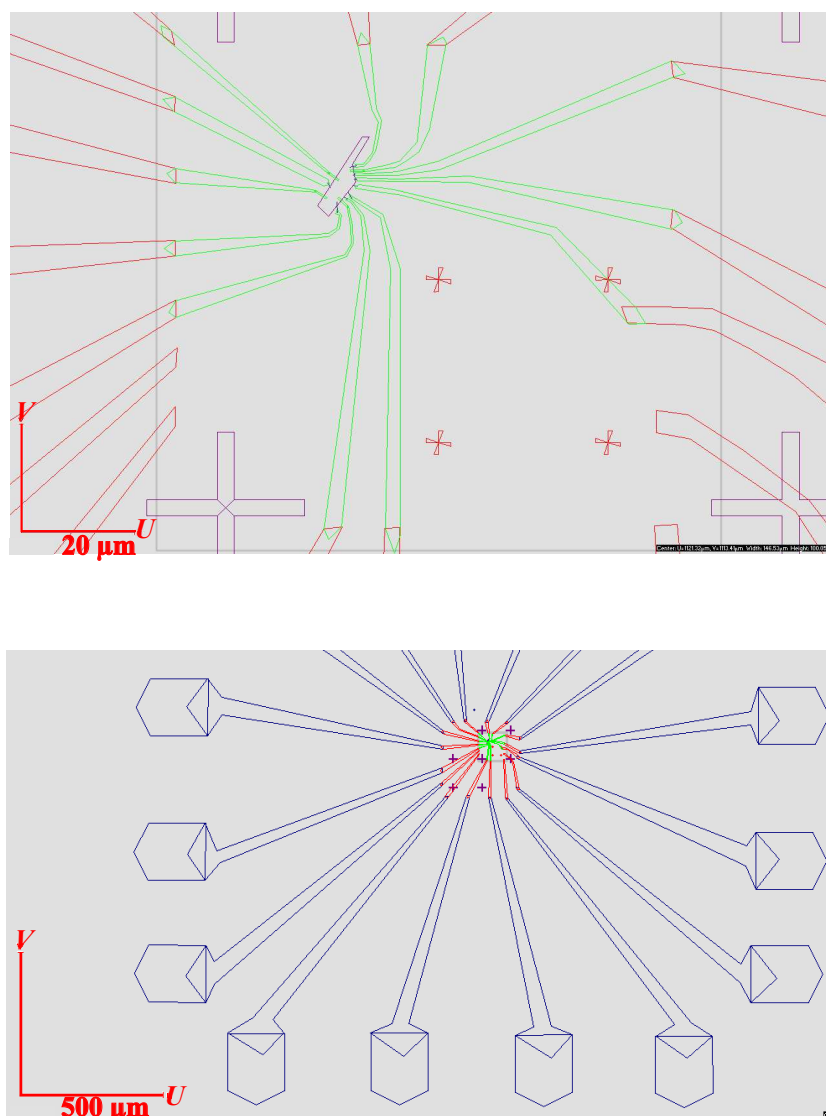


Figure 6.15: Pattern for the e-beam lithography. The design is composed by several layers. The colours of the layers relates to the aperture used to write them: 120 μm diameter aperture for the blue layer (2500×2500μm writing field), 20 μm diameter aperture for the red layer (400×400μm writing field) and 10 μm diameter aperture for the green layer (100×100μm writing field). The purple layer is not written but it is used to represent the structures lying already on the substrates such as the graphene flake to be connected or the alignment markers. Top: Zoom in the graphene region. Bottom: Overall view of the pattern.

raphy was performed with an upgraded Leo 1530 scanning electron microscope (SEM). This lithography system is composed of three main parts: the electron source (or electron gun), the sample chamber and the beam deflection controller (Elphy Plus package). The first two parts are common to all SEM, the third one is the upgrade that turns the SEM into a lithography system. The electron are emitted by a tungsten filament attached to a tip-shaped cathode using the electrical field enhanced thermionic effect (Schottky

emission). The emitted electrons are accelerated in the electron gun by applying an acceleration voltage up to 30kV. A system of electromagnetic lenses along the electron gun makes sure that the beam is focused. The beam current and consequently the diameter of the outgoing e-beam can be changed by switching between several apertures. The sample to be lithographed is clamped to the mechanical stage in the sample chamber and brought under the e-beam.

The areas of the workpiece to be written have been previously drawn in a pattern file using the Elphy software. While generating the pattern file some guidelines have to be followed to ensure an optimal lithography process. The pattern is divided into several layers each one being written using a different aperture (Fig. 6.15). Indeed, each aperture allows a different writing field, which is the biggest area the e-beam can scan on the sample without having to move the mechanical stage. The maximal deflection of the e-beam sets the boundaries of the "writing field". Choosing aperture implies a trade-off between the accuracy and the writing speed, as a big aperture allows to cover a bigger region at some accuracy cost while smaller apertures ensure higher writing precision but in a restrained area. Since moving the mechanical stage, also known as stitching, introduces a shift in the writing and leads to a mismatch between the neighboring writing fields, the position of the mechanical stage is fixed during the lithography of a given layer. A critical step is the alignment of the pattern with the sample. This is done by matching the pattern coordinate system with three alignment markers on the sample. Once the lithography process is completed, the exposed parts are removed to create the mask (Fig. 6.16). The sample is soaked in a solution of methyl isobutyl ketone (MIBK) and isopropanol (proportion 1:3) for about 15 seconds. An optical microscope check follows to determine if resist remains on the exposed areas. Finally the sample is post-baked for about 30 min at 90 ° C to harden the edges of the PMMA mask.

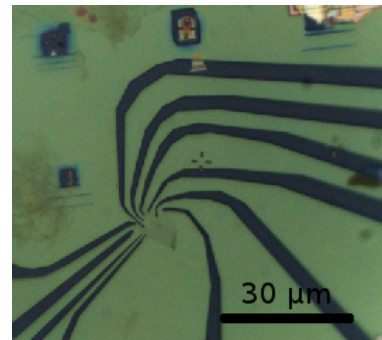


Figure 6.16: Sample after dissolving the e-beam exposed part. The green coloured parts are covered by the PMMA mask. The dark blue ones are left exposed and will be metalized.

6. SAMPLE PREPARATION

6.6 Metal deposition

The metal deposition has been performed using a thermal evaporator (Fig. 6.17), operating in ultra high vacuum (UHV $\sim 10^{-9}$ - 10^{-10} mbar). For each sample, two metals have been used for the contacts. A thin layer of titanium of about 5 to 10 nm thickness followed by a 40 nm thick aluminum layer have been deposited onto the sample. The titanium ensures good adhesion of the aluminum on the sample. To reduce the formation of islands or clusters and therefore obtain a homogeneous layer, the sample is maintained during the deposition at low temperature (~ -130 °C) by a liquid-nitrogen cooling system.

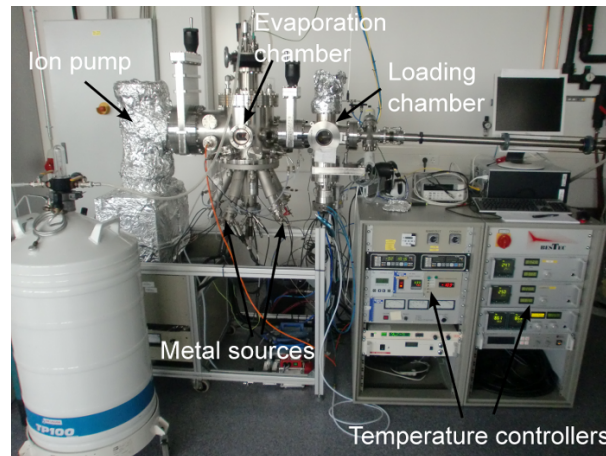
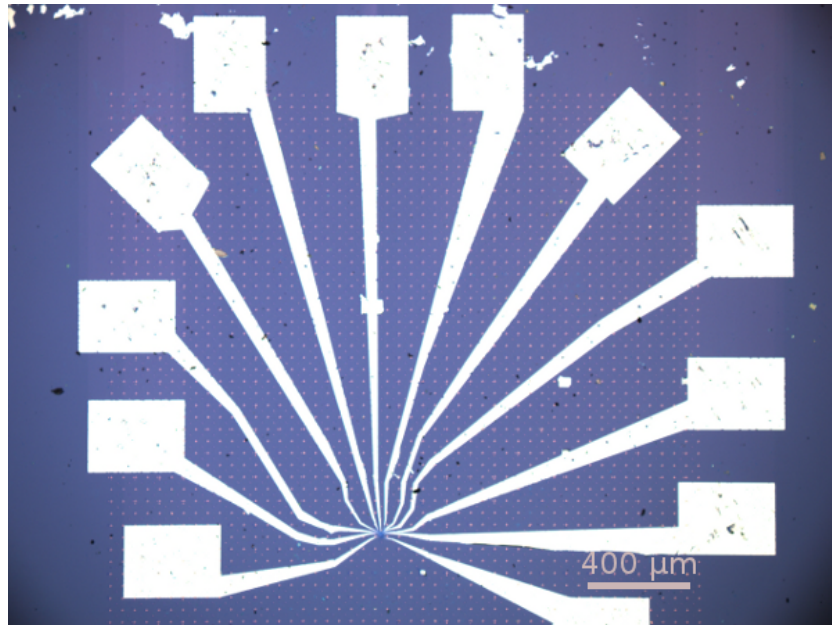
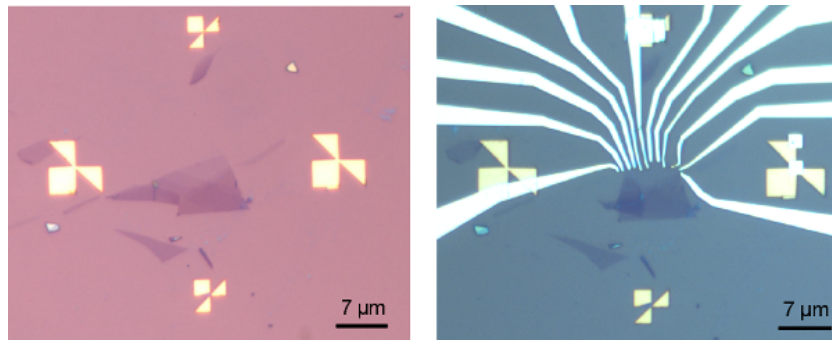


Figure 6.17: UHV thermal evaporator. The sample is loaded into the loading chamber and transferred into the main chamber. An ion pump makes sure that the pressure in the main chamber is around $\sim 10^{-9}$ - 10^{-10} mbar. The sample is rotated to face the metal source whose temperature is set by the controlling board.

Removing the PMMA mask is the last step of the fabrication process. The workpiece is soaked in acetone to dissolve the PMMA and get rid of the extra metal. The sample is then ready to be connected to the probe station for measurements (Fig. 6.18a).



(a) Optical picture of a sample after the metal deposition showing the pads used to connect the samples as well as the metallic leads. The sample is now ready to be probed. The probe station needles will connect the sample on the pads.



(b) Left: Optical microscope picture of a pristine graphene sheet before starting the CNT/graphene fabrication process. Right: The same graphene sheet after the metal deposition. The upper left part of the graphene sheet fold back over itself during the fabrication process.

Figure 6.18: Final step of the sample production.

6. SAMPLE PREPARATION

7

Work function measurements

The charge distribution at the interface of a junction gives the potential landscape that an electron flowing from one structure to another has to cross. Therefore, knowing the charge repartition is the first step to understand the current transport in the junction. One key issue when connecting graphene is the charge transfer due to the connecting metal. The doping due to the metal acts on the transport properties and give rise to a contact resistance at the interface.

As already discussed in Sec. 1.2.1, metals adsorbed onto graphene bind in two different ways depending on whether they preserve the electronic structure of the graphene or not (22, 29). The physisorbed metals bind weakly to the graphene. In that case, the band structure of the graphene underneath and around the metal is not modified significantly. The conic shape around the Dirac point is conserved and the effect of doping due to the metal can be represented by a shift of the graphene Fermi level from the Dirac point. For chemisorbed metals, the doping introduced can not be understood easily since the graphene electronic structure is strongly affected and the conical shape of the bands around the Dirac point is not preserved.

Focusing on physisorbed metals, at the interface, the effective work function of the graphene Φ_{gra}^{eff} (i.e., the work function of the graphene areas influenced by the metal) is given by

$$\Phi_{gra}^{eff} = \Phi_{gra}^0 + \Delta E_F \quad (7.1)$$

where ΔE_F is the shift in the Fermi level and Φ_{gra}^0 is the pristine graphene work function. Despite the lack of band structure calculations for CNT/graphene systems, the MWCNTs can be assumed to belong to the physisorbed type. The main binding interaction for a CNT/graphene system is the weak van der Waals force (see Sec. 2.3.3). Moreover, the equilibrium distance computed for the CNT/graphene in Sec. 2.3 is in the range of that exhibited by the physisorbed metals (see Table 1.1). Measuring the effective work function of MWCNT/graphene junctions and comparing it to the pristine graphene can give a picture of the doping induced in the graphene sheet and therefore an indication of the overall charge transfer. Therefore, several graphene/MWCNT junctions were probed using the Kelvin probe force microscopy technique.

7.1 Kelvin Probe Force Microscopy

The Kelvin probe force microscopy (KPFM) is an AFM technique to measure the work function of a sample (112). A conductive tip scans the sample while the contact potential difference (CPD) is recorded. The CPD is due to the work function difference between the tip (Φ_{tip}) and the sample (Φ_{sample})

$$V_{CPD} = \frac{\Phi_{tip} - \Phi_{sample}}{-e} \quad (7.2)$$

where e is the elementary charge. Provided that the work function of the tip is known by means of a calibration procedure, the work function of the sample can be inferred.

The measurement of the CPD relies on applying an AC voltage plus a DC voltage offset to the tip $V = V_{AC} \sin(\omega t) + V_{DC}$ and then nullifying the oscillating electrostatic forces between the tip and the sample. The aim of the AC voltage is to tell apart the electrostatic forces from other interactions that could affect the tip. The electrostatic forces F_{elec} arise from the Fermi level difference and are given by

$$F_{elec} = -\frac{1}{2} \frac{dC}{dz} \Delta V^2 \quad (7.3)$$

where z and C are respectively the distance and the capacitance between the tip and the sample. This expression is only true for metallic samples, since it is derived from the energy for a parallel-plate capacitor. The potential difference between the tip and the sample ΔV is the sum of the CPD and the applied voltage to the tip

$$\Delta V = V_{AC} \sin(\omega t) + V_{DC} + V_{CPD} \quad (7.4)$$

The electrostatic force F_{elec} is a sum of three spectral terms: a static term, a term depending on the excitation frequency ω and a last one depending on 2ω .

$$F_{elec} = F_{stat} + F_w + F_{2w} \quad (7.5)$$

The static part of the force F_{stat} acts only as a constant off-set on the cantilever bending whereas the F_{2w} contribution does not depend on V_{CPD} . Therefore only F_w is of interest for the KPFM. Since F_w is proportional to $(V_{DC} - V_{CPD})$, by tuning the DC voltage, F_w can be nullified and therefore the CPD can be inferred.

Since the KPFM setup acts also as an AFM while scanning the sample with the tip, not only the electrostatic interaction is measured but also the interactions an AFM can detect. This implies the possibility to separate the topography signal from the KPFM signal. For that, the cantilever is excited with a multi-frequency signal allowing to record in one scan both the topography and the KPFM signal (113, 114). The first eigenmode of the cantilever oscillation ω_0 is used to drive mechanically the cantilever and therefore detect the topography in the IC-mode (see Sec. 6.4). The KPFM signal is detected via the second eigenmode ω_1 . The frequency of the AC signal applied to the tip matches the second eigenmode frequency.

The KPFM or similar electrostatic force microscopy are established techniques to probe graphene samples. Monolayer graphene as well as few-layers graphene exhibit a work function dependence on the thickness (115, 116, 117). This relates to the incomplete charge screening of substrate impurities in thin graphene sheets (118). The work function difference between mono- and bilayer graphene was found to be about 66 meV and reaches the value of the graphite for five-layer graphene. Despite this variation, the work function of graphene remains close to that of graphite. KPFM measurements have been carried together with transport measurements and have evidenced the effect of charge carrier tuning in mono- and bi-layer graphene on the work function (24). The work function could be changed from 4.5 to 4.8 eV for a monolayer while the bilayer samples exhibited a variation range from 4.65 to 4.75 eV. Asymmetry effects between electron and hole transport as well as the impact of impurities left by the fabrication process have also been investigated using KPFM (119, 120).

7.2 Ambient air measurements

The KPFM measurements were performed in ambient conditions with a MultiMode AFM head from Bruker Company and a controller from Nanonis GmbH at the Institute of Microstructure Technology (IMT) together with Zhang Zhenhao. The AFM tip was made of p-doped silicon and was excited with following frequencies: $\omega_0 \sim 70$ kHz and $\omega_1 \sim 430$ kHz.

No tip calibration could be performed to measure its work function Φ_{tip} . Consequently, the extracted work functions have an off-set that can be eliminated by comparing the work function between two regions of the sample.

The measured sample (Fig. 7.1) has been fabricated following the procedure described in the Sec. 6. The contacts were made of a 10 nm-thick titanium layer and a 40 nm-thick aluminium layer. The carrier density in the graphene was fixed during the measurements, since no back voltage could be applied to the sample. Because of the fabrication process and also inferred from the electrical transport measurements, a p-doping can be assumed for the graphene sheet with a high carrier density.

The scanned region is a $7 \times 7 \mu\text{m}$ square encompassing silicon substrate areas as well as parts of the graphene device. Fig. 7.2 shows clearly the different scanned regions. The height signal image presents a good contrast between the graphene, the nanotubes and the metallic leads. Therefore it will be taken as reference for the location of the different structures.

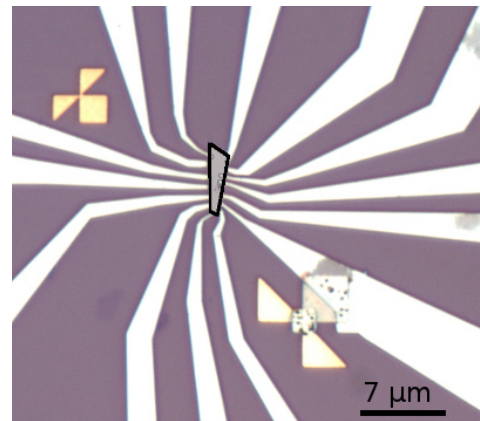


Figure 7.1: Optical picture of the sample used for the KPFM measurements. The contrast of the graphene sheet has been enhanced.

7. WORK FUNCTION MEASUREMENTS

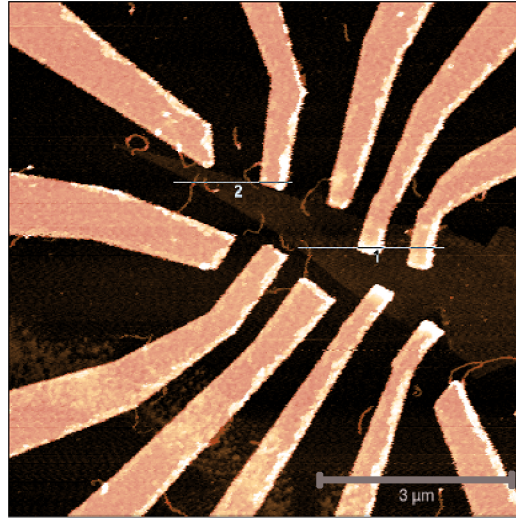


Figure 7.2: AFM IC-Mode height picture of a device showing the metallic leads, the MWCNT and the graphene sheet. The color scale has been modified to enhance the contrast between the graphene, the tubes and the metallic leads.

The V_{CPD} profiles of two regions of the sample have been analyzed. The two profiles of about $2 - 2.2 \mu\text{m}$ length were drawn together along the graphene, the MWCNTs and the metallic leads. The direction of both profiles are shown in Fig. 7.3a. The KPFM signal (Fig. 7.3b) shows, along both profiles, low contrast between the graphene and the MWCNTs and high contrast between the metallic leads and the graphene as well as with the MWCNTs. For both profiles, the height and the V_{CPD} profile are shown on the same plot.

In the "1"-labeled profile (Fig. 7.3c), the nanotube has a diameter of $\sim 14 \text{ nm}$ for a corresponding V_{CPD} signal of about 0.6 V , close to the value of graphene ($\sim 0.57 \text{ V}$). The metallic leads show a much lower V_{CPD} signal: for the first lead between $0.27 - 0.30 \text{ V}$ and for the second one around 0.25 V .

The same trend is clearly to be seen in the "2"-labeled profile (Fig. 7.3d). The profile goes across three nanotubes whose diameters are about $\sim 15 \text{ nm}$. The third nanotube lies half on the graphene and half on the SiO_2 substrate, as can be inferred from the height step between the region before and after the nanotube. All the nanotubes present a V_{CPD} signal ($\sim 0.56 \text{ V}$) indistinguishable from that of graphene V_{CPD} signal. Again, the scan of the metallic leads gives for the V_{CPD} values significantly lower than the ones observed for graphene. The measured V_{CPD} signal values are about 0.25 V , in agreement with the values measured along the "1"-labeled profile for the metallic leads.

From the information given by the two profiles, several conclusions can be drawn. First, except for the graphene areas in the vicinity of a metallic pad, the V_{CPD} signal exhibits a homogeneous value across the rest of the graphene sheet. The work function can be considered constant and no charged or depleted region are evidenced in the sheet. In particular, there is no contrast between graphene regions around the MWCNT and those far away, considered as pristine graphene areas. Consequently, if referred to Eq. 7.1,

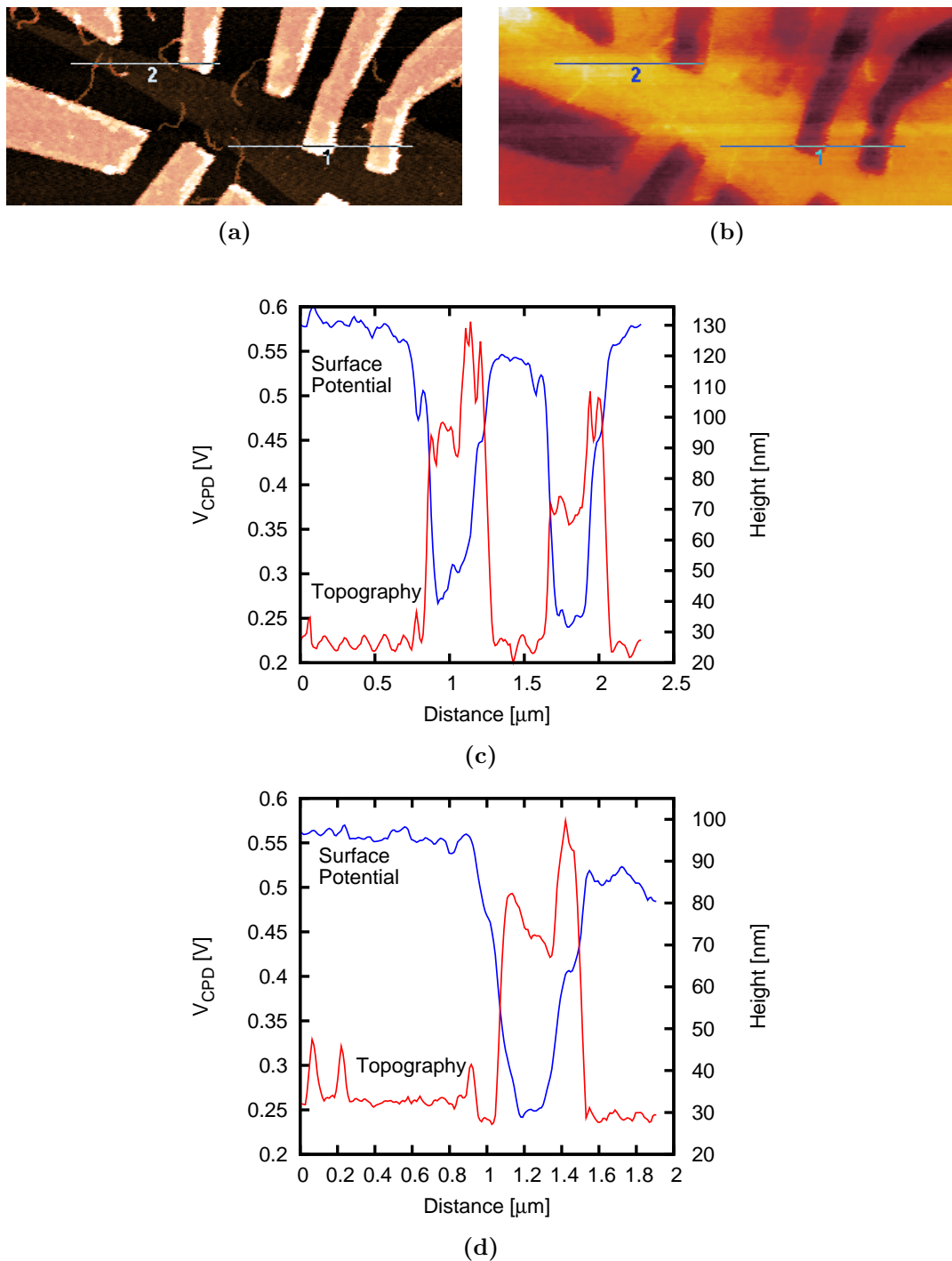


Figure 7.3: 7.3a: AFM IC-mode height picture showing where the two profiles were made. 7.3b: KPFM picture of the same region. Both pictures were recorded simultaneously with the one-scan KPFM technique. 7.3c and 7.3d : Height (red curve) and V_{CPD} signal (blue curve) profiles respectively along the "1"-labeled and the "2"-labeled profiles.

7. WORK FUNCTION MEASUREMENTS

no significant Fermi-level shift and therefore no induced doping can be established in the regions close to the MWCNT. Moreover, the differences of V_{CPD} signal between the MWCNT and the close surrounding graphene areas are of the same magnitude as the instrument noise level ~ 0.02 V. Since the KPFM technique does not give any significant contrast between both regions, the work functions are very similar.

On the contrary, the contrast difference between the metal and the pristine graphene in the KPFM signal is obvious for both profiles. The work function difference is about ~ 0.30 eV. If the literature value is assumed for the pristine graphene work function (i.e., $\Phi_{Graphene}^0 \sim 4.60$ eV), neglecting the effect of p-doping, the inferred work function for the metallic leads is $\Phi_{Metal}^0 \sim 4.30$ eV. This value is indeed close to the work function of aluminium ($\Phi_{Aluminium}^0 = 4.25$ eV). The KPFM is a surface measurement technique, thus the values measured are those of the top layer of aluminium and not those of the bottom layer of titanium.

Focusing on the graphene/metal interface, the variation in the V_{CPD} signal does exhibit a noticeable mismatch with the height signal ones (Fig. 7.4b). The V_{CPD} signal has been averaged along the profile direction over a small region (i.e., the rectangle in Fig. 7.4a). The V_{CPD} signal starts to "feel" the interface around $0.15 \mu\text{m}$ to $0.2 \mu\text{m}$ away from it in the graphene part. Indeed, the V_{CPD} signal starts to decrease significantly for such distance and it drops for a distance of $0.1 \mu\text{m}$ from the interface to a value of 0.52 V. On the other side, in the metal region, V_{CPD} drops quickly over a small distance and reaches a value around ~ 0.26 V. This value does not change significantly over the metal pads except for impurities as already inferred from the analysis of the profiles in Fig. 7.3. As the titanium is chemisorbed on graphene, the doping level ΔE_F can not be deduced from Eq. 7.1. But the fact that the effective work function of the graphene does not match that of pristine graphene over a significant distance away from the contact accounts for an extended doping due to the metal pads.

7.3 Conclusion

Kelvin probe force microscopy measurements have shown that no sizable charge transfer occurs at the interface between MWCNTs and graphene or in the graphene regions around the tube. Metal pads have been on the contrary proven to modify the graphene work function over a large scale, evidencing a significant charge transfer. Since charge carriers injected through the junction move in the energy landscape defined by the charge distribution, the MWCNTs are expected to show low contact resistance when used as connectors for graphene.

The measurements were carried out without tuning the charge carrier density by sweeping the back-gate. A high carrier density with holes as main carriers has been assumed from the statistic of the transport measurements already performed. As observed by Yu *et al.* (24), the work function of graphene exhibit a work function difference of ~ 0.3 eV when changing from a high hole density to a high electron density regime. The work function of the tube should not be significantly modified by the gate sweep, since they are

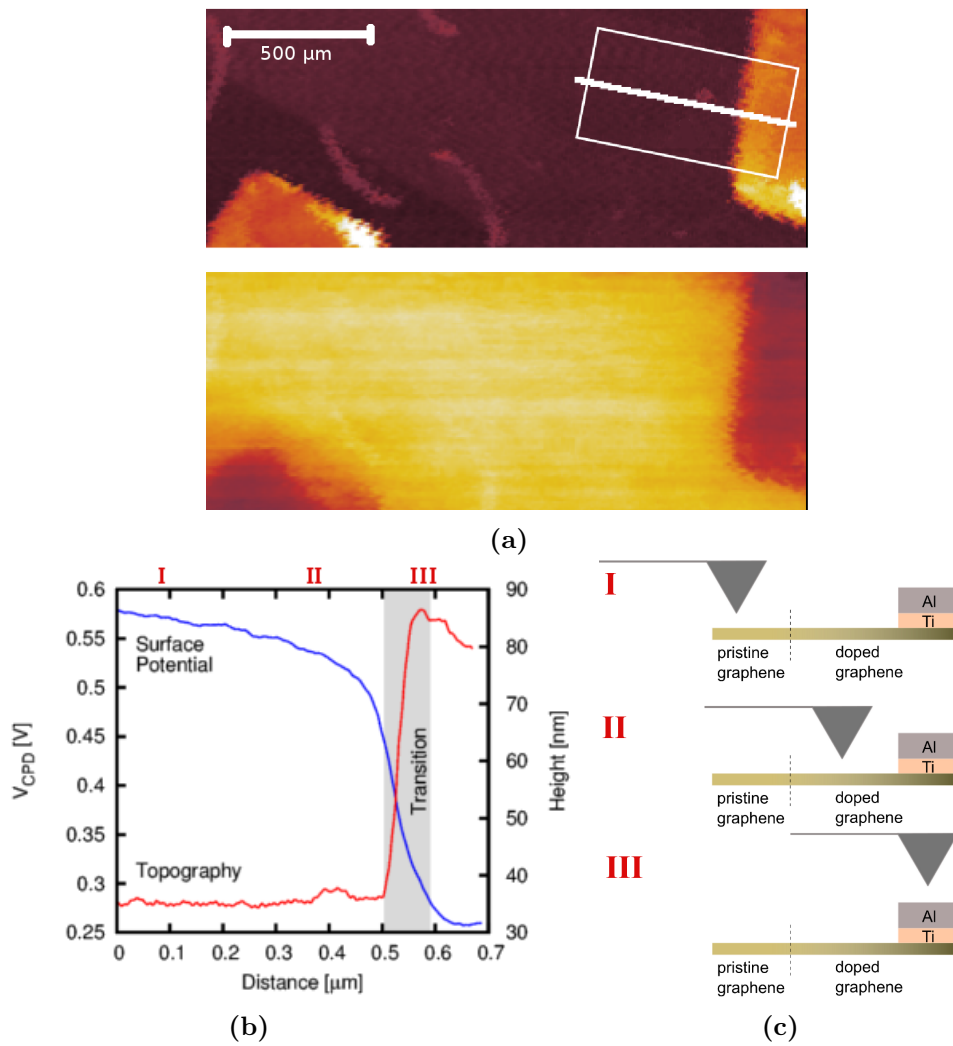


Figure 7.4: Fig. 7.4a: Top: Height picture with the direction of the profile and the region used for the average. Bottom: KPFM picture of the same region. Fig. 7.4b: Height and V_{CPD} signal profiles respectively along the "1"-labeled profile. Fig. 7.4c: Labeled position of the AFM tip while recording the V_{CDV} signal. Position I: measurement of the pristine graphene. Position II: measurement of the doped graphene. Position III: measurement of the aluminium. These positions are indicated in the profiles in Fig. 7.4b.

metallic. Repeating the measurements while sweeping the back-gate could then evidence how strong the coupling is between CNT and graphene.

7. WORK FUNCTION MEASUREMENTS

8

Electrical transport experiments

The electrical characterisation of the MWCNT/graphene junctions fabricated following the process explained in Sec. 6 is presented in this section. Such type of junctions have an unconventional geometry: the contact region is not two dimensional as in standard metal/graphene junctions but quasi-linear. This peculiar feature is expected to influence the transfer of charge carriers across the interface and thus the contact resistance.

The contact resistance arises from the charge transfer that occurs at the junction because of the Fermi level re-alignment as mentioned before in Sec.1.2.1. This picture is valid for an ideal contact. For real contacts, the surface presents defects and is not perfectly flat. The contact resistance is then influenced by the way the interfaces match together and by how many effective "contact points" are formed between the two structures. When the contact surface is two dimensional, statistically enough contact points are present to considered that the matching between the interfaces does not hinder significantly the electrical transport. The injection process is characterised by the transfer length which is basically the length over which the injection process happens. But when it comes to MWCNT/graphene junctions, the electrical transport should be much more influenced by the linear nature of the contact region.

Conventional measurement techniques for the contact resistance includes four-probe measurements, e.g., van der Pauw measurements (121), or transfer length technique (TLM technique) (122). Both techniques require a specific geometry configuration for the sample, which cannot be achieved for the MWCNT/graphene samples because of technical limitations. Indeed, this would require a pre-patterning of the graphene sheet by e-beam lithography. The contamination by the remnants of PMMA would hinder the AFM nanomanipulation process. The contact resistance was therefore determined by two-probe measurements at zero bias using of lock-in detection technique. The two probe measurements consisted in recording the resistance of MWCNT/graphene junction devices while sweeping the gate voltage (i.e., while tuning the charge carrier density in the graphene).

8.1 Measurement setup

All transport measurements were carried out at room temperature and under ambient condition. The samples were connected to the measurement set-up by means of a home-

8. ELECTRICAL TRANSPORT EXPERIMENTS

made probe station. While a small AC excitation voltage is applied between the pair of probed contacts, the current flowing is being measured and recorded. Because of the small amplitude of the signal to be detected, lock-in amplifiers have been used for the measurements.

Lock-in amplifiers rely on a phase sensitive detection technique to retrieve small signals down to the nanovolt in the presence of a noise level that can be orders of magnitude larger. The lock-in generates a DC signal: $A_L \sin(\omega_L t + \theta_L)$. The signal to be detected $A_S \sin(\omega_S t + \theta_S)$ is amplified and multiplied by the lock-in generated signal. The resulting output signal is proportional to $\cos((\omega_L - \omega_S)t + (\theta_L - \theta_S)) - \cos((\omega_L + \omega_S)t + (\theta_L + \theta_S))$. The output is passed through a low-pass filter eliminating the AC component of the signal. The output signal is a DC signal only when $\omega_L = \omega_S$. It is then proportional to $\cos(\theta_L - \theta_S)$. The lock-in frequency is usually taken as the same as the excitation signal used for the measurements, thus assuring the condition $\omega_L = \omega_S$.

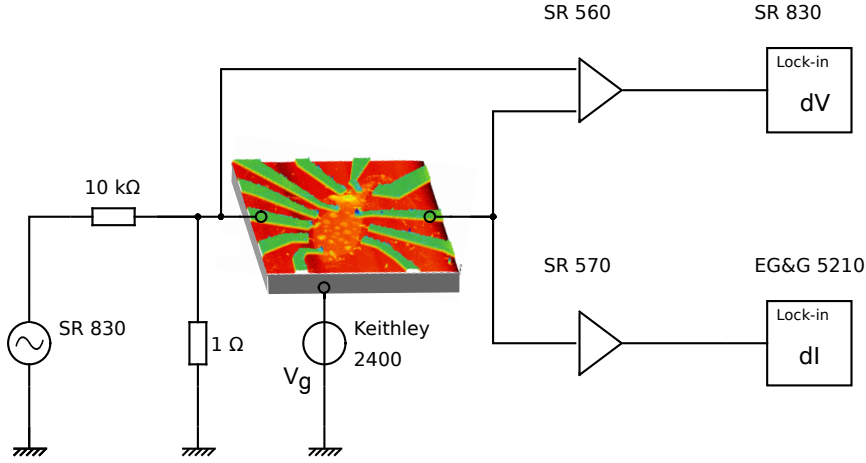


Figure 8.1: Electric schematic of the measurement set-up. Two metallic leads (green colour on the AFM picture) are connected to the measurement set-up. The back-gate voltage is applied to the silicon substrate (grey colour).

The Fig. 8.1 gives the electrical diagram of the measurement set-up. The sample lies on a copper plate connected to a source meter (Keithley 2400 Source Meter) that is used for applying the back-gate voltage. The low frequency ($\sim 15 - 35\text{Hz}$) excitation signal is delivered by a Stanford Research Systems (SR) 830 DSP lock-in ($\sim 5\text{V}$), a voltage divider follows to reduce the excitation voltage to a safe range for the sample ($\sim 0.5\text{ mV}$). This assures that the measurements are carried at (almost) zero bias. The current flowing through the pair of contacts is detected after amplification and conversion into a voltage (low-noise current amplifier SR 570) by a EG&G 5210 lock-in. The voltage drop across the contacts is measured after amplification (low-noise amplifier SR 560) by the SR 830 DSP lock-in. The differential resistance dV/dI is measured by using the lock-in technique. Since the measurements are performed at low bias, the differential resistance is equal to the resistance.

8.2 Sample description

Each sample fabricated had typically between 6 to 10 graphene/MWCNT and 4 graphene/metal junctions integrated in it. Three sorts of devices have been probed:

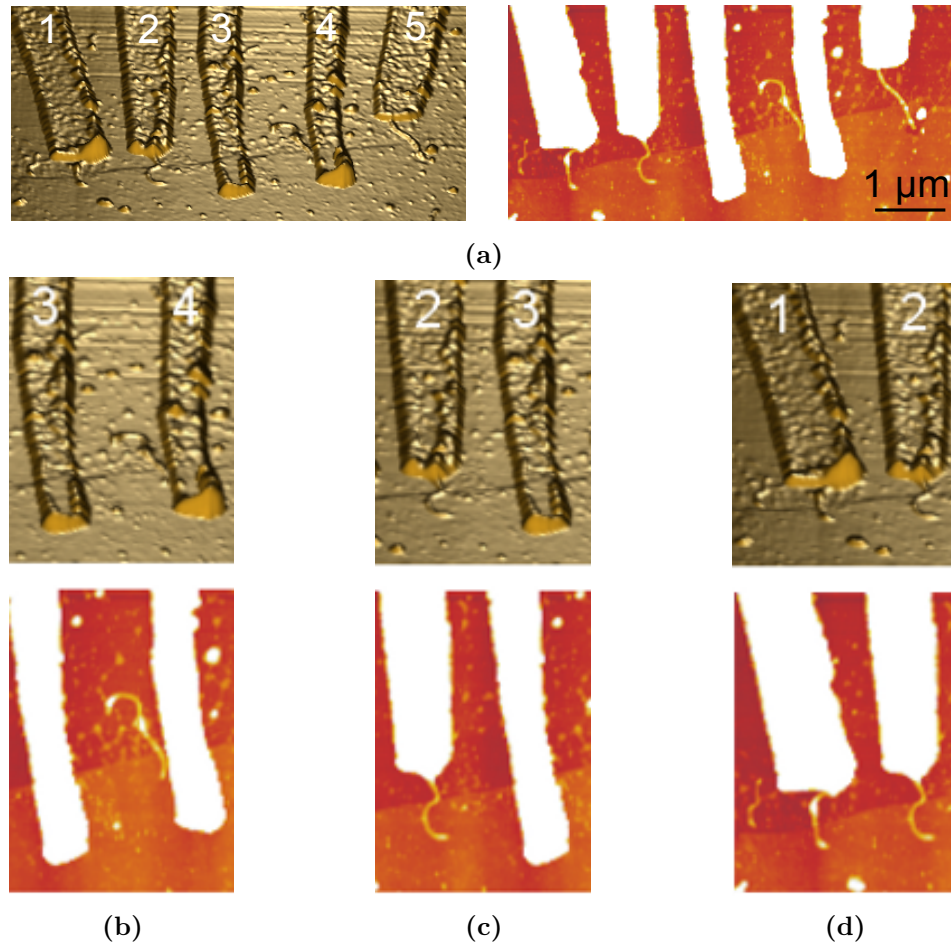


Figure 8.2: AFM pictures of the 3 devices layouts used for the scope of this work. Fig. 8.2a: Overall view of a sample on which MWCNT as well as metal probes are lying on a graphene sheet. Left: 3D picture. Contacts 1, 2 and 5 are MWCNT. Contacts 3 and 4 are metal. Right: 2D picture of the same sample with the scale indicated. Fig.8.2b: Example of metal-graphene-metal device (MGM) Fig. 8.2c: Example of CNT-graphene-metal device (CntGM) Fig. 8.2d: Example of CNT-graphene-CNT device (CntGCnt)

- metal-graphene-metal devices (MGM) which are standard two terminal metal probes with two metal/graphene junctions (Fig. 8.2b)
- CNT-graphene-metal device (CNT-GM) which integrates one MWCNT/graphene junction and one metal/graphene junction (Fig. 8.2c)
- CNT-graphene-CNT device (CntGCnt) which integrates two MWCNT/graphene junction in which both electrodes are MWCNTs (Fig. 8.2c)

8.3 Description of the measurements

A classical way to characterise graphene devices is to study how external electric potentials modify the charge carrier transport in the device. For that, the so-called resistance versus gate measurements are performed. The graphene is separated from the highly doped silicon wafer by a layer of silicon oxide. The system forms a capacitor with the top plate being the graphene sheet, the bottom one being the highly doped silicon and the silicon oxide constitutes the dielectric medium. By applying a voltage to the highly doped silicon V_g , a potential difference is created across the silicon oxide and the charge carrier density in the graphene sheet can be tuned.

As already mentioned in Sec. 1.1.3, since the charge carrier density is directly related to the density of states (DOS) and to the Fermi level in the graphene sheet, the Fermi level position can be controlled by the back-gate voltage V_g . The direction of the shift allows to control the carriers involved in the transport. For $V_g < V_{Dirac}$, the Fermi level is in the valence band, being the holes the main carriers. While for $V_g > V_{Dirac}$, the Fermi level is in the conduction band and the electrons are then involved in the transport.

For graphene with a Dirac point at V_{Dirac} , the charge density reads

$$n = \alpha(V_g - V_{Dirac}) \text{ with } \alpha = \frac{\epsilon_0 \epsilon_r}{te} \quad (8.1)$$

where ϵ_0 is the vacuum permittivity, ϵ_r is the relative permittivity of SiO_2 , t is the thickness of SiO_2 layer and e is the elementary charge. For all the experiments a SiO_2 thickness layer of 300 nm has been used, thus giving a value $\alpha = 7.19 \times 10^{10} \text{cm}^{-2} \cdot \text{V}^{-1}$. Because of the p-doping exhibited by almost all samples, the Dirac point was reached for positives V_g . The intrinsic doping level ranged from almost zero for $V_{Dirac} \gtrsim 0$ V to more than $n \sim -4.67 \times 10^{12} \text{cm}^{-2}$ ($V_{Dirac} \sim 65$ V) for strongly doped samples. This implies a wide range of charge carrier density, thus allowing to analyse the transport for three different carrier regimes: the high-density carrier regime with holes or electrons as main carriers, and the low-carrier regime near the Dirac point.

8.3.1 Connecting graphene with metal

The measurements of metal-graphene-metal (MGM) devices yield a range for the resistance of the graphene and the metal/graphene junction. They also give a characterisation of the graphene sheet in terms of intrinsic doping.

The MGM device can be viewed as series of resistors with some of them showing a gate dependency. The total resistance R_{MGM} is the sum of the lead resistances R_{Met} , the metal/graphene interface resistance $R_{Met/Gra}$ and the graphene channel resistance R_{Gra}

$$R_{MGM} = 2.R_{Met} + 2.R_{Met/Gra} + R_{Gra} \quad (8.2)$$

The metal leads are assumed to have the same contact quality and therefore no distinction is made between them. From all the contributions, the lead resistance does not depend on the gate voltage and introduces a small offset in the total resistance. It

can be assumed that this contribution is negligible. The expression 8.2 reduces then to $R_{MGM} \simeq 2.R_{Met/Gra} + R_{Gra}$.

The graphene resistance is expected to depend on the charge carrier density n . As for the metal/graphene contact resistance, as mentioned in Sec.1.2.1, it is still unclear whether it shows a dependence on n .

An example of resistance versus gate measurement for a MGM device is given in Fig.8.3. For all the resistance versus gate measurements performed, two curves have been obtained depending on the gate sweep direction. The Dirac point is shifted but the overall behaviour of the resistance remains unchanged. This hysteresis effect observed upon reversal of the gate sweep direction is a known effect occurring at room temperature. It is due to the screening of the gate voltage by charged impurities of adsorbate molecules (123, 124). In the rest of the work, for the sake of comparison, only the downward sweep direction has been considered (i.e: gate voltage sweep direction: from the maximum to the minimum).

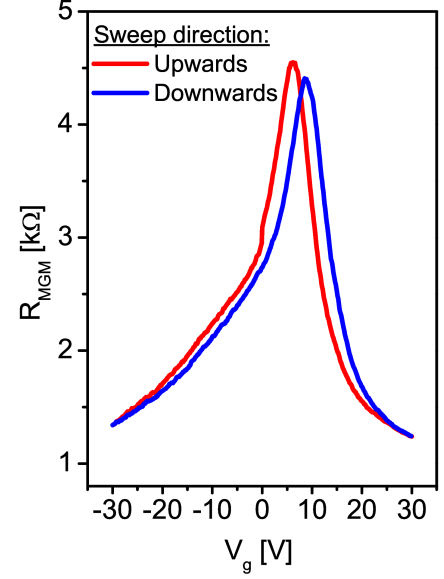


Figure 8.3: Resistance-versus-gate curve. The red (blue) curve has been recorded for increasing (decreasing) gate voltage sweep.

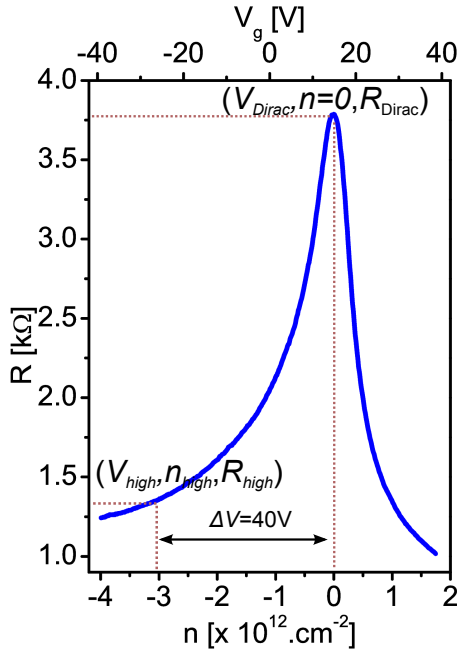


Figure 8.4: Resistance-versus-gate curve. The charge carrier density is shown on the x-axis. The Dirac point has been represented as well as the point in the p-branch labeled by $(V_{high}, n_{high}, R_{high})$.

the metal and the graphene are different. The resistance depends on the geometry of the

The maximum of resistance displayed by the curve in Fig. 8.4 signals the position of the Dirac point reached for a gate voltage of V_{Dirac} , the charge carrier density n is zero at this point. The resistance exhibits some asymmetry between the p-doped and the n-doped branches, indicating that the electrons and the holes have a different field effect mobility. All samples presented a level of intrinsic p-doping, as the Dirac point is always reached at positive voltages.

For the analysis of the high-density carrier regime, we focus on the hole governed transport since more data are measured than for the electron governed part. A point has been taken as reference 40V away from the Dirac point in the p-branch of the resistance-versus-gate curve $V_{high} = V_{Dirac} - 40$ V. This point has a charge carrier density n_{high} and a resistance R_{high} .

For each MGM device, the shape of the graphene channel and the contact surface between the metal and the graphene are different. The resistance depends on the geometry of the

8. ELECTRICAL TRANSPORT EXPERIMENTS

device. The measurements of R_{MGM} give therefore only an overall indication of how resistive the graphene and the interface metal/graphene are, but comparison of different samples is not possible. From Fig. 8.5, the most of the resistance values are around a few $k\Omega$ except for three more resistive samples that show values up to some tens of $k\Omega$.

In order to characterise the magnitude of the change in the resistance induced by the gate voltage sweep (i.e., the gate effect), ΔR has been defined by

$$\Delta R = R_{Dirac} - R_{high}. \quad (8.3)$$

From the R_{MGM} data in Fig. 8.5, ΔR is only a few $k\Omega$ with a maximum of about 15 $k\Omega$ for the two samples showing the highest resistance. These two samples can be considered as having poor quality contact between the graphene sheet and the metal.

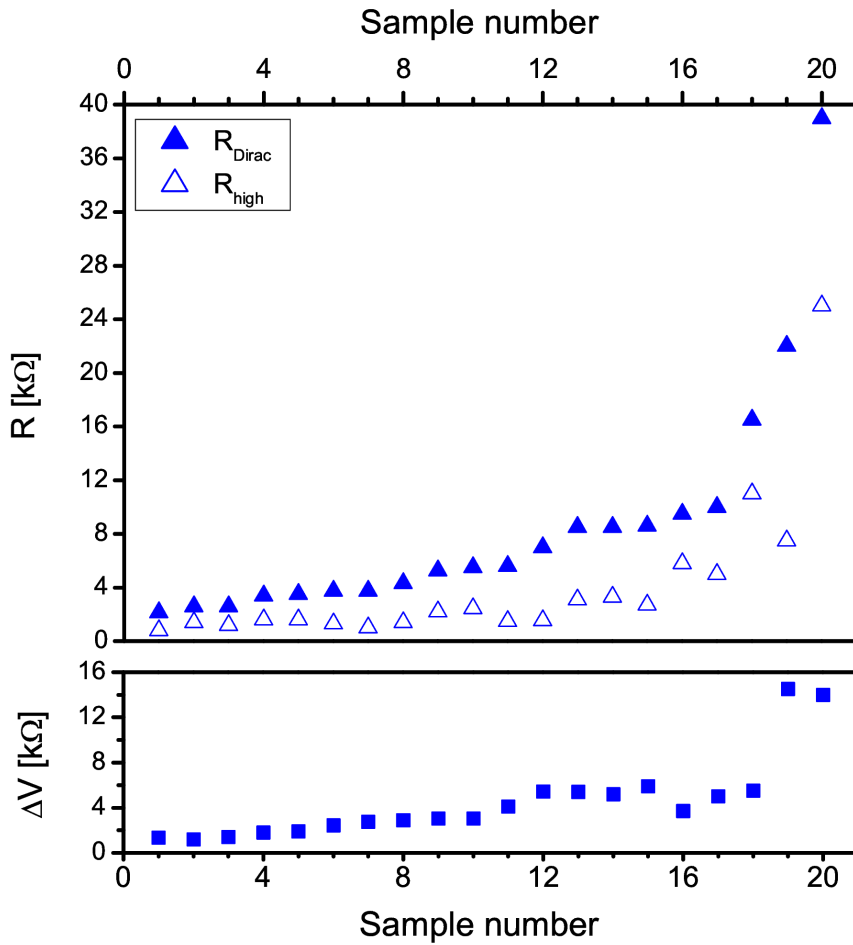


Figure 8.5: Top: Distribution of the MGM Devices with respect to measured resistances at the Dirac point and 40 V away from it in the p-doped region. The full dots correspond to the resistance at the Dirac point V_{Dirac} , while the open dots correspond to the resistance for V_{high} . The data has been sorted ascendantly using V_{Dirac} . Thus the sample number is not related to the chronological order of sample fabrication. Bottom: Distribution of the MGM Devices with respect to ΔR .

8.3.2 Connecting graphene with MWCNTs

MWCNT-Graphene-Metal devices

As the MGM devices, the CNT-GM devices are series of resistors. This time the total resistance R_{CNT-GM} is given by

$$R_{CNT-GM} = 2.R_{Met} + R_{Met/Gra} + R_{Gra} + R_{CNT/Gra} + R_{CNT} + R_{CNT/Met}. \quad (8.4)$$

R_{CNT-GM} includes in addition to the resistances already described for the MGM devices, the resistance of the interface MWCNT/graphene $R_{CNT/Gra}$, the resistance of the MWCNT R_{CNT} and the resistance of the interface MWCNT/metal $R_{CNT/Met}$. In the Eq. 8.4, $R_{Gra} + R_{Met/Gra}$ depends on the charge carrier density n and $R_{CNT/Gra}$ would be proven to depend on this parameter as well. $R_{CNT} + R_{CNT/Met}$ is gate-independent since the tubes are metallic.

Measurements have been carried out for 32 CNT-GM devices. They display a resistance range significantly larger than the MGM devices (Fig. 8.6). The least resistive samples exhibit a resistance around ~ 40 k Ω while the most resistive sample had a maximal resistance over 1.4 M Ω . ΔR shows a wide range of values varying by two orders of magnitude from around 10 k Ω to 1 M Ω .

Several terms in Eq. 8.4 can be estimated. First, the literature gives for the resistance of MWCNT and the contact resistance between MWCNT and metal a range from a few k Ω to some tens of k Ω (125, 126, 127, 128, 129).

The resistance range exhibited by the MGM devices gives an estimate for $R_{Met/Gra} + R_{Gra}$. R_{MGM} contains twice the contact resistance $R_{Met/Gra}$. By taking half of the values for R_{MGM} , the $R_{Met/Gra} + R_{Gra}$ term is only a few k Ω , when not considering two most resistive samples.

It follows from these estimates, that three groups of samples can be identified depending on the neglected contribution in the total resistance expression R_{CNT-GM} :

- Low-resistance samples ($R_{Dirac} \lesssim 80$ k Ω - 100 k Ω). For these samples, Eq. 8.4 holds since the two terms $R_{Met/Gra} + R_{Gra}$ and $R_{CNT} + R_{CNT/Met}$ cannot be neglected. The charge carrier density dependent part is then $R_{Met/Gra} + R_{Gra} + R_{CNT/Gra}$.
- Medium-resistance samples (100 k $\Omega \lesssim R_{Dirac} \lesssim 250$ k Ω). The contribution of the graphene and the metal/graphene interface can be safely neglected. Thus Eq. 8.4 reduces to $R_{CNT-GM} \simeq R_{CNT/Gra} + R_{CNT} + R_{CNT/Met}$. The charge carrier density dependent part is this time only the contact resistance between the tube and the graphene $R_{CNT/Gra}$.
- High-resistance samples ($R_{Dirac} > 400$ k Ω) The MWCNT contribution to the total resistance can be neglected for this group. Thus the measured resistance is the MWCNT/graphene interfacial resistance $R_{CNT/Gra}$.

The resistance versus gate curves display an interesting trend. In Fig. 8.7, the gate effect is small for the low-resistance sample $\Delta R = R_{Dirac} - R_{high} \sim 8$ k Ω while it is about

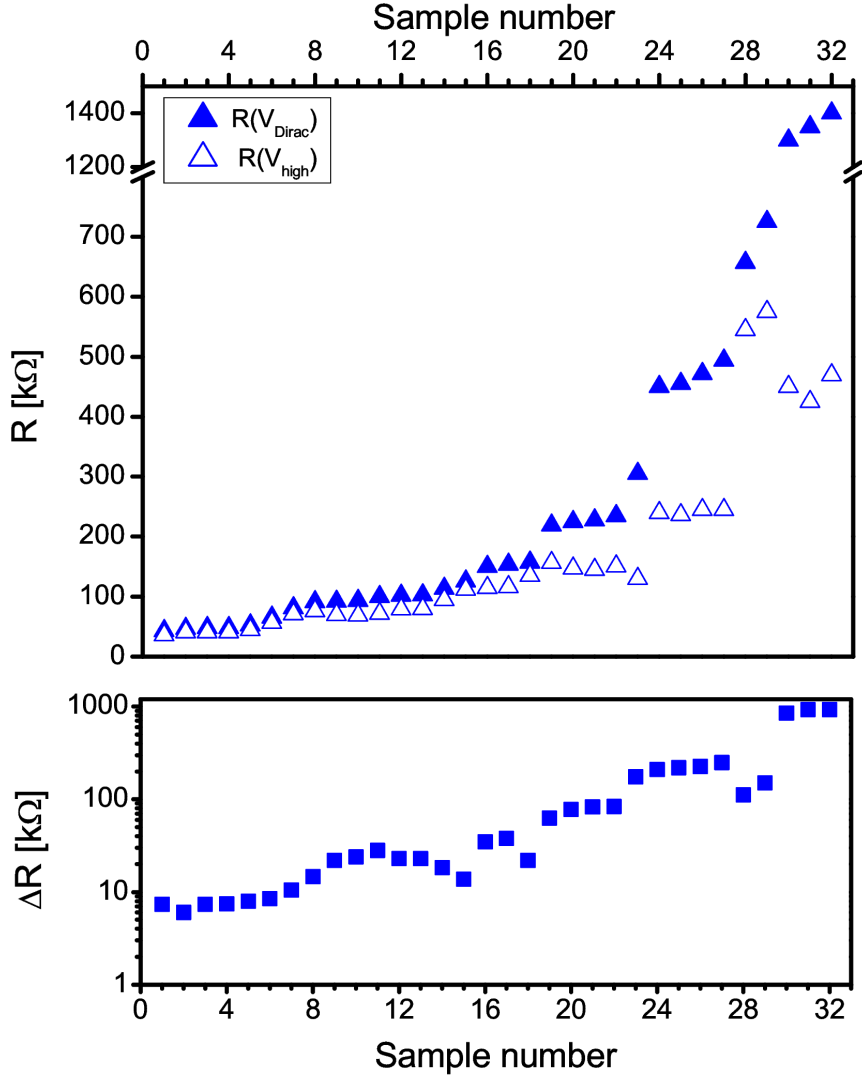


Figure 8.6: Repartition for the CNT-GM devices of the resistances measured at the Dirac point and 40V away from it in the p-doped region. The full dots correspond to the resistance at the Dirac point V_{Dirac} , while the hollow dots correspond to the resistance for V_{high} . The data has been sorted ascendantly using R_{Dirac} . Thus the x-axis sample number is not related to the chronological order of sample fabrication. Bottom: Repartition of ΔR for the corresponding CNT-GM devices.

an order of magnitude higher ($\Delta R \sim 70k\Omega$) for the medium-resistance sample and almost two orders of magnitude higher for the high-resistance sample ($\Delta R \sim 900k\Omega$).

This trend is clearly confirmed when ΔR is represented versus the resistance at the Dirac point as in Fig. 8.8. For low-resistance samples, the modulation of the resistance with the charge carrier density is weak, ΔR is a few $k\Omega$. Such value for ΔR are close to the values observed for the MGM devices. The junction can be considered to be an additional resistor weakly dependent on the charge carrier density that only shifts the curve obtained for the graphene connected to metal to a higher value of the resistance.

Since the range of the gate effect in graphene is around a few $k\Omega$ as seen previously, the gate effect observed in graphene cannot account for the one observed for medium- to

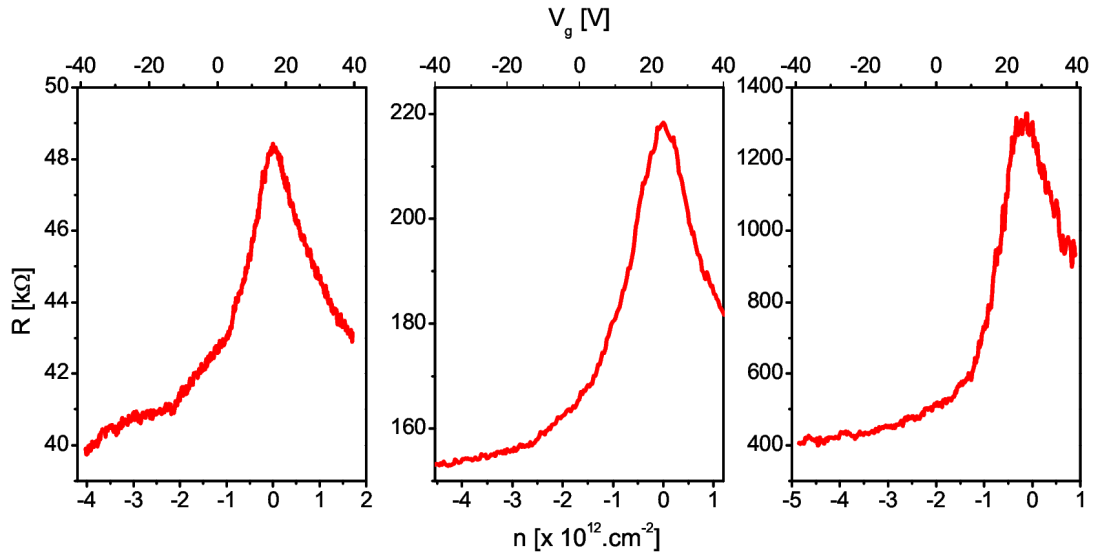


Figure 8.7: Resistance versus gate curves for three different types of CNT-MG devices: a low resistance sample (left), a medium resistance sample (middle) and a high resistance sample (right).

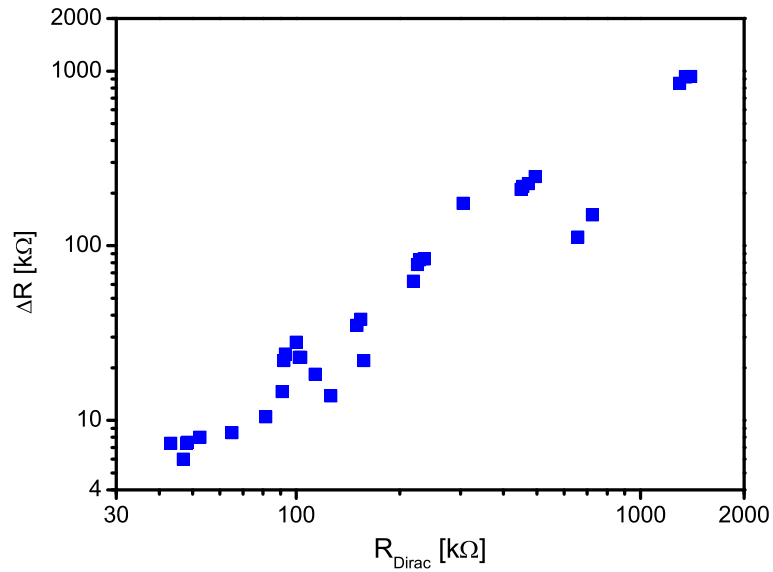


Figure 8.8: ΔR versus R_{Dirac} for the CNT-GM devices

high-resistance samples. The modulation of the resistance with the charge carrier density in graphene is directly related to the density of states of graphene. As a consequence, a different mechanism is needed to be invoked to explain the gate voltage effect observed in medium- to high-resistance samples.

8. ELECTRICAL TRANSPORT EXPERIMENTS

MWCNT-Graphene-MWCNT Junctions

The same transport measurements as for the CNT-GM have been carried for 13 CNT-G-CNT devices. These devices are also series of resistors with some showing a charge carrier density dependence. As for the CNT-GM devices, the total resistance $R_{CNT-G-CNT}$ contains the metal leads R_{Met} , which will be neglected as for the CNT-GM and MGM devices and the graphene channel R_{gra} contributions. For the CNT-G-CNT devices, both electrodes are made up of CNTs, no graphene/metal interface contribution has to be considered. The total resistance $R_{CNT-G-CNT}$ is then given by

$$R_{CNT-G-CNT} = R_{CNT/Met,1} + R_{CNT,1} + R_{CNT/Gra,1} + R_{Gra} + R_{CNT/Gra,2} + R_{CNT,2} + R_{CNT/Met,2} \quad (8.5)$$

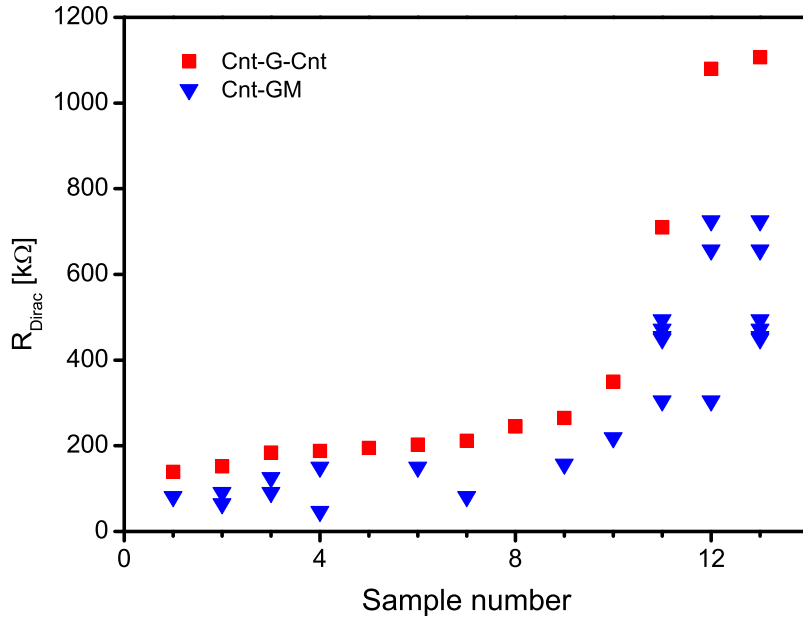


Figure 8.9: Repartition of the resistance $R_{CNT-G-CNT}$ measured at the Dirac point for the measured CNT-G-CNT devices. The data has been sorted ascendantly using R_{Dirac} . Thus the x-axis sample number is not related to the chronological order of fabrication. The

The previous section evidenced that the resistance of the tubes presents a wide range of variation. Therefore, the two tubes are not assumed to be similar.

Fig. 8.9 makes evident that as expected from Eq. 8.5, $R_{CNT-G-CNT}$ is the sum of the contributions of the two tubes/graphene junctions integrated in the device. Indeed, this trend is clearly seen if the resistance of one MWCNT/graphene junction $R_{CNT-G-M}$ integrated in the CNT-G-v device is represented along with the total resistance of the CNT-G-CNT device $R_{CNT-G-CNT}$. In addition, Fig. 8.9 gives the range of $R_{CNT-G-CNT}$ values that vary from around 150 kΩ to more than 1 MΩ. Considering the resistance grouping of the single MWCNT/graphene junctions discussed in the previous section, the lower limit range of $R_{CNT-G-CNT}$ accounts for CNT-G-CNT devices made of two low-resistance

MWCNT/graphene junctions. The association of two high-resistance MWCNT/graphene junctions yields the upper limit for $R_{CNT-G-CNT}$. The MWCNT/graphene contact resistance was proven in the last section to exhibit a gate dependence. The resistance versus gate measurements of CNT-G-CNT devices do consequently show the same behaviour (Fig.8.10). But these measurements display also more noise than the CNT-GM measurements. This observation is easily understood by the fact that the noise is due to the integrated MWCNT/graphene junctions in the device.

Finally, the same trend as in the previous section with respect to the gate effect is also clearly evidenced in Fig. 8.11. The gate effect increases with the resistance of the device. Indeed, samples characterised by low resistance (i.e., R_{Dirac} less than 400 k Ω) exhibit low ΔR , while high resistive samples (i.e., R_{Dirac} above 700 k Ω) shows a difference ΔR around 400 k Ω .

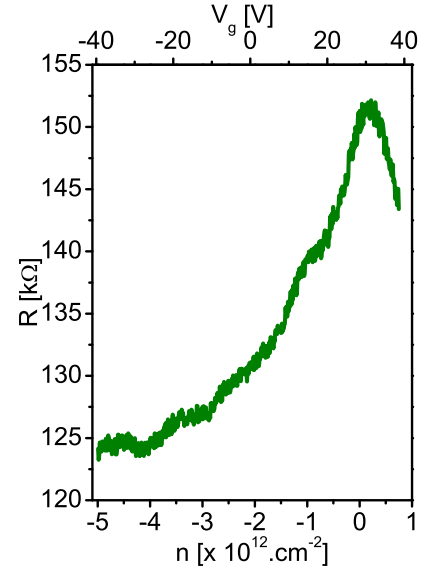


Figure 8.10: Resistance versus gate $R(V_g)$ measurement for CNT-graphene-CNT devices (CNT-G-CNT).

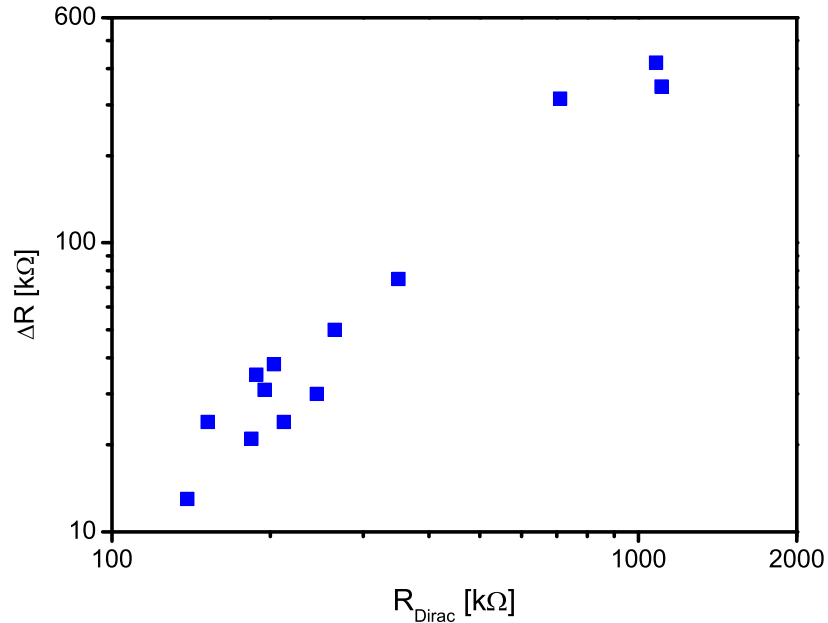


Figure 8.11: ΔR versus R_{Dirac} for the CNT-M-CNT devices

Summary

The following trends have been revealed by the measurements:

8. ELECTRICAL TRANSPORT EXPERIMENTS

- The more resistive the junction is, the higher the resistance gate modulation.
- Low-resistance junctions show a slight gate dependence of the resistance. The resistance of the CNT-GM devices is mainly the resistance of the graphene and the graphene/metal contacts shifted by the value of the MWCNT/graphene junction resistance.
- Medium- to high-resistance junctions exhibit a moderate to high gate resistance modulation, which cannot be attributed to the graphene channel. The gate dependence effect relies on a different mechanism than the one prevalent in graphene. For CNT-GM devices integrating such junction, the total resistance is mainly the MWCNT/graphene interfacial resistance (plus a small contribution of the CNT resistance for the medium resistance samples).

8.4 MWCNT/graphene junction properties

From the study presented by Khomyakov *et al.* (22) (See Sec. 1.2.1), the electrons flowing across the junctions have to overcome a potential barrier arising from the work-function mismatch and the chemical interaction. The transfer process taking place at the junction governs the junction properties. Therefore, the measurements presented in the previous section will be analysed in this section to characterise this process. It is assumed that the charge carrier transport from the tube into the graphene is equivalent to the reverse transport direction. Thus only the transport from the tube to the graphene has been considered for the analysis.

8.4.1 Charge injection localisation

The description of the charge injection mechanism is essential to understand the performances of the probed devices. The injection process is the tunneling process that allows the charge carriers to be transferred from the tube to the graphene underneath the tube. This process is one of the two processes that account for the contact resistance as explained by Xia *et al.* (See Sec.1.2.1). Determining where in the junction the injection occurs sets the limits for the device scaling and therefore presents a great interest for potential device integration in applications.

Two mechanisms for the charge injection have been reported for metal contacts to CNTs or to graphene. Some studies claimed that the charge injection occurs at the edges of the contact region (38, 130, 131, 132, 133). Other works suggested that the charges are injected in the part of the nanostructure underneath the electrode, the contact is said to be distributed (134, 135, 136, 137, 138). Such type of injection process is characterised by a transfer length defined by the distance over which the charges are transferred from one structure to the other. When the contact length is smaller than the transfer length, the charge transport is hindered. This is reflected in an steep increase of the contact resistance for devices with contact length below the transfer length. For CNT/metal contacts, transfer lengths of about 100 nm have been reported (137) whereas

for graphene/titanium contacts transfer lengths down to 200 nm have been extracted (138).

In addition to the lack of consistency of the previously mentioned results, it is worth pointing out that these results were obtained for side-contact configuration and in the case of the CNTs for embedded contacts. The probed MWCNT/graphene junctions are side-contact junctions but not an embedded type since the graphene does not wrap the tube. Thus the contact area differs from the reported junctions and is reduced to a line in the case of an ideal junction.

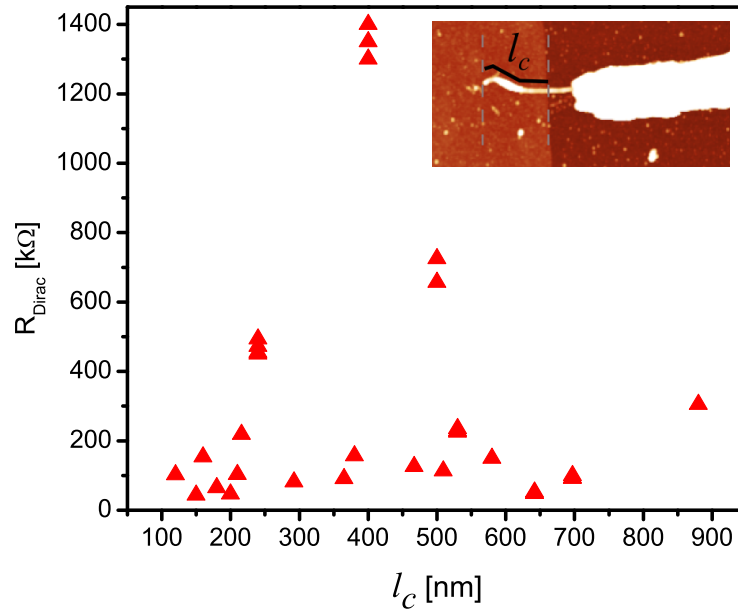


Figure 8.12: Resistance at the Dirac point R_{Dirac} versus the contact length l_c . Inset: Contact length measured using an AFM picture.

This implies that the contact length between the tube and the graphene constitutes the key parameter to analyse the MWCNT/graphene junction. The contact length l_c is defined by the length of the tube lying on top of the graphene sheet. The resistance of the CNT-GM devices at the Dirac point has been used for the analysis. Considering the resistance at high carrier density would have yielded the same trends. The extraction from the AFM measurements gives a range from about 100 nm to 900 nm for the contact length.

The results presented in Fig. 8.12 display no obvious dependence of the resistance on the contact length. No increase of the resistance for short contact length is evidenced, implying that from a device integration point of view, 100-nm long junctions make already good contact. Since the transfer length gives the limit for the device scaling, when considering its value for CNT/metal and for graphene/metal contacts, MWCNT/graphene junctions show better downsizing potential.

8. ELECTRICAL TRANSPORT EXPERIMENTS

Now focusing on the place the charge injection occurs, as already mentioned, the injection mechanisms found in the literature are based on embedded side contacts and are therefore not relevant to explain the charge injection in the MWCNT/graphene junctions. Since the contact is quasi-linear and because of the tunneling nature of the charge injection, it can be safely assumed that the distance between the tube and the graphene plays a crucial role in determining where the charge are injected. Indeed, the tube-to-graphene charge injection is likely to occur at the closest point between the two structures. Charge accumulation at the end of the tube has been demonstrated in Sec. 4.7 suggesting that this point can be identified with the injection point. Nevertheless, if deformations of the structures due to structural properties or defects are considered, the injection point could be located away from the tube end.

8.4.2 Gate dependence of the injection

The MWCNT/graphene junctions displayed a wide range of resistance as well as values of the gate effect. The gate dependent part of the resistance in the CNT-GM devices was proven to be related directly to the MWCNT/graphene contact resistance for medium- to high-resistance samples. For the low-resistance samples, the gate effect is mainly due to the graphene, but with a small contribution from the MWCNT/graphene contact resistance.

The mechanism described by Xia *et al.* to render the contact resistance for metal/graphene junctions (27) has been used as a point of departure to analyse the measurements obtained for MWCNT/graphene junctions. As mentioned in Sec. 1.2.1, the contact resistance is described by two transmission processes, each characterised by a transmission coefficient: the injection of carriers from the metal to the metal-covered graphene (transmission coefficient: T_{MG}) and the transport from the injection point to the pure graphene channel (transmission coefficient: T_K).

Injection from the M-graphene to pure graphene

As discussed in Sec. 1.2.1, the electronic structure of the metal-covered graphene and around the metal is modified (referred as M-graphene). In the case of physisorbed metal, the Fermi level is shifted from the Dirac point while for chemisorbed metals the band structure is strongly affected. This leads to a charge accumulation (depletion) in the M-graphene. The charge carriers flowing from the M-graphene to the pure graphene need to overcome the potential barrier due to the charge redistribution in the M-graphene region. Up to some hundreds of nanometers have been reported for the width of the extension of the M-graphene region. (139, 140, 141). The transmission coefficient T_K accounts for such transport.

In the case of MWCNT/graphene junctions, the equivalent of the M-graphene area is the area influenced by the tube in the graphene sheet. This region has a limited extent, around 1.7 to 2 CNT radius for big tubes according to the charge distribution calculations (See Sec.5.1). The transmission coefficient T_K can be therefore considered as fixed for all the MWCNT/graphene junctions, implying that the electrical transport from the

tube-influenced graphene area to the graphene is not relevant to explain the high contact resistance and strong gate effects exhibit by some samples.

An additional argument is provided by the KPFM work-function measurements of Sec. 7. No change in the work function has been evidenced around the MWCNT/graphene junction. The charge transfer if any was proven to be limited. Thus the potential barrier the charge carriers have to cross when flowing from the graphene underneath the MWCNT to the "pristine" graphene region, is small and spatially confined. The junction is therefore not governed by the transport process from the tube-influenced graphene area to the graphene.

Injection from the MWCNT to the M-graphene

Since the transmission process between the tube-influenced graphene area and the pristine graphene has been ruled out to explain the resistance range and the gate effect observed for the MWCNT/graphene junction samples, the transmission process between the MWCNT and the graphene appears to be the governing process for the transport. For the metal-to-graphene injection, considering a coherent diffusive regime, Xia *et al.* give the following formula for the transmission coefficient T_{MG}

$$T_{MG} = \sqrt{\frac{\lambda}{\lambda_m}} \quad (8.6)$$

where λ is the scattering mean free path in the M-graphene. The length λ_m is the metal-graphene coupling length and is inversely related to the coupling strength term η that renders the re-hybridisation strength between the d-orbitals of the metal and the graphene p_z orbital. Fermi's golden rule can be used to obtain an expression for η yielding a quadratic dependence on the hopping integral between the metal and the carbon atoms t_{MG} , which accounts for the inter-system carrier transmission: $\eta \propto |t_{MG}|^2$ (27). Metal binding strongly with the graphene shows a higher coupling strength ($\eta=0.3$ eV for titanium) than weakly binded metal ($\eta=0.06$ eV for palladium) (135). The coupling strength η is expected to decrease with the increasing distance between the metal and the graphene, implying the very same behaviour for the transmission coefficient T_{MG} . Indeed, as mentioned in (22, 29), the chemical interaction that accounts for the repulsive interaction between the metal and graphene orbitals depends strongly on the distance between the structures, being strong when the structures are close and negligible when the structures are distant from more than a threshold distance ($\gtrsim 4.2$ Å for copper contacts on graphene (29)).

In the case of MWCNT/graphene junctions, no band structure calculations have been reported up to now. The interaction between the p_z orbitals of the two systems can be assumed to be weak since it is mostly due to the van der Waals interaction. Still, since the hopping integral between the carbon of the tube and the carbon of the graphene can be defined t_{CNT-G} , the coupling strength coefficient η is obtained as in the previous metal-graphene interaction case by Fermi's golden rule. The transmission coefficient is then expected to decrease with increasing MWCNT-graphene distance.

8. ELECTRICAL TRANSPORT EXPERIMENTS

The equilibrium distance has been computed in Sec. 2.3.4 for an ideal MWCNT/graphene junction d_{eq} . This distance corresponds to the position where the chemical repulsive forces are balanced by the attractive electrostatic forces. The calculations do not take into account the randomness of the contact due to impurities, defects in the structures or corrugations in the graphene sheet that can modify significantly the effective distance between the two structures. In the case of a real MWCNT/graphene contact, the effective distance d_{eff} is the distance between the MWCNT and the graphene at the charge injection point from one structure to another as pictured in Fig.8.13.

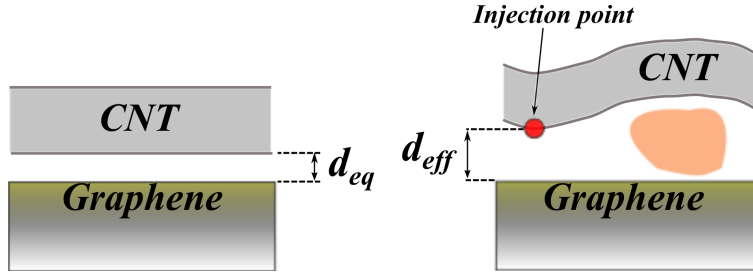


Figure 8.13: Distance between the tube and the graphene for an ideal junction (left) and for a real junction (right). In the picture, the effective distance d_{eff} departs from the ideal equilibrium distance d_{eq} due to an impurity trapped between CNT and graphene.

The trend indicated by the MWCNT/graphene junction resistance measurements can be related to the effective distance d_{eff} between MWCNT and graphene and to the changes induced by the electrostatic forces on this distance. As the gate voltage is swept, the charge carrier density in the graphene sheet is tuned. In the MWCNT, mirror charges are created to screen the electric field due to the charges in the graphene sheet. Because of the attractive electrostatic interaction between the charges in the graphene and in the MWCNT, the distance d_{eff} changes and therefore the transmission coefficient T_{CNT-G} with it. This leads finally to the observed variation of the junction contact resistance with the gate voltage. Around the Dirac point, the charge carrier density in the graphene sheet is low, thus the electrostatic interaction with the tube is reduced. The effective distance d_{eff} is then maximum and so is the contact resistance. With the increase of the charge carrier density in the graphene sheet, the electrostatic interaction with the tube grows and eventually the effective distance d_{eff} shortens allowing a better transmission.

Thus the range of values obtained for the MWCNT/graphene junction resistance can be related to the effective distance between the MWCNT and the graphene d_{eff} . Indeed, MWCNT/graphene junctions with large effective distance exhibit low transmission coefficient and therefore high contact resistance. If on the other hand the distance d_{eff} decreases, the tube-to-graphene transmission probability increases, resulting in a reduced contact resistance.

The variation of d_{eff} with the gate sweep drives the variation in the junction resistance. The value of the effective distance at the Dirac point d_{max} is crucial to determine the range of d_{eff} and therefore the amplitude of the resistance gate modulation. For values of d_{max} close to the theoretical value, the effective distance between the MWCNT and

the graphene cannot be reduced significantly by the electrostatic forces since quickly the repulsive forces due to atomic orbital overlap prevail as pictured in the representation of the binding energy in Fig. 8.14. For values of d_{max} substantially larger than the theoretical value, the range of variation is larger for the distance d_{eff} as seen in the binding energy in Fig. 8.15.

All these assumptions lead to understand the MWCNT/graphene junction as follows:

- Low-resistance MWCNT/graphene junctions have few structural defects or impurities. They exhibit an effective distance at the Dirac point d_{max} (pink position in Fig. 8.14) close to the theoretical value. With the gate sweep, the effective distance does not change significantly (green position in Fig. 8.14) because of the quickly rising repulsive forces. Thus, the transmission coefficient is not substantially affected. The resistance consequently does not show a strong modulation. The chart in Fig. 8.14 gives an overview of the resistance modulation phenomena for low resistance MWCNT/graphene.
- Medium- to high-resistance MWCNT/graphene junctions have a higher effective distance at the Dirac point. This leads to a higher resistance range than for the low-resistance MWCNT/graphene junctions. The distance d_{eff} changes significantly when the graphene charge density is tuned. Consequently, the transmission coefficient is strongly affected. This is reflected by the medium to strong modulation effect observed for the junction resistance. Fig. 8.15 gives an overview of the resistance modulation phenomena for high-resistance MWCNT/graphene.

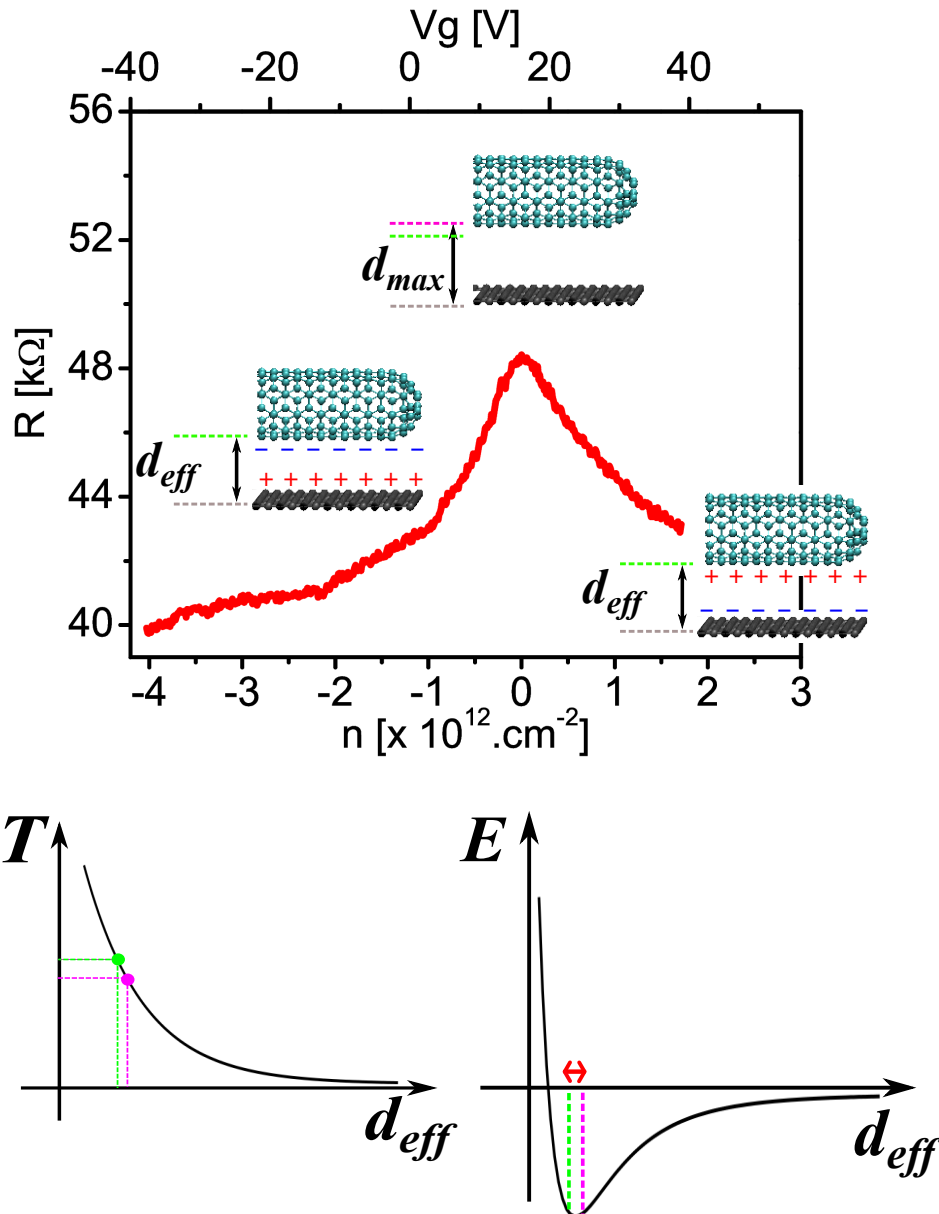


Figure 8.14: Gate dependence mechanism for low resistance samples. The effective distance is indicated on the resistance versus gate curve for the high charge carrier density (green position) and for the Dirac point (pink position). The binding energy E between the tube and the graphene as well as the tunneling transmission coefficient T at the junction (assumed to have an exponential decay shape) are shown versus the effective distance d_{eff} . The two positions corresponding to the high charge carrier density and the Dirac point are displayed in each chart.

The small range of d_{eff} variation evidenced between the pink and the green position (red arrow) is due to the quick uprising repulsive forces. The change in the transmission coefficient is small between these two positions and therefore has little influence over the resistance.

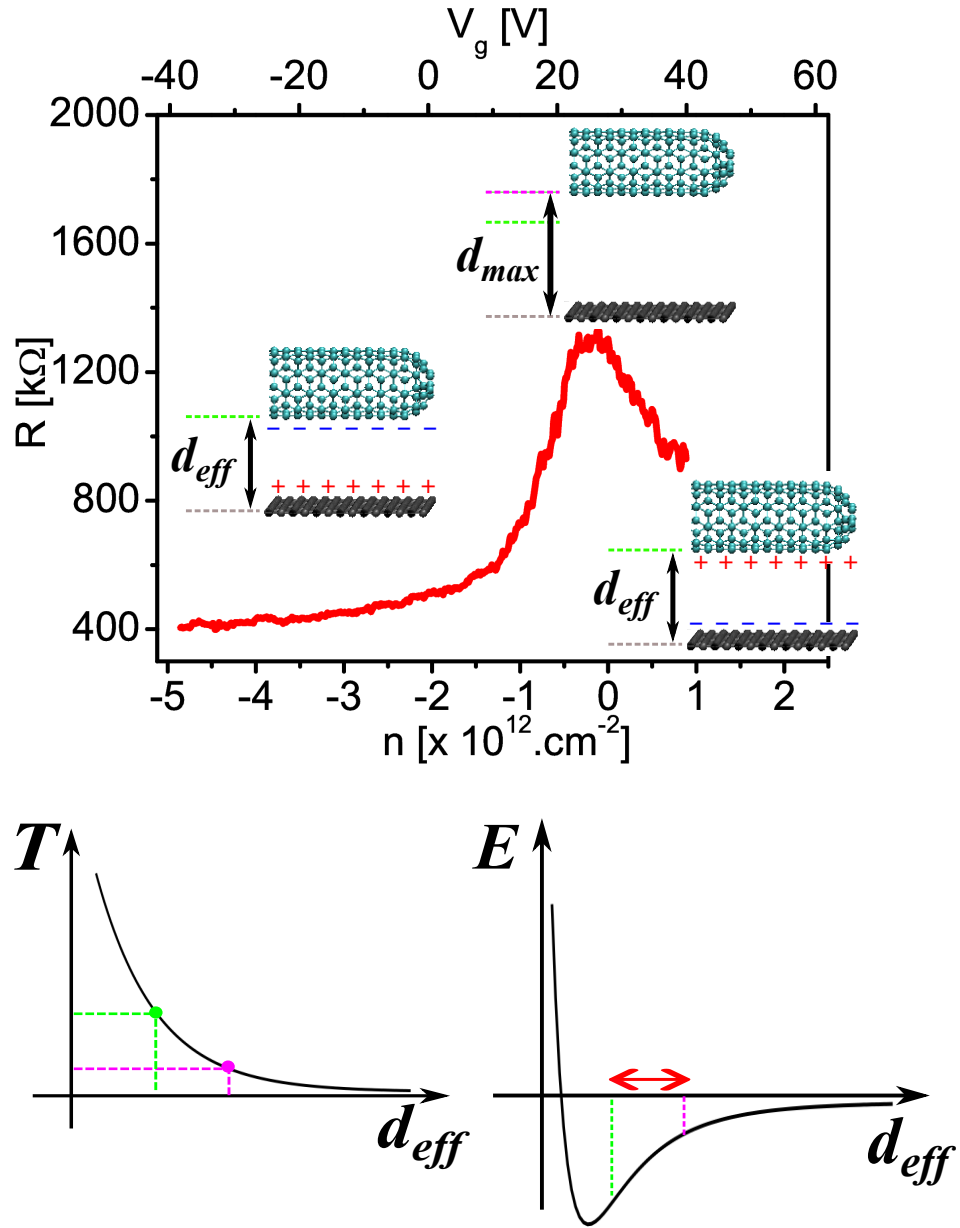


Figure 8.15: Gate dependence mechanism for high resistance samples. The effective distance is indicated on the resistance versus gate curve for the high charge carrier density (green position) and for the Dirac point (pink position). The binding energy E between the tube and the graphene as well as the tunneling transmission coefficient T at the junction (assumed to have an exponential decay shape) are shown versus the effective distance d_{eff} . The two positions corresponding to the high charge carrier density and the Dirac point are displayed in each chart.

The large range of d_{eff} variation evidenced between the pink and the green position (red arrow) is due to the electrostatic forces arising when the graphene sheet is being charged. The change in the transmission coefficient is significant between these two positions. The resistance undergoes consequently a dramatical modulation.

8.5 Conclusion

Electrical transport measurements on MWCNT/graphene junctions were carried out for several devices. The measurements yielded a wide range of junction resistances, from a few tens of $k\Omega$ to around $1.5 M\Omega$. The contact length of the junction down to 100 nm was found not to influence the quality of the transport. This result could be used for further applications to downsize devices. The measurements showed furthermore that the junction resistance depends on the gate voltage. A correlation between the resistance of the junction and the exhibited gate effect was clearly revealed. The transport at the junction can be understood by a chain process involving first the transfer from the tube to the graphene underneath the tube followed by a second transport process to the pure graphene region.

The first transfer process was proven to govern the junction transport properties. The correlation trend between resistance and gate effect had been explained by the nature of the contact surface, which is a quasi 1D contact area. A slight modification over the contact area represented by a change in the effective distance between the two structures has a dramatic influence over the transport properties at the junction since the effective distance is related to the transmission coefficient. Low-resistance junctions have few structural defects and impurities in contrast to medium- to high-resistive samples. This is reflected by a smaller effective distance and therefore small resistance value and reduced resistance modulation with the gate voltage sweep.

Thus controlling the transport at the junction depends strongly on the experimental condition. Impurities due to sample fabrication and structural defects influence the quality of the junction. Surfactant molecules or residual scotch tape are key parameters to control in order to improve the quality of the junction and obtain more predictable results.

Conclusion

New connecting techniques for graphene have to be developed to ensure a better device integration for this astonishing material. The use of carbon nanotubes, a material closely related to graphene as connecting material is a promising option to explore. In this work, the interface between carbon nanotube and graphene has been addressed. A range of properties have been determined ranging from structural parameters to electrical transport behaviour.

First the structural properties of carbon nanotube/graphene junctions have been computed using semi-empirical quantum chemistry methods. The van der Waals interaction plays a key role in the binding between the two graphitic structures. The binding energy as well as the equilibrium distance have been determined. Both exhibited a dependence on the carbon nanotube radius: the more atoms participates in the binding, the stronger the binding becomes and the further apart the substructures are. The equilibrium distances ranging from 3.02 Å for small-radius tube to 3.14 Å for large-radius tubes are significantly smaller than the graphite interplane distance.

The equilibrium distance was used as an input parameter to calculate the charge distribution at the carbon nanotube/graphene interface. First two-dimensional analytical calculations have been performed. By means of conformal mapping technique the Laplace equation could be solved, giving the charge distribution. A three-dimensional electrostatic-based model called "charge-dipole" model that scales down to the atoms has been used to gain more insight. The results yielded a limited spatial extent of the charge redistribution around the junction region in the graphene sheet. When compared to usual metals that dope the graphene over a scale of hundreds of nanometers scale, the influence of the nanotube on the charge distribution in graphene is confined to 1.7 to 2 times the tube radius.

Contrary to all reported fabrication techniques, the process developed in this work to build nanotube/graphene junctions allows to preselect the type of tube and to control the location of the junction. This achievement relies on using the tip of an atomic force microscope as a "nano rake" to drag off the tubes onto the graphene. Multi-walled carbon nanotubes (MWCNT) have been used as building block for the junctions because of their metallic properties and their resistance to mechanical manipulations.

Kelvin probe force microscopy were performed to measure the work function of the graphene at and around MWCNT/graphene junctions and Ti/Al/graphene junctions. No significant charge transfer could be evidenced at the interface between MWCNTs and graphene nor in the graphene regions around the tube. Connecting graphene with

8. ELECTRICAL TRANSPORT EXPERIMENTS

MWCNT therefore does not introduce doping in the graphene sheet. On the contrary, KPFM measurements displayed a substantial work function modification over a large scale deep in the graphene sheet due to the charge transfer between the metal and the graphene.

Electrical transport measurements were carried out on the fabricated MWCNT/graphene junctions. The measured resistance ranged from a few tens of $k\Omega$ to around $1.5 M\Omega$. A high downsizing potential was evidenced for the MWCNT/graphene junctions, since the junction resistance exhibits no variation with the contact length down to 100 nm. An interesting trend was revealed by the results: the higher the junction resistance, the stronger the modulation of the resistance with the charge carrier density (i.e., the gate effect). The transfer process between the tube and the graphene underneath was found to govern the junction resistance. It depends on the effective distance between the MWCNT and the graphene. Junctions showing few structural defects or/and low contamination are likely to exhibit a small effective distance and thus a low interfacial resistance while junction having higher effective distance are much more resistive. This is a step toward the control over the electrical transport at MWCNT/graphene junctions.

The use of MWCNT as connector for graphene in electronic devices is limited then by performances strongly dependent on the experimental conditions and on the quality of the building-blocks. Reducing the amount of impurities due to the fabrication process could be a way to assure low-resistance MWCNT/graphene junctions suitable for the electronic applications such as transparent electrodes or all-carbon electronics.

Appendix A

Hartree-Fock method

A.1 Schrödinger equation

Quantum effects play an important role for the understanding of nanoscopic and mesoscopic systems. When the system is at equilibrium and without time-dependent perturbation, the time-independent Schrödinger equation is enough to describe the system. Solving the time-independent Schrödinger consists of determining the Eigenstates and their associated Eigenvalue for the Hamiltonian of the system. Finding all the Eigenstates for a system is a daunting task and is dispensable since the system in the further developments is considered not to be in an excited state but in its ground state. The ground state is defined by being the state with lowest energy. All the calculations carried in this section will refer to the ground state.

The Schrödinger equation reads

$$\mathbf{H}\Psi = E\Psi \quad (\text{A.1})$$

where \mathbf{H} is the Hamiltonian operator, Ψ the wave function and E the system energy. In a matrix algebra picture, E and Ψ are respectively Eigenvalue and Eigenvector (or Eigenstate) of the Hamiltonian operator \mathbf{H} . Providing an accurate expression for \mathbf{H} is the starting point for determining the system. The operator \mathbf{H} contains five contributions to the total energy of the system and its expression is given by

$$\mathbf{H} = -\sum_A \frac{\hbar^2}{2m_A} \nabla_A^2 + \sum_{A<B} \frac{e^2 Z_A Z_B}{r_{A,B}} - \sum_i \frac{\hbar^2}{2m_e} \nabla_i^2 + \sum_{i<j} \frac{e^2}{r_{i,j}} - \sum_i \sum_A \frac{e^2 Z_A}{r_{i,A}} \quad (\text{A.2})$$

where A denotes the nuclei, i denotes the electrons, m is the mass, e is the elementary charge, Z is the atomic number and r is the distance between the considered particles. The first two terms in Eq. A.2 account respectively for the nuclei kinetic energy and the potential energy, the third and fourth term account for both the electronic kinetic energy and the potential energy whereas the last term contains the electron-nucleus Coulomb interaction.

Since the proton to electron mass ratio is about 1836, electrons move faster than nuclei and react instantaneously to a change in the nuclei position. Consequently, the electrons are considered to be moving in a frozen nuclei lattice. Thus when dealing with

A. HARTREE-FOCK METHOD

the motions of the electrons, the nuclei positions are then fixed. The nuclei kinetic energy can be then neglected and the nuclei potential energy set as constant, which will be omitted in the following developments since it only shifts the energy eigenvalues and leaves the wave functions invariant. In this approximation, known as the Born-Oppenheimer approximation, the Hamiltonian can be written

$$\mathbf{H}_{el} = - \sum_i \frac{\hbar^2}{2m_e} \nabla_i^2 + \sum_{i<j} \frac{e^2}{r_{i,j}} - \sum_i \sum_A \frac{e^2 Z_A}{r_{i,A}} \quad (\text{A.3})$$

and the general Schroedinger equation (Eq. A.1) reduces to the electronic Schroedinger equation

$$\mathbf{H}_{el} \Psi(\mathbf{r}) = E_{el} \Psi(\mathbf{r}) \quad (\text{A.4})$$

with \mathbf{r} the electronic coordinate vector and E_{el} the electronic energy. Using the one-electron operator $\mathbf{h}(i)$ for the electron i defined as

$$\mathbf{h}(i) = -\frac{1}{2} \nabla_i^2 - \sum_A \frac{Z_A}{r_{i,A}} \quad (\text{A.5})$$

and the two-electrons operator $\mathbf{v}(i, j)$

$$\mathbf{v}(i, j) = \frac{1}{r_{i,j}} \quad (\text{A.6})$$

equation A.3 can be written as (using atomic units: $m_e = 1$, $\hbar = 1$ and $e=1$)

$$\mathbf{H}_{el} = \sum_i \mathbf{h}(i) + \sum_{i<j} \mathbf{v}(i, j). \quad (\text{A.7})$$

A.2 Hartree-Fock method

Having decoupled the electronic motion from the nuclear one by calling on the Born-Oppenheimer approximation, the resolution of Eq. A.4 remains rife with problems as it can be only solved exactly for one-electron systems such as H , H_2^+ or He^+ . The electron-electron interaction term hinders an exact resolution of the Schroedinger equation for larger systems. Handling larger systems requires then to rely on numerical methods.

In this scope the Hartree-Fock method was developed (142). This method relies on an iterative process for determining the wave function and the associated energy. Instead of considering the electron-electron interaction pairwise, the method introduces a mean field term for the electron-electron interaction. Each electron moves into a field induced by the other electrons and the value of this field depends only on the coordinates of the considered electron, the positions of the other electrons is thus not required.

The second assumption made by the Hartree-Fock method concerns the total wave function Ψ used as initial guess to start the iterative process. For the initial guess, Ψ is required to be antisymmetric and to be a product of one-electron wave functions χ , called molecular spin orbitals (MSO). The MSO are a product of spatial wave function times a

spin wave function. They are chosen to constitute a set of orthonormal functions

$$\langle \chi_i | \chi_j \rangle = \int \bar{\chi}_i(\mathbf{x}) \chi_j(\mathbf{x}) d\mathbf{x} = \delta_{i,j} \quad (\text{A.8})$$

Ψ is written for a system of N electrons as a Slater determinant

$$\Psi = \frac{1}{\sqrt{N!}} \begin{vmatrix} \chi_1(1) & \chi_2(1) & \cdots & \chi_N(1) \\ \chi_1(2) & \chi_2(2) & \cdots & \chi_N(2) \\ \vdots & \vdots & \ddots & \vdots \\ \chi_1(N) & \chi_2(N) & \cdots & \chi_N(N) \end{vmatrix} \quad (\text{A.9})$$

The Hartree-Fock equations are now derived by first computing the energy of a so defined total wave function Ψ . The expectation value of the electronic Hamiltonian (Eq. A.7) gives the Hartree-Fock energy

$$E_{HF} = \langle \Psi | \mathbf{H}_{el} | \Psi \rangle = \int \bar{\Psi}(\mathbf{x}) \mathbf{H}_{el} \Psi(\mathbf{x}) d\mathbf{x}. \quad (\text{A.10})$$

Introducing the one-electron integrals and their notation

$$\langle i | \mathbf{h}(i) | i \rangle = \int \bar{\chi}_i(\mathbf{x}_1) \mathbf{h}(i) \chi_i(\mathbf{x}_1) d\mathbf{x}_1 \quad (\text{A.11})$$

as well as the two-electron integrals

$$\langle ij | kl \rangle = \int \int \bar{\chi}_i(\mathbf{x}_1) \bar{\chi}_j(\mathbf{x}_1) \frac{1}{r_{1,2}} \chi_k(\mathbf{x}_2) \chi_l(\mathbf{x}_2) d\mathbf{x}_1 d\mathbf{x}_2 \quad (\text{A.12})$$

the energy can be recast

$$E_{HF} = \sum_i \langle i | \mathbf{h}(i) | i \rangle + \frac{1}{2} \sum_{i,j} (\langle ij | ij \rangle - \langle ij | ji \rangle). \quad (\text{A.13})$$

Having the expression of the Hartree-Fock energy, the variational principle can be invoked to determine the set of MSO. This principle states that the Slater determinant with the lowest energy is the best approximation to the true wave function describing the system. Thus, if a wave function Ψ close enough to the ground state undergoes a small change $\delta\Psi$, then the change in the energy should be equal to zero, $\delta E_{HF} = 0$. Adding the fact that the MSO are required to be orthonormal, this minimization condition leads after some developments to the canonical Hartree-Fock equations

$$\mathbf{h}(i) \chi_i(i) + \sum_{j \neq i} \left[\int \frac{|\chi_j(j)|^2}{r_{i,j}} d\mathbf{x}_2 \right] \chi_i(i) - \sum_{j \neq i} \left[\int \frac{\bar{\chi}_j(j) \chi_i(j)}{r_{i,j}} d\mathbf{x}_2 \right] \chi_i(i) = \epsilon_i \chi_i(i). \quad (\text{A.14})$$

If the Coulomb operator $\mathbf{J}_j(i)$ and the exchange operator $\mathbf{K}_j(i)$ are defined as

$$\mathbf{J}_j(i) = \int \frac{|\chi_j(j)|^2}{r_{i,j}} d\mathbf{x}_2 \quad \text{and} \quad \mathbf{K}_j(i) = \int \frac{\bar{\chi}_j(j) \chi_i(j)}{r_{i,j}} d\mathbf{x}_2 \quad (\text{A.15})$$

A. HARTREE-FOCK METHOD

and the Fock operator $\mathbf{f}(i)$ as well

$$\mathbf{f}(i) = \mathbf{h}(i) + \sum_{j \neq i} (\mathbf{J}_j(i) - \mathbf{K}_j(i)) \quad (\text{A.16})$$

the equation A.14 can be rewritten

$$\mathbf{f}(i)\chi_i(i) = \epsilon_i\chi_i(i). \quad (\text{A.17})$$

The meaning of the ϵ_i is then disclosed, as they turn out to be the eigenvalues of the Fock operator associated to the canonical MSO. The Coulomb operator $\mathbf{J}_j(i)$ corresponds to the Coulomb interaction between the charge densities defined by $|\chi_i(i)|^2$ and $|\chi_j(j)|^2$. The exchange operator $\mathbf{K}_j(i)$ reflects the fermionic nature of electrons that hinders electrons with same spin to be at same place.

Since the Fock operator definition contains the MSO, this is where the iterative trait of the Hartree-Fock method comes into play. In fact, a set of initial guess for the orbitals is needed in order to define the Hartree-Fock energy and the Fock operator and to solve consequently the Hartree-Fock equations that will supply a new set of orbitals. This new set of orbitals will be used in turn to carry on with the iterative process until the energy difference between two iterative steps is smaller than the defined convergence criteria. Due to such iterative feature, Hartree-Fock calculations are alternatively labeled as self-consistent field calculations (SCF).

A.3 Implementation of the Hartree-Fock method

The codes using the Hartree-Fock method are based on a matrix form of the method coined by Roothaan (143). Indeed, they use a discrete basis set to expand the spatial part of the MSO. Let Φ_i be the spatial part of the MSO χ_i , the expansion of Φ_i in a basis set $\{\phi\}_{\alpha=1,\dots,n}$ is given by

$$\Phi_i = \sum_{\alpha=1}^n c_{\alpha,i} \phi_{\alpha} = \mathbf{c}_i \quad (\text{A.18})$$

where \mathbf{c}_i is the expansion coefficient matrix. The $\{\phi\}$ are called atomic orbitals and the expansion is referred as linear combination of atomic orbital (LCAO). Here the literature conventions are used: the lower-case Roman letters for indexing the MSO and Greek letters for indexing the basis set. If the system is assumed to have all its N electrons paired in $\frac{N}{2}$ orbitals (closed-shell system), the Hartree-Fock energy can be rewritten as

$$E_{HF} = 2 \sum_{i=1}^{\frac{N}{2}} \langle i | \mathbf{h}(i) | i \rangle + \sum_{i=1}^{\frac{N}{2}} \sum_{j=1}^{\frac{N}{2}} (2 \langle ij | ij \rangle - \langle ij | ji \rangle) \quad (\text{A.19})$$

and the Fock operator as

$$\mathbf{f}(i) = \mathbf{h}(i) + \sum_{j=1}^{\frac{N}{2}} (2\mathbf{J}_j(i) - \mathbf{K}_j(i)). \quad (\text{A.20})$$

A.3 Implementation of the Hartree-Fock method

Moreover the Hartree-Fock equation can be recast in matrix form in the atomic orbital basis $\{\phi\}_{\alpha=1,\dots,n}$ as

$$\mathbf{F}\mathbf{c}_i = \epsilon_i \mathbf{S}\mathbf{c}_i \quad (\text{A.21})$$

This set of equations are known as Roothan-Hall equations (143, 144). The terms of the overlap matrix \mathbf{S} are computed as

$$S_{\mu\nu} = \langle \mu | \nu \rangle = \int \phi_\mu(\mathbf{x}_1) \phi_\nu(\mathbf{x}_1) d\mathbf{x}_1. \quad (\text{A.22})$$

The matrix \mathbf{F} is called the Fock matrix and its terms $F_{\mu\nu}$ are defined by

$$F_{\mu\nu} = \langle \mu | \mathbf{f}(i) | \nu \rangle = \langle \mu | -\frac{1}{2} \nabla_i^2 - \sum_A \frac{Z_A}{r_{i,A}} | \nu \rangle + \sum_{\lambda\sigma} P_{\lambda\sigma} \left[\langle \mu\nu | \lambda\sigma \rangle - \frac{1}{2} \langle \mu\lambda | \nu\sigma \rangle \right] \quad (\text{A.23})$$

where $P_{\lambda\sigma}$ are terms of the density matrix \mathbf{P} :

$$P_{\lambda\sigma} = 2 \sum_{i=1}^{\frac{N}{2}} c_{\lambda,i} c_{\sigma,i}. \quad (\text{A.24})$$

In practice, the Hartree-Fock programs compute the overlap, the one-electron and the two-electron integrals along with the density matrix to construct the Fock matrix and then follow the procedure depicted in the Fig. A.1. Despite the approximations assumed in the Hartree-Fock method, the calculations involving large systems are still too expensive. The computational cost does raise dramatically with larger basis set. Indeed, for a basis set of N functions, the amount of two-electron integrals scales proportional to N^4 .

A. HARTREE-FOCK METHOD

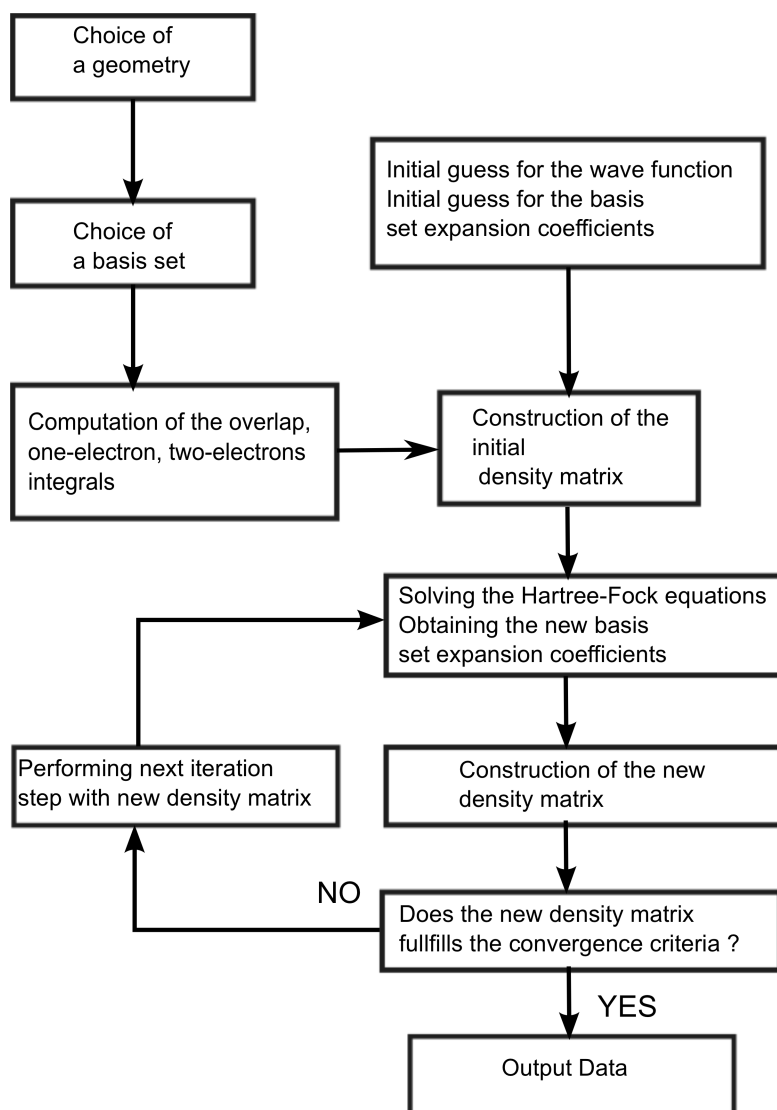


Figure A.1: Flow chart for the Hartree-Fock method (adapted from (145))

Acknowledgements

I would like to thank all the persons who supported me during my PhD.

First, I owe my deepest gratitude to Prof. Dr. Hilbert von Löhneysen for giving me the opportunity to work on such exciting project and to Prof. Dr. Wulf Wulfhekel for taking over the work as secondary referee.

This thesis was made possible thanks to the masterly guidance of my advisor Dr. Romain Danneau who introduced me to the fascinating world of graphene and kept encouraging me throughout these years. Un grand merci!

I am very grateful to Zhang Zhenhao for his help with the Kelvin probe microscopy measurements at the IMT. Also from the IMT, I would like to thank Dr. Hendrik Hoelscher and his group members for their assistance with the Dimension Icon.

I owe a lot to my group colleagues Christian Benz, Julien Bordaz, Jens Mohrmann, Maximilian Thürmer, Philipp Zukowsky and a special thanks to Renjun Du and to Fan Wu for proofreading parts of my work and for their support.

I am indebted to my many of my INT colleagues that have provided scientific guidance and help: Michael Wolf, Michael Engel, Simone Dehm, Maya Lukas, Velimir Meded, Franz Symala, Frank Hennrich among others.

It is a pleasure to thank Magalie Huttin, Coral Herranz-Lancho, Julia Setzler, Andrea Magri, Senthil Kumar Kuppusamy and Mohsen Pouryazdan for their friendship, kindness and support. I will really miss going for lunch to the KIT canteen with you!

Last but not least, I would like to thank my friends and my family for their continuous encouragements and help. I have a special thought for my grandfather back there in Argentina.

References

- [1] P. R. WALLACE. **The Band Theory of Graphite.** *Phys. Rev.*, **71**:622–634, May 1947. [5](#)
- [2] K. S. NOVOSELOV, A. K. GEIM, S. V. MOROZOV, D. JIANG, Y. ZHANG, S. V. DUBONOS, I. V. GRIGORIEVA, AND A. A. FIRSOV. **Electric Field Effect in Atomically Thin Carbon Films.** *Science*, **306**(5696):666–669, 2004. [5](#), [67](#)
- [3] Y. ZHANG, Y.-W. TAN, H.L. STORMER, AND P. KIM. **Experimental observation of the quantum Hall effect and Berry’s phase in graphene.** *Nature*, **438**:201–204, Nov 2005. [5](#)
- [4] A. H. CASTRO NETO, F. GUINEA, N. M. R. PERES, K. S. NOVOSELOV, AND A. K. GEIM. **The electronic properties of graphene.** *Rev. Mod. Phys.*, **81**:109–162, Jan 2009. [6](#), [8](#), [9](#)
- [5] S. IJIMA. **Helical microtubules of graphitic carbon.** *Nature*, **354**:56–58, Nov 1991. [6](#)
- [6] CHEN SONG, YUEYUAN XIA, MINGWEN ZHAO, XIANGDONG LIU, FENG LI, BODA HUANG, HONGYU ZHANG, AND BINGYUN ZHANG. % of Functionalization of silicon-doped single walled carbon nanotubes at the doping site: An ab initio study. *Physics Letters A*, **358**(2):166 – 170, 2006. [10](#)
- [7] N.W. ASHCROFT AND N.D. MERMIN. *Solid state physics.* Science: Physics. Saunders College, 1976. [11](#)
- [8] S. DAS SARMA, SHAFFIQUE ADAM, E. H. HWANG, AND ENRICO ROSSI. **Electronic transport in two-dimensional graphene.** *Rev. Mod. Phys.*, **83**:407–470, May 2011. [11](#)
- [9] A. K. GEIM AND K. S. NOVOSELOV. **The rise of graphene.** *Nature Materials*, **6**:183–191, Mar 2007. [12](#)
- [10] E. FRADKIN. **Critical behavior of disordered degenerate semiconductors. II. Spectrum and transport properties in mean-field theory.** *Phys. Rev. B*, **33**:3263–3268, Mar 1986. [12](#)
- [11] M. I. KATSNELSON. **Zitterbewegung, chirality, and minimal conductivity in graphene.** *The European Physical Journal B - Condensed Matter and Complex Systems*, **51**:157–160, 2006. [12](#)
- [12] P. M. OSTROVSKY, I. V. GORNYI, AND A. D. MIRLIN. **Electron transport in disordered graphene.** *Phys. Rev. B*, **74**:235443, Dec 2006. [12](#)
- [13] K. S. NOVOSELOV, A. K. GEIM, S. V. MOROZOV, D. JIANG, M. I. KATSNELSON, I. V. GRIGORIEVA, S. V. DUBONOS, AND A. A. FIRSOV. **Two-dimensional gas of massless Dirac fermions in graphene.** *Nature*, **438**:197–200, Nov 2005. [12](#)
- [14] K. I. BOLOTIN, K. J. SIKES, Z. JIANG, M. KLIMA, G. FUDENBERG, J. HONE, P. KIM, AND H. L. STORMER. **Ultrahigh electron mobility in suspended graphene.** *Solid State Communications*, **146**:351–355, 2008. [13](#)
- [15] X. DU, I. SKACHKO, A. BARKER, AND E. Y. ANDREI. **Approaching ballistic transport in suspended graphene.** *Nature Nanotechnology*, **3**:491–495, Aug 2008. [13](#)
- [16] S. REICH, C. THOMSEN, AND J. MAULTZSCH. *Carbon Nanotubes.* John Wiley & Sons, 2008. [13](#)
- [17] J. NYGARD, D.H. COBDEN, M. BOCKRATH, P.L. MCEUEN, AND P.E. LINDELOF. **Electrical transport measurements on single-walled carbon nanotubes.** *Applied Physics A*, **69**:297–304, 1999. [13](#)
- [18] A. BACHTOLD, C. STRUNK, J.-P. SALVETAT, J.-M. BONARD, L. FORRÓ, T. NUSSBAUMER, AND C. SCHÖNENBERGER. **Aharonov-Bohm oscillations in carbon nanotubes.** *Nature*, **397**:673–675, Feb 1999. [13](#)
- [19] S. M. CHOI, S. H. JHI, AND Y. W. SON. **Effects of strain on electronic properties of graphene.** *Phys. Rev. B*, **81**:081407, Feb 2010. [14](#)
- [20] W. S. SU, T. C. LEUNG, AND C. T. CHAN. **Work function of single-walled and multiwalled carbon nanotubes: First-principles study.** *Phys. Rev. B*, **76**:235413, Dec 2007. [14](#)
- [21] B. SHAN AND K. CHO. **First Principles Study of Work Functions of Single Wall Carbon Nanotubes.** *Phys. Rev. Lett.*, **94**:236602, Jun 2005. [14](#)
- [22] P. A. KHOMYAKOV, G. GIOVANNETTI, P. C. RUSU, G. BROCKS, J. VAN DEN BRINK, AND P. J. KELLY. **First-principles study of the interaction and charge transfer between graphene and metals.** *Phys. Rev. B*, **79**:195425, May 2009. [14](#), [16](#), [17](#), [18](#), [83](#), [102](#), [105](#)

-
- [23] R. YAN, Q. ZHANG, W. LI, I. CALIZO, T. SHEN, C. A. RICHTER, A. R. HIGHT-WALKER, X. LIANG, A. SEABAUGH, D. JENA, H. G. XING, D. J. GUNDLACH, AND N. V. NGUYEN. **Determination of graphene work function and graphene-insulator-semiconductor band alignment by internal photoemission spectroscopy.** *Applied Physics Letters*, **101**(2):022105, 2012. [14](#)
- [24] Y.-J. YU, Y. ZHAO, S. RYU, L. E. BRUS, K. S. KIM, AND P. KIM. **Tuning the Graphene Work Function by Electric Field Effect.** *Nano Letters*, **9**(10):3430–3434, 2009. [14](#), [85](#), [88](#)
- [25] R. GAO, ZH. PAN, AND ZH. L. WANG. **Work function at the tips of multiwalled carbon nanotubes.** *Applied Physics Letters*, **78**(12):1757–1759, 2001. [14](#)
- [26] S. DATTA. *Electronic Transport in Mesoscopic Systems*. Cambridge Studies in Semiconductor Physics and Microelectronic Engineering. Cambridge University Press, 1997. [15](#)
- [27] F. XIA, V. PEREBEINOS, Y.-M. LIN, Y. WU, AND P. AVOURIS. **The origins and limits of metal-graphene junction resistance.** *Nature Nanotechnology*, **6**:179–184, March 2011. [15](#), [19](#), [104](#), [105](#)
- [28] J. A. ROBINSON, M. LABELLA, M. ZHU, M. HOLLANDER, R. KASARDA, Z. HUGHES, K. TRUMBULL, R. CAVALLERO, AND D. SNYDER. **Contacting graphene.** *Applied Physics Letters*, **98**(5):053103, 2011. [16](#), [18](#)
- [29] G. GIOVANNETTI, P. A. KHOMYAKOV, G. BROCKS, V. M. KARPAN, J. VAN DEN BRINK, AND P. J. KELLY. **Doping Graphene with Metal Contacts.** *Phys. Rev. Lett.*, **101**:026803, Jul 2008. [16](#), [17](#), [83](#), [105](#)
- [30] CH. GONG, G. LEE, B. SHAN, E. M. VOGEL, R. M. WALLACE, AND K. CHO. **First-principles study of metal-graphene interfaces.** *Journal of Applied Physics*, **108**(12):123711, 2010. [17](#), [18](#)
- [31] E. WATANABE, A. CONWILL, D. TSUYA, AND Y. KOIDE. **Low contact resistance metals for graphene based devices.** *Diamond and Related Materials*, **24**(0):171 – 174, 2012. [18](#)
- [32] J. SŁAWIŃSKA AND I. ZASADA. **Fingerprints of Dirac points in first-principles calculations of scanning tunneling spectra of graphene on a metal substrate.** *Phys. Rev. B*, **84**:235445, Dec 2011. [18](#)
- [33] S. M. SONG, J. K. PARK, O. J. SUL, AND B. J. CHO. **Determination of Work Function of Graphene under a Metal Electrode and Its Role in Contact Resistance.** *Nano Letters*, **12**(8):3887–3892, 2012. [18](#)
- [34] J. SŁAWIŃSKA, I. WLASNY, P. DABROWSKI, Z. KLUSEK, AND I. ZASADA. **Doping domains in graphene on gold substrates: First-principles and scanning tunneling spectroscopy studies.** *Phys. Rev. B*, **85**:235430, Jun 2012. [18](#)
- [35] R. S. SUNDARAM, M. STEINER, H.-Y. CHIU, M. ENGEL, A. A. BOL, R. KRUPKE, M. BURGHARD, K. KERN, AND P. AVOURIS. **The Graphene-Gold Interface and Its Implications for Nanoelectronics.** *Nano Letters*, **11**(9):3833–3837, 2011. [18](#)
- [36] Q. J. WANG AND J. G. CHE. **Origins of Distinctly Different Behaviors of Pd and Pt Contacts on Graphene.** *Phys. Rev. Lett.*, **103**:066802, Aug 2009. [18](#)
- [37] B. UCHOA, C.-Y. LIN, AND A. H. CASTRO NETO. **Tailoring graphene with metals on top.** *Phys. Rev. B*, **77**:035420, Jan 2008. [18](#)
- [38] K. NAGASHIO, T. NISHIMURA, K. KITA, AND A. TORIUMI. **Contact resistivity and current flow path at metal/graphene contact.** *Applied Physics Letters*, **97**(14):143514, 2010. [19](#), [102](#)
- [39] A. VENUGOPAL, L. COLOMBO, AND E. M. VOGEL. **Contact resistance in few and multilayer graphene devices.** *Applied Physics Letters*, **96**(1):013512, 2010. [19](#)
- [40] S. RUSSO, M.F. CRACIUN, M. YAMAMOTO, A.F. MORPURGO, AND S. TARUCHA. **Contact resistance in graphene-based devices.** *Physica E: Low-dimensional Systems and Nanostructures*, **42**(4):677–679, 2010. [19](#)
- [41] P. BLAKE, R. YANG, S.V. MOROZOV, F. SCHEDIN, L.A. PONOMARENKO, A.A. ZHUKOV, R.R. NAIR, I.V. GRIGORIEVA, K.S. NOVOSELOV, AND A.K. GEIM. **Influence of metal contacts and charge inhomogeneity on transport properties of graphene near the neutrality point.** *Solid State Communications*, **149**(2728):1068 – 1071, 2009. [19](#)
- [42] A. A. KANE, T. SHEPS, E. T. BRANIGAN, V. A. APKARIAN, M. H. CHENG, J. C. HEMMINGER, S. R. HUNT, AND P. G. COLLINS. **Graphitic Electrical Contacts to Metallic Single-Walled Carbon Nanotubes Using Pt Electrodes.** *Nano Letters*, **9**(10):3586–3591, 2009. [20](#)
- [43] Y. CHAI, A. HAZEGHI, K. TAKEI, HONG-YU CHEN, P.C.H. CHAN, A. JAVEY, AND H.-S.P. WONG. **Low-Resistance Electrical Contact to Carbon Nanotubes With Graphitic Interfacial Layer.** *Electron Devices, IEEE Transactions on*, **59**(1):12 –19, Jan 2012. [20](#)
- [44] M. TAMAOKI, S. KISHIMOTO, Y. OHNO, AND T. MIZUTANI. **Electrical properties of the graphitic carbon contacts on carbon nanotube field effect transistors.** *Applied Physics Letters*, **101**(3):033101, July 2012. [20](#)
- [45] S. PAULSON, A. HELSER, M. BUONGIORNO NARDELLI, R. M. TAYLOR, M. FALVO, R. SUPERFINE, AND S. WASHBURN. **Tunable Resistance of a Carbon Nanotube-Graphite Interface.** *Science*, **290**(5497):1742–1744, 2000. [20](#), [21](#)

-
- [46] B. LI, X. CAO, H. G. ONG, J. W. CHEAH, X. ZHOU, Z. YIN, H. LI, J. WANG, F. BOEY, W. HUANG, AND H. ZHANG. **All-Carbon Electronic Devices Fabricated by Directly Grown Single-Walled Carbon Nanotubes on Reduced Graphene Oxide Electrodes.** *Advanced Materials*, **22**(28):3058–3061, 2010. [21](#), [22](#), [65](#)
- [47] T. PEI, H. XU, ZH. ZHANG, ZH. WANG, Y. LIU, Y. LI, SH. WANG, AND L.-M. PENG. **Electronic transport in single-walled carbon nanotube/graphene junction.** *Applied Physics Letters*, **99**(11):113102, 2011. [21](#), [22](#), [65](#)
- [48] B. GAO, Y. F. CHEN, M. S. FUHRER, D. C. GLATTLI, AND A. BACHTOLD. **Four-Point Resistance of Individual Single-Wall Carbon Nanotubes.** *Phys. Rev. Lett.*, **95**:196802, Oct 2005. [21](#)
- [49] S. JANG, H. JANG, Y. LEE, D. SUH, S. BAIK, B. HEE HONG, AND J.-H. AHN. **Flexible, transparent single-walled carbon nanotube transistors with graphene electrodes.** *Nanotechnology*, **21**(42):425201, 2010. [21](#)
- [50] J. LEE, V. VARSHNEY, J. S. BROWN, A. K. ROY, AND B. L. FARMER. **Single mode phonon scattering at carbon nanotube-graphene junction in pillared graphene structure.** *Applied Physics Letters*, **100**(18):183111, 2012. [22](#)
- [51] B. G. COOK, W. R. FRENCH, AND K. VARGA. **Electron transport properties of carbon nanotube—graphene contacts.** *Applied Physics Letters*, **101**(15):153501, 2012. [22](#)
- [52] J. GONZÁLEZ, F. GUINEA, AND J. HERRERO. **Propagating, evanescent, and localized states in carbon nanotube-graphene junctions.** *Phys. Rev. B*, **79**:165434, Apr 2009. [22](#)
- [53] F. D. NOVAES, R. RURALI, AND P. ORDEJON. **Electronic Transport between Graphene Layers Covalently Connected by Carbon Nanotubes.** *ACS Nano*, **4**(12):7596–7602, 2010. [22](#)
- [54] K. L. MA, X. H. YAN, Y. D. GUO, AND Y. XIAO. **Electronic transport properties of junctions between carbon nanotubes and graphene nanoribbons.** *European Physical Journal B*, **83**:487–492, oct 2011. [22](#)
- [55] G. K. DIMITRAKAKIS, E. TYLIANAKIS, AND G. E. FROUDAKIS. **Pillared Graphene: A New 3-D Network Nanostructure for Enhanced Hydrogen Storage.** *Nano Letters*, **8**(10):3166–3170, 2008. PMID: 18800853. [22](#)
- [56] K.L. MA, X.H. YAN, Y.D. GUO, AND Y. XIAO. **Electronic transport properties of junctions between carbon nanotubes and graphene nanoribbons.** *The European Physical Journal B*, **83**:487–492, 2011. [22](#)
- [57] J.A. POPLE AND D.L. BEVERIDGE. *Approximate molecular orbital theory.* McGraw-Hill series in advanced chemistry. McGraw-Hill, 1970. [24](#)
- [58] M. J. S. DEWAR AND W. THIEL. **Ground states of molecules. 38. The MNDO method. Approximations and parameters.** *Journal of the American Chemical Society*, **99**(15):4899–4907, 1977. [24](#)
- [59] J. STEWART. **Optimization of parameters for semiempirical methods V: Modification of NDDO approximations and application to 70 elements.** *Journal of Molecular Modeling*, **13**:1173–1213, 2007. [24](#)
- [60] J. REZAC, J. FANFRLIK, D. SALAHUB, AND P. HOBZA. **Semiempirical Quantum Chemical PM6 Method Augmented by Dispersion and H-Bonding Correction Terms Reliably Describes Various Types of Noncovalent Complexes.** *Journal of Chemical Theory and Computation*, **5**(7):1749–1760, 2009. [24](#)
- [61] P. JUREKA, J. ERN, P. HOBZA, AND D. R. SALAHUB. **Density functional theory augmented with an empirical dispersion term. Interaction energies and geometries of 80 noncovalent complexes compared with ab initio quantum mechanics calculations.** *Journal of Computational Chemistry*, **28**(2):555–569, 2007. [25](#)
- [62] S. GRIMME. **Accurate description of van der Waals complexes by density functional theory including empirical corrections.** *Journal of Computational Chemistry*, **25**(12):1463–1473, 2004. [25](#)
- [63] J. J. P. STEWART. **MOPAC2009.** Stewart Computational Chemistry. [25](#)
- [64] A. BANERJEE, N. ADAMS, J. SIMONS, AND R. SHEPARD. **Search for stationary points on surfaces.** *The Journal of Physical Chemistry*, **89**(1):52–57, 1985. [26](#)
- [65] P. CULOT, G. DIVE, V. H. NGUYEN, AND J. M. GHUYSEN. **A quasi-Newton algorithm for first-order saddle-point location.** *Theoretical Chemistry Accounts: Theory, Computation, and Modeling (Theoretica Chimica Acta)*, **82**:189–205, 1992. [26](#)
- [66] M. SEYDOU, Y. J. DAPPE, S. MARSAUDON, J.-P. AIMÉ, X. BOUJU, AND A.-M. BONNOT. **Atomic force microscope measurements and LCAO- S^2 + vdW calculations of contact length between a carbon nanotube and a graphene surface.** *Phys. Rev. B*, **83**:045410, Jan 2011. [27](#), [28](#), [30](#), [31](#)
- [67] JOHN F. DOBSON, ANGELA WHITE, AND ANGEL RUBIO. **Asymptotics of the Dispersion Interaction: Analytic Benchmarks for van der Waals Energy Functionals.** *Phys. Rev. Lett.*, **96**:073201, Feb 2006. [28](#), [29](#)

-
- [68] J. F. DOBSON AND T. GOULD. **Calculation of dispersion energies.** *Journal of Physics: Condensed Matter*, **24**(7):073201, 2012. [28](#), [29](#)
- [69] F. SYMALLA. **Intercalation of Transition Metals in Twisted Graphene Bilayers.** Karlsruhe Institut of Technologie, 2012. Master's Thesis. [30](#)
- [70] Y. J. DAPPE, J. ORTEGA, AND F. FLORES. **Intermolecular interaction in density functional theory: Application to carbon nanotubes and fullerenes.** *Phys. Rev. B*, **79**:165409, Apr 2009. [30](#)
- [71] Y. J. DAPPE, M. A. BASANTA, F. FLORES, AND J. ORTEGA. **Weak chemical interaction and van der Waals forces between graphene layers: A combined density functional and intermolecular perturbation theory approach.** *Phys. Rev. B*, **74**:205434, Nov 2006. [30](#)
- [72] M. SEYDOU, S. MARSAUDON, J. BUCHOUX, J. P. AIMÉ, AND A. M. BONNOT. **Molecular mechanics investigations of carbon nanotube and graphene sheet interaction.** *Phys. Rev. B*, **80**:245421, Dec 2009. [30](#)
- [73] R. SCHINZINGER AND P.A.A. LAURA. *Conformal Mapping: Methods and Applications.* Dover Books on Mathematics Series. Dover Publications, 2003. [33](#), [34](#)
- [74] M. L. OLSON AND K. R. SUNDBERG. **An atom monopole–dipole interaction model with charge transfer for the treatment of polarizabilities of pi-bonded molecules.** *The Journal of Chemical Physics*, **69**(12):5400–5404, 1978. [40](#)
- [75] J. APPLEQUIST, J. R. CARL, AND K.-K. FUNG. **Atom dipole interaction model for molecular polarizability. Application to polyatomic molecules and determination of atom polarizabilities.** *Journal of the American Chemical Society*, **94**(9):2952–2960, 1972. [40](#)
- [76] B. SHANKER AND J. APPLEQUIST. **Polarizabilities of fullerenes C₂₀ through C₂₄₀ from atom monopole-dipole interaction theory.** *The Journal of Physical Chemistry*, **98**(26):6486–6489, 1994. [40](#)
- [77] H. A. STERN, G. A. KAMINSKI, J. L. BANKS, R. ZHOU, B. J. BERNE, AND R. A. FRIESNER. **Fluctuating Charge, Polarizable Dipole, and Combined Models: Parameterization from ab Initio Quantum Chemistry.** *The Journal of Physical Chemistry B*, **103**(22):4730–4737, 1999. [40](#)
- [78] A. MAYER. **A monopole-dipole model to compute the polarization of metallic carbon nanotubes.** *Applied Physics Letters*, **86**(15):153110, 2005. [40](#), [43](#)
- [79] A. MAYER. **Polarization of metallic carbon nanotubes from a model that includes both net charges and dipoles.** *Phys. Rev. B*, **71**:235333, Jun 2005. [40](#)
- [80] A. MAYER. **Formulation in terms of normalized propagators of a charge-dipole model enabling the calculation of the polarization properties of fullerenes and carbon nanotubes.** *Phys. Rev. B*, **75**:045407, Jan 2007. [40](#), [43](#)
- [81] A. MAYER, PH LAMBIN, AND P-O STRAND. **An electrostatic interaction model for frequency-dependent polarizability: methodology and applications to hydrocarbons and fullerenes.** *Nanotechnology*, **19**(2):025203, 2008. [40](#)
- [82] A. MAYER AND P.-O. ASTRAND. **A ChargeDipole Model for the Static Polarizability of Nanostructures Including Aliphatic, Olephinic, and Aromatic Systems.** *The Journal of Physical Chemistry A*, **112**(6):1277–1285, 2008. PMID: 18198848. [40](#)
- [83] R. LANGLET, A. MAYER, N. GEUQUET, H. AMARA, M. VANDESCUREN, L. HENRARD, S. MAKSIMENKO, AND PH. LAMBIN. **Study of the polarizability of fullerenes with a monopoledipole interaction model.** *Diamond and Related Materials*, **16**(12):2145 – 2149, 2007. [40](#)
- [84] ZH. WANG AND M. DEVEL. **Electrostatic deflections of cantilevered metallic carbon nanotubes via charge-dipole model.** *Phys. Rev. B*, **76**:195434, Nov 2007. [40](#)
- [85] ZH. WANG, M. ZDROJEK, TH. MÉLIN, AND M. DEVEL. **Electric charge enhancements in carbon nanotubes: Theory and experiments.** *Phys. Rev. B*, **78**:085425, Aug 2008. [40](#)
- [86] ZH. WANG AND R. W. SCHARSTEIN. **Electrostatics of graphene: Charge distribution and capacitance.** *Chemical Physics Letters*, **489**(46):229 – 236, 2010. [40](#), [44](#)
- [87] E. ANDERSON, Z. BAI, C. BISCHOF, S. BLACKFORD, J. DEMMEL, J. DONGARRA, J. DU CROZ, A. GREENBAUM, S. HAMMARLING, A. MCKENNEY, AND D. SORENSEN. *LAPACK Users' Guide.* Society for Industrial and Applied Mathematics, Philadelphia, PA, third edition, 1999. [43](#)
- [88] P. G. SILVESTROV AND K. B. EFETOV. **Charge accumulation at the boundaries of a graphene strip induced by a gate voltage: Electrostatic approach.** *Phys. Rev. B*, **77**:155436, Apr 2008. [44](#)
- [89] ZH. WANG. *Propriétés électro-mécaniques des nanotubes de carbone.* PhD thesis, Université de Franche-Comté, 2008. [45](#)
- [90] P. KEBLINSKI, S. K. NAYAK, P. ZAPOL, AND P. M. AJAYAN. **Charge Distribution and Stability of Charged Carbon Nanotubes.** *Phys. Rev. Lett.*, **89**:255503, Dec 2002. [45](#)
- [91] CH. LI AND T.-W. CHOU. **Electrostatic charge distribution on single-walled carbon nanotubes.** *Applied Physics Letters*, **89**(6):063103, 2006. [45](#)

-
- [92] J. C. MEYER, A. K. GEIM, M. I. KATSNELSON, K. S. NOVOSELOV, T. J. BOOTH, AND S. ROTH. **The structure of suspended graphene sheets.** *Nature*, **446**(7131):60–63, March 2007. [61](#)
- [93] S. ENGELS, P. WEBER, B. TERRÉS, J. DAUBER, C. MEYER, C. VOLK, S. TRELLENKAMP, U. WICHMANN, AND C. STAMPFER. **Transport in coupled graphene-nanotube quantum devices.** *ArXiv e-prints*, April 2012. [65](#)
- [94] NGS NATURGRAPHIT GMBH. "http://www.graphit.de/". [66](#)
- [95] P. BLAKE, E. W. HILL, A. H. CASTRO NETO, K. S. NOVOSELOV, D. JIANG, R. YANG, T. J. BOOTH, AND A. K. GEIM. **Making graphene visible.** *Applied Physics Letters*, **91**(6):063124, 2007. [67](#)
- [96] S. RODDARO, P. PINGUE, V. PIAZZA, V. PELLEGRINI, AND F. BELTRAM. **The Optical Visibility of Graphene: Interference Colors of Ultrathin Graphite on SiO₂.** *Nano Letters*, **7**(9):2707–2710, 2007. PMID: 17665963. [67](#)
- [97] M.S. DRESSELHAUS, G. DRESSELHAUS, R. SAITO, AND A. JORIO. **Raman spectroscopy of carbon nanotubes.** *Physics Reports*, **409**(2):47 – 99, 2005. [68](#)
- [98] A. C. FERRARI, J. C. MEYER, V. SCARDACI, C. CASIRAGHI, M. LAZZERI, F. MAURI, S. PISCANEC, D. JIANG, K. S. NOVOSELOV, S. ROTH, AND A. K. GEIM. **Raman Spectrum of Graphene and Graphene Layers.** *Phys. Rev. Lett.*, **97**:187401, Oct 2006. [68](#)
- [99] A. C. FERRARI. **Raman spectroscopy of graphene and graphite: Disorder, electronphonon coupling, doping and nonadiabatic effects.** *Solid State Communications*, **143**(12):47 – 57, 2007. [68](#)
- [100] L.M. MALARD, M.A. PIMENTA, G. DRESSELHAUS, AND M.S. DRESSELHAUS. **Raman spectroscopy in graphene.** *Physics Reports*, **473**(56):51 – 87, 2009. [68](#), [69](#)
- [101] NANOCYL COMPANY. "http://www.spmtips.com/". [71](#)
- [102] SH. LIN AND D. BLANKSCHTEIN. **Role of the Bile Salt Surfactant Sodium Cholate in Enhancing the Aqueous Dispersion Stability of Single-Walled Carbon Nanotubes: A Molecular Dynamics Simulation Study.** *The Journal of Physical Chemistry B*, **114**(47):15616–15625, 2010. [71](#)
- [103] W. WENSELEERS, I.I. VLASOV, E. GOOVAERTS, E.D. OBRATZSOVA, A.S. LOBACH, AND A. BOUWEN. **Efficient Isolation and Solubilization of Pristine Single-Walled Nanotubes in Bile Salt Micelles.** *Advanced Functional Materials*, **14**(11):1105–1112, 2004. [71](#)
- [104] MIKROMASCH COMPANY. "http://www.spmtips.com/". [73](#)
- [105] M. MARTIN, L. ROSCHIER, P. HAKONEN, U. PARTS, M. PAALANEN, B. SCHLEICHER, AND E. I. KAUPPINEN. **Manipulation of Ag nanoparticles utilizing noncontact atomic force microscopy.** *Applied Physics Letters*, **73**(11):1505–1507, 1998. [74](#)
- [106] E. TRANVOUEZ, A. ORIEUX, E. BOER-DUCHEMIN, C H DEVILLERS, V HUC, G COMTET, AND G DUJARDIN. **Manipulation of cadmium selenide nanorods with an atomic force microscope.** *Nanotechnology*, **20**(16):165304, 2009. [74](#)
- [107] E. GNECCO, A. RAO, K. MOUGIN, G. CHANDRASEKAR, AND E. MEYER. **Controlled manipulation of rigid nanorods by atomic force microscopy.** *Nanotechnology*, **21**(21):215702, 2010. [74](#)
- [108] D. M. SCHAEFER, R. REIFENBERGER, A. PATIL, AND R. P. ANDRES. **Fabrication of two-dimensional arrays of nanometer-size clusters with the atomic force microscope.** *Applied Physics Letters*, **66**(8):1012–1014, 1995. [74](#)
- [109] M. AHLKOG, R. TARKIAINEN, L. ROSCHIER, AND P. HAKONEN. **Single-electron transistor made of two crossing multiwalled carbon nanotubes and its noise properties.** *Applied Physics Letters*, **77**(24):4037–4039, 2000. [74](#)
- [110] T. HERTEL, R. MARTEL, AND P. AVOURIS. **Manipulation of Individual Carbon Nanotubes and Their Interaction with Surfaces.** *The Journal of Physical Chemistry B*, **102**(6):910–915, 1998. [74](#)
- [111] L. DONG, F. ARAI, AND T. FUKUDA. **3D nanorobotic manipulations of multi-walled carbon nanotubes.** In *Robotics and Automation, 2001. Proceedings 2001 ICRA. IEEE International Conference on*, **1**, pages 632 – 637 vol.1, 2001. [74](#)
- [112] M. NONNENMACHER, M. P. O'BOYLE, AND H. K. WICKRAMASINGHE. **Kelvin probe force microscopy.** *Applied Physics Letters*, **58**(25):2921–2923, 1991. [84](#)
- [113] A. KIKUKAWA, S. HOSAKA, AND R. IMURA. **Silicon pn junction imaging and characterizations using sensitivity enhanced Kelvin probe force microscopy.** *Applied Physics Letters*, **66**(25):3510–3512, 1995. [84](#)
- [114] D. ZIEGLER, J. RYCHEN, N. NAUJOKS, AND A. STEMMER. **Compensating electrostatic forces by single-scan Kelvin probe force microscopy.** *Nanotechnology*, **18**(22):225505, 2007. [84](#)
- [115] S. S. DATTA, D. R. STRACHAN, E. J. MELE, AND A. T. CHARLIE JOHNSON. **Surface Potentials and Layer Charge Distributions in Few-Layer Graphene Films.** *Nano Letters*, **9**(1):7–11, 2009. [85](#)

-
- [116] D. ZIEGLER, P. GAVA, J. GÜTTINGER, F. MOLITOR, L. WIRTZ, M. LAZZERI, A. M. SAITTA, A. STEMMER, F. MAURI, AND C. STAMPPER. **Variations in the work function of doped single- and few-layer graphene assessed by Kelvin probe force microscopy and density functional theory.** *Phys. Rev. B*, **83**:235434, Jun 2011. [85](#)
- [117] R. WANG, SH. WANG, D. ZHANG, ZH. LI, Y. FANG, AND X. QIU. **Control of Carrier Type and Density in Exfoliated Graphene by Interface Engineering.** *ACS Nano*, **5**(1):408–412, 2011. [85](#)
- [118] Y. SHI, X. DONG, P. CHEN, J. WANG, AND L.-J. LI. **Effective doping of single-layer graphene from underlying SiO₂ substrates.** *Phys. Rev. B*, **79**:115402, Mar 2009. [85](#)
- [119] W.-J. LIU, H.-Y. YU, S.-H. XU, Q. ZHANG, X. ZOU, J.-L. WANG, K.-L. PEY, J. WEI, H.-L. ZHU, AND M.-F. LI. **Understanding Asymmetric Transportation Behavior in Graphene Field-Effect Transistors Using Scanning Kelvin Probe Microscopy.** *Electron Device Letters, IEEE*, **32**(2):128–130, Feb 2011. [85](#)
- [120] J. MOSER, A. VERDAGUER, D. JIMENEZ, A. BARREIRO, AND A. BACHTOLD. **The environment of graphene probed by electrostatic force microscopy.** *Applied Physics Letters*, **92**(12):123507, 2008. [85](#)
- [121] L. J. VAN DER PAUW. **A method of measuring specific resistivity and Hall effect of discs of arbitrary shape.** *Philips Res.Rep*, **13**(1), 1958. [91](#)
- [122] D.K. SCHRODER. *Semiconductor Material and Device Characterization*. Wiley, 2006. [91](#)
- [123] P JOSHI, H E ROMERO, A T NEAL, V K TOUTAM, AND S A TADIGADAPA. **Intrinsic doping and gate hysteresis in graphene field effect devices fabricated on SiO₂ substrates.** *Journal of Physics: Condensed Matter*, **22**(33):334214, 2010. [95](#)
- [124] Y. J. SHIN, J. H. KWON, G. KALON, K.-T. LAM, C. S. BHATIA, G. LIANG, AND H. YANG. **Ambipolar bistable switching effect of graphene.** *Applied Physics Letters*, **97**(26):262105, 2010. [95](#)
- [125] CH. LAN, P. SRISUNGSITHISUNTI, P. B AMAMA, T. S FISHER, X. XU, AND R. G REIFENBERGER. **Measurement of metal/carbon nanotube contact resistance by adjusting contact length using laser ablation.** *Nanotechnology*, **19**(12):125703, 2008. [97](#)
- [126] A. BACHTOLD, M. S. FUHRER, S. PLYASUNOV, M. FORERO, ERIK H. ANDERSON, A. ZETTL, AND PAUL L. MCEUEN. **Scanned Probe Microscopy of Electronic Transport in Carbon Nanotubes.** *Phys. Rev. Lett.*, **84**:6082–6085, Jun 2000. [97](#)
- [127] PHILIP G. COLLINS, M. HERSAM, M. ARNOLD, R. MARTEL, AND PH. AVOURIS. **Current Saturation and Electrical Breakdown in Multiwalled Carbon Nanotubes.** *Phys. Rev. Lett.*, **86**:3128–3131, Apr 2001. [97](#)
- [128] A. BACHTOLD, M. DE JONGE, K. GROVE-RASMUSSEN, P. L. MCEUEN, M. BUITELAAR, AND C. SCHÖNENBERGER. **Suppression of Tunneling into Multiwall Carbon Nanotubes.** *Phys. Rev. Lett.*, **87**:166801, Oct 2001. [97](#)
- [129] B. BOURLON, D. C. GLATTLI, B. PLAÇAIS, J. M. BERROIR, C. MIKO, L. FORRÓ, AND A. BACHTOLD. **Geometrical Dependence of High-Bias Current in Multiwalled Carbon Nanotubes.** *Phys. Rev. Lett.*, **92**:026804, Jan 2004. [97](#)
- [130] S. HEINZE, J. TERSOFF, R. MARTEL, V. DERYCKE, J. APPENZELLER, AND PH. AVOURIS. **Carbon Nanotubes as Schottky Barrier Transistors.** *Phys. Rev. Lett.*, **89**:106801, Aug 2002. [102](#)
- [131] W. ZHU AND E. KAXIRAS. **Schottky barrier formation at a carbon nanotube-metal junction.** *Applied Physics Letters*, **89**(24):243107, 2006. [102](#)
- [132] F. WAKAYA, K. KATAYAMA, AND K. GAMO. **Contact resistance of multiwall carbon nanotubes.** *Microelectronic Engineering*, **6768**(0):853 – 857, 2003. [102](#)
- [133] D. MANN, A. JAVEY, J. KONG, Q. WANG, AND H. DAI. **Ballistic Transport in Metallic Nanotubes with Reliable Pd Ohmic Contacts.** *Nano Letters*, **3**(11):1541–1544, 2003. [102](#)
- [134] ZH. CHEN, J. APPENZELLER, J. KNOCH, Y.-M. LIN, AND P. AVOURIS. **The Role of Metal-Nanotube Contact in the Performance of Carbon Nanotube Field-Effect Transistors.** *Nano Letters*, **5**(7):1497–1502, 2005. [102](#)
- [135] NORBERT NEMEC, DAVID TOMÁNEK, AND GIANAURELIO CUNIBERTI. **Contact Dependence of Carrier Injection in Carbon Nanotubes: An *Ab Initio* Study.** *Phys. Rev. Lett.*, **96**:076802, Feb 2006. [102](#), [105](#)
- [136] P.M. SOLOMON. **Contact Resistance to a One-Dimensional Quasi-Ballistic Nanotube/Wire.** *Electron Device Letters, IEEE*, **32**(3):246–248, Mar 2011. [102](#)
- [137] A. D. FRANKLIN AND Z. CHEN. **Length scaling of carbon nanotube transistors.** *Nature Nanotechnology*, **5**:858–862, December 2010. [102](#)
- [138] H. XU, SH. WANG, ZH. ZHANG, ZH. WANG, H. XU, AND L.-M. PENG. **Contact length scaling in graphene field-effect transistors.** *Applied Physics Letters*, **100**(10):103501, 2012. [102](#), [103](#)

-
- [139] F. XIA, T. MUELLER, R. GOLIZADEH-MOJARAD, M. FREITAG, Y.-MI. LIN, J. TSANG, V. PEREBEINOS, AND P. AVOURIS. **Photocurrent Imaging and Efficient Photon Detection in a Graphene Transistor.** *Nano Letters*, **9**(3):1039–1044, 2009. [104](#)
- [140] T. MUELLER, F. XIA, M. FREITAG, J. TSANG, AND PH. AVOURIS. **Role of contacts in graphene transistors: A scanning photocurrent study.** *Phys. Rev. B*, **79**:245430, Jun 2009. [104](#)
- [141] R. JALILIAN, L. A. JAUREGUI, G. LOPEZ, J. TIAN, C. ROECKER, M. M. YAZDANPANAHI, R. W. COHN, I. JOVANOVIĆ, AND Y. P. CHEN. **Scanning gate microscopy on graphene: charge inhomogeneity and extrinsic doping.** *Nanotechnology*, **22**(29):295705, 2011. [104](#)
- [142] D.R. HARTREE. **The Wave Mechanics of an Atom with a Non-Coulomb Central Field. Part I. Theory and Methods.** *Proc. Cambridge Phil. Soc.*, **24**:89–110, 1928. [114](#)
- [143] C. C. J. Roothaan. **New Developments in Molecular Orbital Theory.** *Rev. Mod. Phys.*, **23**:69–89, Apr 1951. [116](#), [117](#)
- [144] G. G. HALL. **The Molecular Orbital Theory of Chemical Valency. VIII. A Method of Calculating Ionization Potentials.** *Proceedings of the Royal Society of London. Series A. Mathematical and Physical Sciences*, **205**(1083):541–552, 1951. [117](#)
- [145] C.J. CRAMER. *Essentials of Computational Chemistry: Theories and Models.* John Wiley and Sons, 2005. [118](#)